



UNIL | Université de Lausanne

Unicentre

CH-1015 Lausanne

<http://serval.unil.ch>

Year : 2014

Multiscale Descriptions of Density-Driven Flow Instabilities in Porous Media

Künze Rouven

Künze Rouven, 2014, Multiscale Descriptions of Density-Driven Flow Instabilities in Porous Media

Originally published at : Thesis, University of Lausanne

Posted at the University of Lausanne Open Archive.
<http://serval.unil.ch>

Droits d'auteur

L'Université de Lausanne attire expressément l'attention des utilisateurs sur le fait que tous les documents publiés dans l'Archive SERVAL sont protégés par le droit d'auteur, conformément à la loi fédérale sur le droit d'auteur et les droits voisins (LDA). A ce titre, il est indispensable d'obtenir le consentement préalable de l'auteur et/ou de l'éditeur avant toute utilisation d'une oeuvre ou d'une partie d'une oeuvre ne relevant pas d'une utilisation à des fins personnelles au sens de la LDA (art. 19, al. 1 lettre a). A défaut, tout contrevenant s'expose aux sanctions prévues par cette loi. Nous déclinons toute responsabilité en la matière.

Copyright

The University of Lausanne expressly draws the attention of users to the fact that all documents published in the SERVAL Archive are protected by copyright in accordance with federal law on copyright and similar rights (LDA). Accordingly it is indispensable to obtain prior consent from the author and/or publisher before any use of a work or part of a work for purposes other than personal use within the meaning of LDA (art. 19, para. 1 letter a). Failure to do so will expose offenders to the sanctions laid down by this law. We accept no liability in this respect.



Faculté des géosciences et de l'environnement
Institut des sciences de la terre

Multiscale Descriptions of Density-Driven Flow Instabilities in Porous Media

Thèse de doctorat

Présentée à la
Faculté des géosciences et de l'environnement de
l'Université de Lausanne

par

Rouven Künze

Dipl.-Ing. (Environmental Engineering)
University of Stuttgart (Germany)

Jury

Prof. Dr. Eric Verrecchia, Président
Prof. Dr. Klaus Holliger, Rapporteur
Prof. Dr. Ivan Lunati, Directeur de thèse
Prof. Dr. Patrick Jenny, Expert
Prof. Dr. Niklas Linde, Expert

Lausanne, 2014

IMPRIMATUR

Vu le rapport présenté par le jury d'examen, composé de

Président de la séance publique :	M. le Professeur Eric Verrecchia
Président du colloque :	M. le Professeur Eric Verrecchia
Directeur de thèse :	M. le Professeur Ivan Lunati
Rapporteur :	M. le Professeur Klaus Holliger
Expert externe :	M. le Professeur Patrick Jenny
Expert interne :	M. le Professeur Niklas Linde

Le Doyen de la Faculté des géosciences et de l'environnement autorise l'impression de la thèse de

Monsieur Rouven KÜNZE

Titulaire d'un
Diploma in environmental engineering
Universität de Stuttgart

intitulée

**MULTISCALE DESCRIPTIONS OF DENSITY-DRIVEN FLOW
INSTABILITIES IN POROUS MEDIA**

Lausanne, le 6 mars 2014

Pour le Doyen de la Faculté des géosciences et
de l'environnement



Professeur Eric Verrecchia, Vice-doyen

Contents

Résumé	vii
Abstract	ix
Acknowledgments	xi
1 Introduction	1
1.1 Preamble	1
1.2 Analytical formulations	3
1.2.1 Single-phase flow and transport	3
1.2.2 Multiphase flow	3
1.3 Numerical discretization	4
1.3.1 Finite-Volume method	4
1.3.2 MaFloT and MaFloTT	7
1.4 Challenges in modelling density-driven instabilities	8
1.5 MsFV: concept, findings and limitations	9
1.6 Objectives	10
2 An adaptive multiscale method for density-driven instabilities	13
2.1 Abstract	14
2.2 Introduction	14
2.3 Governing equations	15
2.4 Discretization and coupling	16
2.5 The MsFV method	17
2.5.1 The MsFV pressure solution	17
2.6 Adaptive iterative MsFV method and transport	19
2.6.1 Iterative improvement of the local boundary conditions	19
2.6.2 Adaptivity and transport	20
2.7 The iMsFV as downscaling method (DMsFV)	21
2.8 Numerical simulations	23
2.8.1 MsFV simulation of saltwater-freshwater instabilities	23
2.8.2 Error sources in the MsFV method	24

2.8.3	Adaptive iMsFV simulations of saltwater-freshwater instabilities	26
2.8.4	Grid convergence study of the Elder problem with the DMsFV method	28
2.8.5	The effects of the advection schemes on the grid-convergence of the Elder problem	29
2.9	Conclusions	31
3	A Multilevel Multiscale Finite-Volume method	35
3.1	Abstract	36
3.2	Introduction	36
3.3	Governing equations	38
3.4	The Multilevel MsFV (MMsFV) method	39
3.4.1	MsFV pressure	39
3.4.2	Multilevel MsFV pressure	40
3.4.3	Conservative fine-scale fluxes	41
3.5	Iterative improvement of the solution	43
3.6	Complexity analysis	44
3.6.1	Complexity of MsFV	44
3.6.2	Complexity of MMsFV	45
3.6.3	Complexity of the iterative methods	47
3.7	Numerical Simulations	48
3.7.1	Two-dimensional pressure solutions	48
3.7.2	Two-dimensional pressure convergence study	49
3.7.3	Three-dimensional pressure convergence study	51
3.7.4	Effect of the nested reconstruction on saturation results	52
3.8	Conclusions	54
3.9	Appendix	56
3.9.1	MsFV operators	56
3.9.2	Calculation of β	57
3.9.3	2-Level reuse formulation	57
4	Local modeling of instability onset for global finger evolution	59
4.1	Abstract	60
4.2	Introduction	60
4.3	Governing equations	61
4.4	Characteristic length scales and adaptive algorithm	62
4.4.1	Physical length scales	63
4.4.2	Numerical length scales	64
4.4.3	Onset, transition and global instability stages	65
4.4.4	The adaptive algorithm	66
4.5	Numerical formulations of the different stages	67
4.5.1	Original discretization	67

4.5.2	Local solution	67
4.5.3	DMSFV in transition stage	68
4.6	Numerical simulations	71
4.6.1	Problem definition and reference solutions	71
4.6.2	Adaptive simulations	73
4.7	Conclusions	79
5	Conclusions and outlook	83
5.1	Conclusions	83
5.2	Outlook	85
	Bibliography	87
	Curriculum Vitae	93

Résumé

Les instabilités engendrées par des gradients de densité interviennent dans une variété d'écoulements. Un exemple est celui de la séquestration géologique du dioxyde de carbone en milieux poreux. Ce gaz est injecté à haute pression dans des aquifères salines et profondes. La différence de densité entre la saumure saturée en CO_2 dissous et la saumure environnante induit des courants favorables qui le transportent vers les couches géologiques profondes. Les gradients de densité peuvent aussi être la cause du transport indésirable de matières toxiques, ce qui peut éventuellement conduire à la pollution des sols et des eaux. La gamme d'échelles intervenant dans ce type de phénomènes est très large. Elle s'étend de l'échelle poreuse où les phénomènes de croissance des instabilités s'opèrent, jusqu'à l'échelle des aquifères à laquelle interviennent les phénomènes à temps long. Une reproduction fiable de la physique par la simulation numérique demeure donc un défi en raison du caractère multi-échelles aussi bien au niveau spatial et temporel de ces phénomènes. Il requiert donc le développement d'algorithmes performants et l'utilisation d'outils de calculs modernes.

En conjugaison avec les méthodes de résolution itératives, les méthodes multi-échelles permettent de résoudre les grands systèmes d'équations algébriques de manière efficace. Ces méthodes ont été introduites comme méthodes d'upscaling et de downscaling pour la simulation d'écoulements en milieux poreux afin de traiter de fortes hétérogénéités du champ de perméabilité. Le principe repose sur l'utilisation parallèle de deux maillages, le premier est choisi en fonction de la résolution du champ de perméabilité (grille fine), alors que le second (grille grossière) est utilisé pour approximer le problème fin à moindre coût. La qualité de la solution multi-échelles peut être améliorée de manière itérative pour empêcher des erreurs trop importantes si le champ de perméabilité est complexe. Les méthodes adaptatives qui restreignent les procédures de mise à jour aux régions à forts gradients permettent de limiter les coûts de calculs additionnels. Dans le cas d'instabilités induites par des gradients de densité, l'échelle des phénomènes varie au cours du temps. En conséquence, des méthodes multi-échelles adaptatives sont requises pour tenir compte de cette dynamique.

L'objectif de cette thèse est de développer des algorithmes multi-échelles adaptatifs et efficaces pour la simulation des instabilités induites par des gradients de densité. Pour cela, nous nous basons sur la méthode des volumes finis multi-échelles (MsFV) qui offre l'avantage de résoudre les phénomènes de transport tout en conservant la masse de manière exacte. Dans la première partie, nous pouvons démontrer que les approximations de la méthode MsFV engendrent des phénomènes de digitation non-physiques dont la suppression requiert des opérations de correction itératives. Les coûts de calculs additionnels de ces opérations peuvent toutefois être compensés par des méthodes adaptatives. Nous proposons aussi l'utilisation de la méthode MsFV comme méthode de downscaling : la grille grossière étant utilisée dans les zones où l'écoulement est relativement homogène alors que la grille plus fine est utilisée pour résoudre les forts gradients. Dans la seconde partie, la méthode multi-échelle est étendue à un nombre arbitraire de niveaux. Nous prouvons que la méthode généralisée est performante pour la résolution de grands systèmes d'équations algébriques.

Dans la dernière partie, nous focalisons notre étude sur les échelles qui déterminent l'évolution des instabilités engendrées par des gradients de densité. L'identification de la structure locale ainsi que globale de l'écoulement permet de procéder à un upscaling des instabilités à temps long alors que les structures à petite échelle sont conservées lors du déclenchement de l'instabilité. Les résultats présentés dans ce travail permettent d'étendre les connaissances des méthodes MsFV et offrent des formulations multi-échelles efficaces pour la simulation des instabilités engendrées par des gradients de densité.

Abstract

Density-driven instabilities in porous media are of interest for a wide range of applications, for instance, for geological sequestration of CO_2 , during which CO_2 is injected at high pressure into deep saline aquifers. Due to the density difference between the CO_2 -saturated brine and the surrounding brine, a downward migration of CO_2 into deeper regions, where the risk of leakage is reduced, takes place. Similarly, undesired spontaneous mobilization of potentially hazardous substances that might endanger groundwater quality can be triggered by density differences. Over the last years, these effects have been investigated with the help of numerical groundwater models. Major challenges in simulating density-driven instabilities arise from the different scales of interest involved, i.e., the scale at which instabilities are triggered and the aquifer scale over which long-term processes take place. An accurate numerical reproduction is possible, only if the finest scale is captured. For large aquifers, this leads to problems with a large number of unknowns. Advanced numerical methods are required to efficiently solve these problems with today's available computational resources.

Beside efficient iterative solvers, multiscale methods are available to solve large numerical systems. Originally, multiscale methods have been developed as upscaling-downscaling techniques to resolve strong permeability contrasts. In this case, two static grids are used: one is chosen with respect to the resolution of the permeability field (fine grid); the other (coarse grid) is used to approximate the fine-scale problem at low computational costs. The quality of the multiscale solution can be iteratively improved to avoid large errors in case of complex permeability structures. Adaptive formulations, which restrict the iterative update to domains with large gradients, enable limiting the additional computational costs of the iterations. In case of density-driven instabilities, additional spatial scales appear which change with time. Flexible adaptive methods are required to account for these emerging dynamic scales.

The objective of this work is to develop an adaptive multiscale formulation for the efficient and accurate simulation of density-driven instabilities. We consider the Multiscale Finite-Volume (MsFV) method, which is well suited for simulations including the solution of transport problems as it guarantees a conservative velocity field. In the first part of this thesis, we investigate the applicability of the standard MsFV method to density-driven flow problems. We demonstrate that approximations in MsFV may trigger unphysical fingers and iterative corrections are necessary. Adaptive formulations (e.g., limiting a refined solution to domains with large concentration gradients where fingers form) can be used to balance the extra costs. We also propose to use the MsFV method as downscaling technique: the coarse discretization is used in areas without significant change in the flow field whereas the problem is refined in the zones of interest. This enables accounting for the dynamic change in scales of density-driven instabilities.

In the second part of the thesis the MsFV algorithm, which originally employs one coarse level, is extended to an arbitrary number of coarse levels. We prove that this keeps the MsFV method efficient for problems with a large number of unknowns. In the last part of this

thesis, we focus on the scales that control the evolution of density fingers. The identification of local and global flow patterns allows a coarse description at late times while conserving fine-scale details during onset stage. Results presented in this work advance the understanding of the Multiscale Finite-Volume method and offer efficient dynamic multiscale formulations to simulate density-driven instabilities.

Acknowledgments

“There is no real ending. It’s just the place where we stop the story.”

Frank Herbert, Science Fiction Author

A Ph.D. study is a fruitful and instructive time that sometimes feels like Frodo’s bumpy road to Mount Doom (just as plenty of other things sometimes feel, too). The fact that my story stops here, is especially due to the help of several persons, to whom I herewith want to express my gratitude:

This is at first and foremost my supervisor Prof. Ivan Lunati for guiding the thesis, for his support as well as for the long and regular discussions, which helped improving the quality of the single articles. His doors were always open, in times of disagreement as wide as in times of agreement, and he was always ready to find good solutions. I also want to thank him for giving me twice the chance to spend several months at Chevron Energy Technology Company in California, USA.

At second, these thanks go to Dr. Pavel Tomin who often helped me with his useful comments, suggestions and critics no matter what time of the day or day of the week. Equally, I want to thank Dr. Seong H. Lee from Chevron Energy Technology Company for being my advisor during my internship in California and inviting me for a second summer as well as for being a wonderful host during this time. I also want to express my gratitude to Prof. Klaus Holliger, Prof. Patrick Jenny, Prof. Niklas Linde and Prof. Eric Verrecchia for agreeing to be member of my Ph.D. committee.

Additional thanks are due to Dr. Marc-Antoine Habisreutinger for revising the French form of the abstract and making it readable for native French speakers. Further thanks are going to Tobias Lochbühler and to Laureline Josset for proof reading the thesis before handing in as well as to Dr. Caroline Dorn for providing user-friendly LaTeX templates.

Deep thanks are due to my family (Mum, Dad, ...), since without their help and support life would have been much more difficult. "Un grand merci" also to Caroline, Florian, Rolf and Tobias for discussing, skiing, swimming, and good evening meals. All of that made the last four years a special time for me.

Finally, I am especially thankful to Lena whose support over the last four years was priceless. She stood my fretfulness when times were tough and, despite the geographical gap between us, she never lost her patience with me.

Chapter 1

Introduction

1.1 Preamble

Density-driven instabilities can be observed in a wide range of everyday phenomena. For example, colourful flow patterns in lava lamps, illustrated in Fig. 1.1 (a), are formed due to the strong dependence of the green fluid's density on the temperature: the heating at the bottom of the container leads to a density difference between the two fluids with an upward movement of the lighter green phase to the top of the container where it cools down. Comparable to the heating process, cooling causes a density increase and a downward movement to the bottom of the container where it restarts to heat up. This initiates a continuous recirculation of the two fluids.



Figure 1.1: Everyday examples of density-driven instabilities: (a) Lava lamp with density differences caused by heating the fluids at the bottom; (b) Tequila sunrise cocktail where density differences are due to chemical properties of the fluids.

Similar effects can be observed in cocktail bars. In the example shown in Fig. 1.1 (b), the

grenadine added to the orange juice tequila mixture has a higher density and therefore starts percolating down in form of small fingers. In contrast to the lava lamp, the flow takes place through a porous media formed by the ice-cubes. Beside the fluids' properties as viscosity and density, form and structure of the density fingers are a function of irregularities in the porous matrix.

In both cases, convection is induced solely by the density difference between the fluids and does not require additional external forces. Whereas in the illustrated examples this spontaneous convection represents no potential risk for its environment, density-driven instabilities that take place in groundwater aquifers can strongly influence the spreading of contaminants by remarkably decreasing travel times. For example, dense agricultural brine disposed in natural or artificial depressions can become unstable and intrude into the underlying freshwater aquifer [69]. In arid regions, this particularly endangers the quality of tight freshwater. Similar to the lava lamp example illustrated in Fig. 1.1 (a), stabilizing recirculation of the downward moving brine can be observed due to geothermal heating at deep regions, e.g., [12]. Another potential danger originates from Dense-Non-Aqueous-Phase Liquids (DNAPLs) that have been frequently used in industry without sufficient care and that slowly infiltrate into the groundwater system [31].

In the same way, favourable displacements can be caused by density differences: in the process of CO₂ sequestration, CO₂ is captured from large sources instead of being released to the atmosphere and injected at high pressure into deep geological formations; flow instabilities can displace the dissolved CO₂ into deeper regions. In these deep regions the danger of leakage is decreased and potential risks are minimized [43, 63, 65, 66]. To correctly understand and evaluate the environmental impact of the above-mentioned problems (other good examples of density-driven flow processes in porous media can be found in [13, 33]) and to prevent health hazards, accurate numerical simulations are essential.

Simulations of flow and transport include several steps of abstraction. First, the real physical processes need to be described by mathematical models, which leads to a set of differential equations. Due to the complexity of the equations, analytical solutions are rare or exist only for simplistic benchmark problems [33]. Numerical solutions that describe the continuous flow domain by a finite number of nodes, are therefore required. Whereas in general the number of discrete points is chosen according to the resolution of the permeability field, accurate numerical simulations of density-driven instabilities require discretizations that sufficiently resolve the critical wavelength [63], which is the smallest perturbation in the initial base state that is not damped by diffusive processes [20].

For large flow domains, large numerical systems with computationally very expensive solutions are the consequence of highly resolving the critical wavelength and advanced numerical methods are needed. Beside iterative solvers, multiscale techniques belong to this type of methods. In this work, the multiscale concept will be tested and extended to match the challenges that arise from the simulation of density-driven instabilities. The Multiscale Finite-Volume method [36], which has proven an efficient upscaling-downscaling technique for flow problems

in porous media, is used as basis for our investigations.

1.2 Analytical formulations

1.2.1 Single-phase flow and transport

Flow through porous media is described by Darcy's law

$$\mathbf{v} = -\frac{\mathbf{k}}{\mu} [\nabla p - \rho(c)\mathbf{g}], \quad (1.1)$$

where \mathbf{v} [m/s] is the Darcy velocity (volumetric flux per unit surface), \mathbf{k} [m²] is the permeability tensor of the porous medium; p [Pa] the pressure; \mathbf{g} [m/s²] the gravity acceleration; and μ [kg/m/s] and ρ [kg/m³] the viscosity and density of the fluid, respectively, which can be a function of the normalized concentration c [-] (see e.g., [5]). For an incompressible fluid and porous matrix, the mass conservation equation has the form

$$\nabla \cdot \mathbf{v} = r, \quad (1.2)$$

where the velocity \mathbf{v} [m/s] is given by Eq. (1.1) and r is the right hand side term containing sources and sinks. According to the Boussinesq approximation [33], changes in density are neglected in Eq. (1.2), except for its contribution to the gravity term.

By substituting Eq.(1.1) into Eq.(1.2) we obtain an elliptic equation for the unknown pressure p . To close the system of equations, a mass conservation equation for the solute is formulated as

$$\frac{\partial}{\partial t}(\phi c) + \nabla \cdot [c\mathbf{v} - (D_m + \mathbf{D}_d)\nabla c] = q, \quad (1.3)$$

where c [-] is the normalized concentration, ϕ [-] the porosity of the porous matrix, q [1/s] the right-hand-side source term, D_m [m²/s] the coefficient of molecular diffusion and \mathbf{D}_d [m²/s] the tensor of hydrodynamic dispersion.

1.2.2 Multiphase flow

When two immiscible fluids simultaneously flow in the pore space, we have to write a mass conservation equation for each fluid

$$\frac{\partial}{\partial t}(\phi S_\gamma) + \nabla \cdot \mathbf{v}_\gamma = q_\gamma, \quad \gamma = 1, 2, \quad (1.4)$$

where γ denotes the phase, S_γ [-] the phase saturation and q_γ [1/s] the corresponding sources and sinks. The phase velocity, \mathbf{v}_γ [m/s], is described by the generalized form of Darcy's law,

$$\mathbf{v}_\gamma = -\lambda_\gamma \mathbf{k} (\nabla p_\gamma - \rho_\gamma \mathbf{g}) \quad (1.5)$$

where the phase mobility, $\lambda_\gamma = k_{r\gamma}(S_\gamma)/\mu_\gamma$ [m·s/kg], contains the relative permeability function $k_{r\gamma}(S_\gamma)$ [-], which accounts for the resistance force exerted by the solid (see e.g., [31]). By summing up the two mass-balance equations we obtain the elliptic pressure equation,

$$-\lambda_{tot}\mathbf{k}\left(\nabla p_1 - \sum_{\gamma} f_{\gamma}\rho_{\gamma}\mathbf{g} + f_2 p_c\right) = q_{tot} \quad (1.6)$$

where $\lambda_{tot} = \lambda_1 + \lambda_2$ [m·s/kg] is the total mobility, $q_{tot} = q_1 + q_2$ [1/s] the total source term, $f_\gamma = \lambda_\gamma/\lambda_{tot}$ [-] the fractional flow function and where the capillary pressure $p_c(S_\gamma)$ [Pa] is a function of the saturation (see e.g., [4]). Eqs. (1.4) to (1.6) as well as Eqs. (1.1) to (1.3) build a non-linear system of differential equations that are coupled by the concentration and the saturation, respectively.

1.3 Numerical discretization

1.3.1 Finite-Volume method

Several discretization techniques such as finite differences or finite elements are used to simulate flow and transport in porous media. They are based on a discretization of the flow domain, Ω , into a finite number of points that enable constructing discrete approximations to the continuous problem (see Fig. 1.2). In contrast to finite differences or finite elements, a finite-volume discretization method has the advantage of conserving mass.

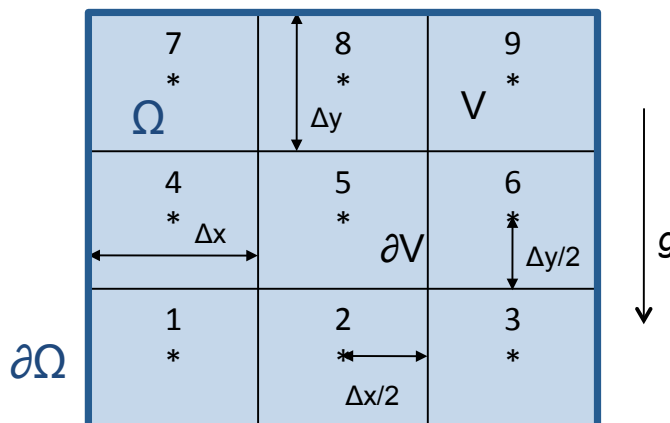


Figure 1.2: Vertex centered finite-volume discretization of a 2D flow domain Ω with the control volumes V and control-volume surface ∂V . The domain boundary is indicated by $\partial\Omega$.

Mass conservation in finite volumes is guaranteed by dividing the domain into a finite number of control volumes that allow the formulation of a number of discrete mass-balance equations. Discrete mass-balance equations are constructed by integrating the continuous pressure or transport equation over the control volumes. For example, the elliptic single-phase pressure

equation, obtained by inserting Eq. (1.1) into Eq. (1.2), is integrated over the cell volume, V ,

$$-\int_V \nabla \cdot \left[\frac{\mathbf{k}}{\mu} (\nabla p - \rho(c)\mathbf{g}) \right] dV = \int_V r dV. \quad (1.7)$$

Applying the divergence theorem to the left-hand-side allows transforming the volume integral into a surface integral and we write

$$-\int_{\partial V} \frac{\mathbf{k}}{\mu} (\nabla p - \rho(c)\mathbf{g}) \mathbf{n} dA = \int_V r dV, \quad (1.8)$$

where \mathbf{n} is the normal vector perpendicular to the surface. From Eq. (1.8) it can be seen that the net flux contribution over the control surface has to be equal to the contribution from sources and sinks assigned to the control volume ("what flows in has to flow out").

Expressing the continuous surface, ∂V , as the union of the cell faces and using a first-order, centred approximation to describe the pressure gradient, ∇p , the discrete single-phase mass balance equation for, e.g., the control volume 5 in Fig. 1.2, is

$$A \frac{k_{4,5}}{\mu} \frac{p_5 - p_4}{\Delta x} + A \frac{k_{5,6}}{\mu} \frac{p_5 - p_6}{\Delta x} + A \frac{k_{2,5}}{\mu} \left(\frac{p_5 - p_2}{\Delta y} - \rho_{2,5}g \right) + A \frac{k_{5,8}}{\mu} \left(\frac{p_5 - p_8}{\Delta y} - \rho_{5,8}g \right) = 0, \quad (1.9)$$

where the four terms on the left-hand-side describe the fluxes over the four cell faces, A is the face area, and Δx and Δy are the center-to-center distances in x - and y -direction, respectively (see e.g., [30]). We assumed zero sources and sinks in cell 5. Notice that variables with two indices have to be evaluated with respect to the common interface of the corresponding cells. While face-based permeability values are in general obtained by an harmonic mean, a linear interpolation is used to calculate the face-based densities that are functions of the node-based concentration values. The latter gives an accurate approximation of $\rho(c)$ for moderate dependences of density on concentration.

The discrete flow system requires the assignment of boundary conditions on the domain boundary, $\partial\Omega$. Two main types of boundary conditions are distinguished: Dirichlet or first type and Neumann or second type boundary conditions. Dirichlet boundary conditions assign a known pressure value to the domain boundary. For example, a Dirichlet type boundary condition on the western face of cell 1 leads to the discrete unknown flux term $A \frac{k_1}{\mu} \frac{p_1 - p_{BC}}{\Delta x/2}$. In contrast, Neumann boundary conditions assign a known flux to the domain boundaries.

Formulating a mass balance equation for each control volume leads to the following algebraic system

$$\mathbf{A}\mathbf{p} = \mathbf{r}(c) \quad (1.10)$$

where the matrix \mathbf{A} contains the transmissibilities $Ak_{i,j}/\mu/\Delta s$ with $\Delta s = \Delta x$ or $\Delta s = \Delta y$ in 2D; and where $\mathbf{p} = [p_1 \ p_2 \ \dots \ p_n]^T$ and $\mathbf{r} = [r_1 \ r_2 \ \dots \ r_n]^T$ are the pressure and the right-

hand-side vectors, respectively. The latter contains, beside gravity effects and boundary terms, contributions from sources and sinks. Notice that i and j are the cell indices in x - and y -direction, and n is the total number of unknowns. For a first-order centered flux approximation, \mathbf{A} contains 5 non-zero bands in 2D and 9 non-zero bands in 3D.

Using a standard backward Euler scheme [31] for the time derivative and a first-order centred approximation for the diffusion-dispersion gradient, we write the discrete solute mass-balance equation for volume 5, Eq. (1.1), as

$$\begin{aligned} V \frac{(c_5^t - c_5^{t-1})}{\Delta t} + Av_{4,5}c_{4,5}^t + AD_{4,5} \frac{c_5^t - c_4^t}{\Delta x} + Av_{5,6}c_{5,6}^t + AD_{5,6} \frac{c_5^t - c_6^t}{\Delta x} \\ + Av_{2,5}c_{2,5}^t + AD_{2,5} \frac{c_5^t - c_2^t}{\Delta y} + Av_{5,8}c_{5,8}^t + AD_{5,8} \frac{c_5^t - c_8^t}{\Delta y} = 0, \end{aligned} \quad (1.11)$$

where t is the time index and $D_{i,j}$ is the dispersion-diffusion coefficient. In advection dominated problems, concentration values at cell faces are in general calculated by upwind schemes, e.g., [31]. Upwind schemes account for the direction in which a temporal change in concentration propagates. It therefore evaluates the unknown concentration with respect to the cell from which the information is coming. For instance, if the flow is directed from cell 4 into cell 5, the convective mass flux between cell 4 and 5 is given in a first order upwind scheme as $Av_{4,5}c_4$.

The transport system can then be written as

$$(\mathbf{V} + \mathbf{U} + \mathbf{D})\mathbf{c}^t = \mathbf{T}\mathbf{c}^t = \mathbf{V} \frac{\mathbf{c}^{t-1}}{\Delta t} + \mathbf{q} \quad (1.12)$$

where \mathbf{V} is the diagonal accumulation operator that contains contributions from the time derivative, $V\phi/\Delta t$, \mathbf{U} the convective operator that includes the flux contributions $Av_{i,j}$, and \mathbf{D} the diffusion-dispersion operator that contains the entries $AD_{i,j}/\Delta s$.

The pressure system, Eq. (1.9), can be easily adapted to two-phase flow by adding the corresponding total mobilities or fractional flow functions, substituting the concentration by the saturation and including capillary pressure terms and gravity effects into the right hand side term, i.e.,

$$\mathbf{A}\mathbf{p}_\gamma = \mathbf{r}(\mathbf{S}_\gamma). \quad (1.13)$$

Using a standard quadratic relative permeability-saturation relationship $k_{r\gamma}(S_\gamma) = S_\gamma^2$, the transport system has the non-linear form

$$(\mathbf{V} + \mathbf{D})\mathbf{S}_\gamma^t + \mathbf{U}\mathbf{k}_{r\gamma}(\mathbf{S}_\gamma^t) = \mathbf{q} + \mathbf{V} \frac{\mathbf{S}_\gamma^{t-1}}{\Delta t}, \quad (1.14)$$

where γ is again the phase index.

1.3.2 MaFloT and MaFloTT

A wide range of commercial and non-commercial flow simulators are available to solve the discretized flow problems (see e.g., [27, 64]). They offer different strategies to resolve the coupling between the pressure and transport equation. In fully implicit methods Eq. (1.10) and Eq. (1.12) or Eq. (1.13) and Eq. (1.14), respectively, are solved together. As the merged flow operator contains twice the number of unknowns with additional bands, sequentially implicit schemes that decouple the two equations and iteratively update the coupled variables, are often preferred.

In this work, we employ for single-phase flow and transport the simulation software MaFloT (Matlab Flow and Transport) [47], that we designed as didactic code (the code can be downloaded under the conditions of the GPL licence [71] from the webpage given in the reference). MaFloT uses a sequentially implicit scheme that writes Eq. (1.10) as

$$\mathbf{A}(\mathbf{c}^{t,\nu-1})\mathbf{p} = \mathbf{r}(\mathbf{c}^{t,\nu-1}) \quad (1.15)$$

and Eq. (1.12), respectively, as

$$\mathbf{T}\mathbf{c}^{t,\nu} = V\frac{\mathbf{c}^{t-1}}{\Delta t} + \mathbf{q}. \quad (1.16)$$

In Eq. (1.15) and Eq. (1.16), ν is the iteration index. The concentration vector, $\mathbf{c}^{t,\nu}$, is iteratively updated until convergence to a user-defined threshold is achieved.

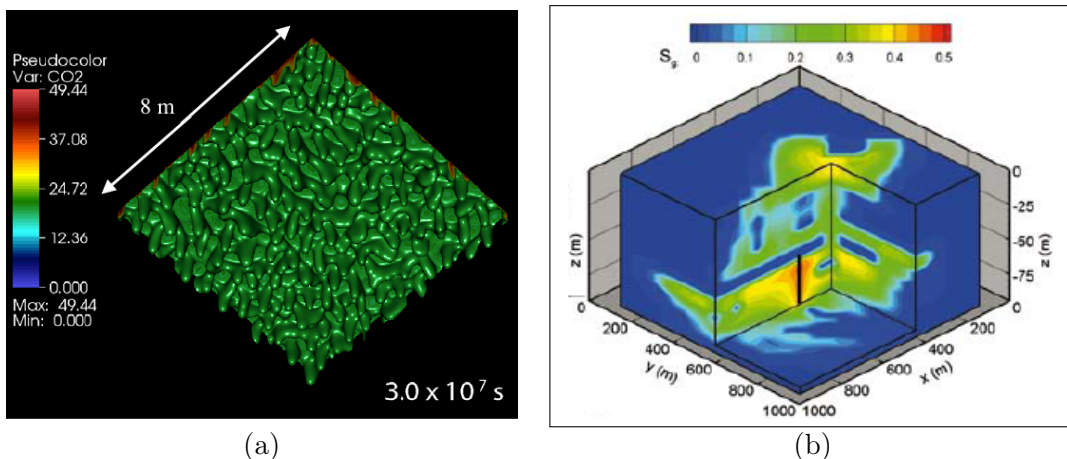


Figure 1.3: The different scales in simulating density-driven flow in porous media: (a) A view from below on the simulated CO₂ concentration isosurface for the 3D diffusion-convection process at time where initial instabilities start to merge (taken from [63]); (b) Field-scale model for the sequestration of CO₂ in a heterogeneous formation with low permeability layers (taken from [14]).

In addition, we designed MaFloTT, a sequentially implicit finite-volume algorithm to simulate two-phase flow in porous media including capillary pressure. It employs a p_γ - S_γ formulation and users can choose between *van Genuchten* or *Brooks-Corey* capillary pressure model [31].

Non-linearities are resolved by a Newton-Raphson [61] scheme,

$$(\mathbf{V} + \mathbf{D})\mathbf{S}^t + \frac{d\mathbf{U}(\mathbf{S}^{t,\nu-1})}{d\mathbf{S}}\mathbf{S}^{t,\nu} = V\frac{\mathbf{S}^{t-1}}{\Delta t} + \mathbf{q} - \mathbf{U}(\mathbf{S}^{t,\nu-1}) + \frac{d\mathbf{U}(\mathbf{S}^{t,\nu-1})}{d\mathbf{S}}\mathbf{S}^{t,\nu-1}. \quad (1.17)$$

Results obtained from MaFloT and MaFloTT will be used throughout this work as reference solution to evaluate newly devised multiscale formulations.

1.4 Challenges in modelling density-driven instabilities

The choice of the grid size on which the continuous problem is discretized is subject to several conditions: small cells limit numerical errors and enable resolving the physical processes with higher accuracy, but they involve a large number of unknowns. Especially in case of density-driven instabilities, modellers face this conflict as small-scale irregularities dominate the onset of instabilities (see Fig. 1.3 (a)). For instance, for the aquifer illustrated in Fig. 1.3 (b) and a cell volume of 10^{-3} m^3 , each of the linear systems given in Eq. (1.15) and Eq. (1.16) consists of 10^{12} unknowns. Direct solution of a problem of this size is impossible with today's computational resources. Methods that reduce the computational costs are therefore required.

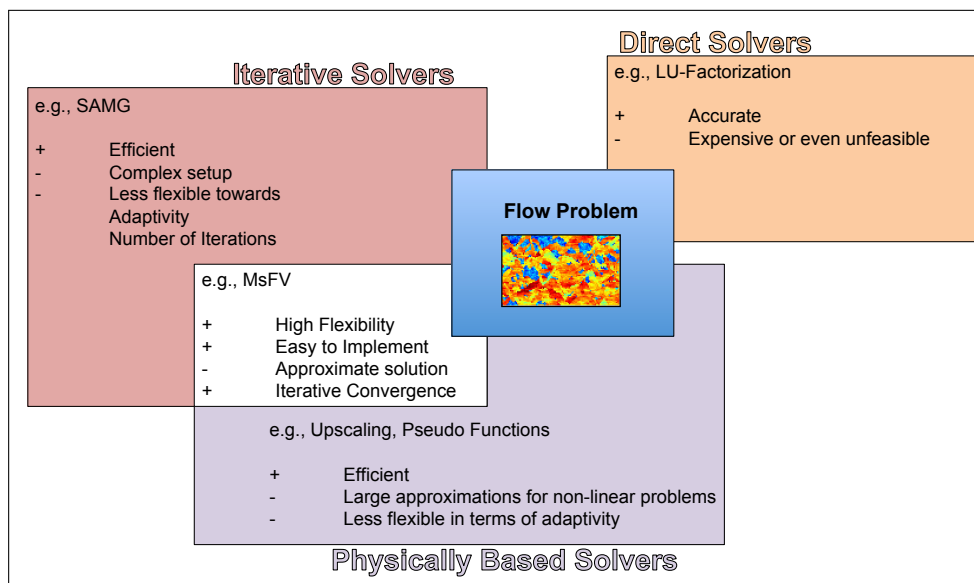


Figure 1.4: State-of-the-art solvers for banded linear elliptic systems.

Many numerical formulations have been developed over the last decades. While for advection dominated transport problems domain decomposition techniques with iterative update of the local boundary conditions have been shown to perform very well [68], elliptic pressure equations require more sophisticated solutions. In general, efficient state-of-the-art solvers for the elliptic pressure system can be classified in two groups (see Fig. 1.4): iterative solvers that

deliver solutions with accuracy comparable to direct solvers (e.g., [68, 72]); or physically based methods such as upscaling schemes [6, 41] or pseudo function formulations [35, 48] that calculate a non-iterative, approximated solution to the original flow problem. For complex flow problems the approximate, non-iterative solutions can be inaccurate. A common drawback of both type of solvers is the low flexibility with respect to adaptive formulations: while upscaling techniques do not allow to locally improve the approximate solution, iterative solvers employ a fully converged solution for the entire domain.

Over the last years, multiscale methods [8, 15, 34, 36] have received more and more attention. Similar to physically-based, non-iterative schemes, these methods approximate the original operator \mathbf{A} such that an efficient solution with respect to the original discretization can be formulated. In contrast to other approximate solvers, the multiscale solution can be iteratively improved to achieve the desired level of accuracy. These two characteristics of multiscale solvers make the method highly flexible with respect to adaptive formulations: accurate fine-scale solutions can be limited to the regions of interest, e.g., regions of instability onset, and the level of accuracy can be arbitrarily chosen.

1.5 MsFV: concept, findings and limitations

Comparable to other multiscale techniques, the Multiscale Finite-Volume (MsFV) method [23, 36, 37, 52, 55, 57, 58] has the advantage that a fully conservative fine-scale velocity field can be constructed from the approximate pressure solution at every time. It is therefore well suited for numerical simulations that require solving a transport problem.

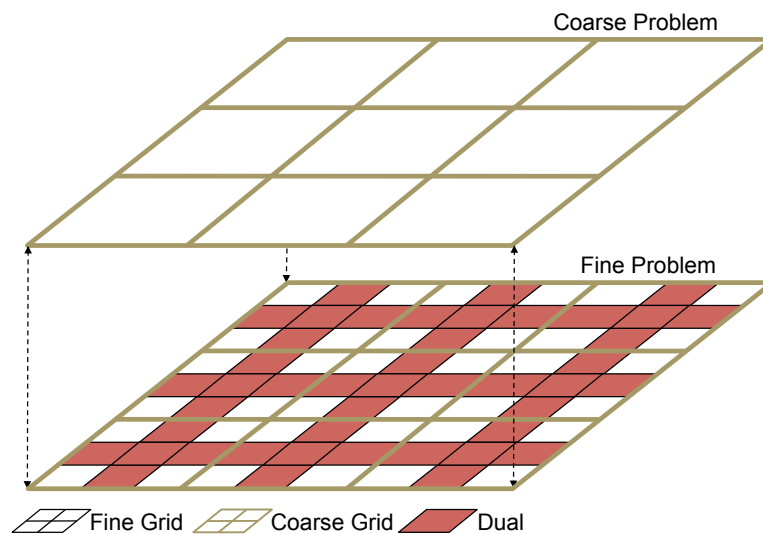


Figure 1.5: MsFV fine, coarse and dual coarse grid.

The Multiscale Finite-Volume method first projects the original problem onto a coarser grid where it is cheaper to solve and then prolongates the upscaled solution back to the fine

grid, see Fig. 1.5. The interpolators used for the projection and prolongation are the solution of local flow problems, defined with respect to a staggered (dual) coarse grid. The dual grid is constructed by connecting the centers of the coarse cells as illustrated in Fig. 1.5. Localization is realized by assigning constant transversal fluxes on dual boundaries. Mass conservation of the coarse solution, which is the main characteristic of the MsFV method, is guaranteed by the consistency between coarse and fine-scale fluxes. The approximate pressure on the fine-grid can finally be represented as a linear combination of the coarse node pressures multiplied by the local interpolators.

Even though the approximated fine-scale solution is, due to the localization assumptions necessary to compute local interpolators, non-conservative on dual boundaries, mass conservation of the coarse solution always allows to reconstruct a fully conservative fine-scale velocity field. This is achieved by solving another set of local problems that are defined with respect to the coarse grid and using the multiscale pressure solution to construct Neumann boundary conditions.

In the first publication on the Multiscale Finite-Volume method [36], the quality of the local interpolators was demonstrated for multiphase flow without capillary pressure or density effects. Errors to reference solutions were minor and promising results were achieved without iterative correction of the pressure solution. From there on, the MsFV method has been extended to compressible flow [52, 54], to include density or capillary pressure terms [56] or for modelling complex wells [38, 74].

In particular, tests with complex permeability fields or large grid anisotropies [54] revealed the weakness of the approximation assumption and showed large errors compared to the reference fine-scale solutions. To guarantee sufficient accuracy for these applications, the multiscale operators can be used as two-stage preconditioner [58] in iterative schemes. Convergence is guaranteed by an appropriate choice of the relaxation parameter [68]. Using the MsFV concept in this context raises the obvious question of how efficiently it performs when compared to existing iterative methods like Algebraic Multigrid [72]. Iterative performances have been investigated in detail in e.g., [26, 76]. It must be noted that the question of the best performing smoother in conjunction with the multiscale operator is still not completely resolved.

If the initial multiscale solution is iteratively corrected to represent mass conservation with sufficient accuracy, the reconstruction procedure can be omitted. The reconstruction step however, allows stopping the iterative update at any iteration while being able to construct a fully conservative fine-scale velocity field. In comparison to other approximation methods or iterative solvers, the Multiscale Finite-Volume method gives the possibility to balance accuracy and efficiency as desired by the modeller or required by the problem.

1.6 Objectives

The standard MsFV method was mainly developed to efficiently describe the effect of strong heterogeneities. That is to say that the scales of interest are given by the static permeability

field and by the number of unknowns that can be efficiently handled. In this work, we focus on spontaneous instabilities. Characteristic scales are defined by the physical processes and change continuously. Therefore, multiscale formulations that dynamically resolve different spatial scales are required. This leads to the following objectives of this work:

- Investigate the effects of the approximations in MsFV on density-driven instabilities and apply adaptive strategies to balance the additional costs of the iterative extension that is necessary to reproduce fine-scale results.
- Develop an efficient downscaling technique that is based on the MsFV concept and that allows to locally resolve the scales of interest.
- Extend the MsFV concept to more than one level of coarsening, which is necessary to keep the method efficient for very large problems in future applications.
- Investigate the level of local and global information required to reproduce density-driven instabilities in a statistical prospective.

The work is structured as follows: first we demonstrate that the localization assumption in case of density-driven instabilities provokes spurious fingers and we show how they can be controlled by the iterative MsFV (iMsFV) method. To balance the additional costs, we use adaptive strategies for iMsFV and for the reconstruction procedure. Coarse cells in which iterative improvements and velocity reconstructions are required, are identified on the basis of the local concentration or saturation field. This requires adaptive multiscale formulations of the transport equation. A standard Schwarz decomposition scheme [70] is provided. With these adaptive schemes we transfer the MsFV method into an efficient downscaling technique that enables resolving critical wavelengths for density-driven instabilities. Further, we derive a new multilevel concept that uses a nested reconstruction procedure to guarantee a conservative velocity field. Finally, we use a local and global extension of the downscaling concept to statistically reproduce ensemble fine-scale simulation results.

The results presented in this work provide new insight into the existing (i)MsFV method, show new developments of MsFV, and employ efficient strategies for the simulation of density-driven instabilities.

Chapter 2

An adaptive multiscale method for density-driven instabilities

Rouven Künze, and Ivan Lunati

published in *Journal of Computational Physics*¹

¹R. Künze, and I. Lunati. An adaptive multiscale method for density-driven instabilities. *Journal of Computational Physics*, 231(17):5557–5570, 2012.

2.1 Abstract

Accurate modeling of flow instabilities requires computational tools able to deal with several interacting scales, from the scale at which fingers are triggered up to the scale at which their effects need to be described. The Multiscale Finite-Volume (MsFV) method offers a framework to couple fine- and coarse-scale features by solving a set of localized problems which are used both to define a coarse-scale problem and to reconstruct the fine-scale details of the flow. The MsFV method can be seen as an upscaling-downscaling technique, which is computationally more efficient than standard discretization schemes and more accurate than traditional upscaling techniques. We show that, although the method has proven accurate in modeling density-driven flow under stable conditions, the accuracy of the MsFV method deteriorates in case of unstable flow and an iterative scheme is required to control the localization error. To avoid large computational overhead due to the iterative scheme, we suggest several adaptive strategies both for flow and transport. In particular, the concentration gradient is used to identify a front region where instabilities are triggered and an accurate (iteratively improved) solution is required. Outside the front region the problem is upscaled and both flow and transport are solved only on the coarse scale. This adaptive strategy leads to very accurate solutions at roughly the same computational cost as the non-iterative MsFV method. In many circumstances, however, an accurate description of flow instabilities requires a refinement of the computational grid rather than a coarsening. For these problems, we propose a modified iterative MsFV, which can be used as downscaling method (DMsFV). Compared to other grid refinement techniques the DMsFV clearly separates the computational domain into refined and non-refined regions, which can be treated separately and matched later. This gives great flexibility to employ different physical descriptions in different regions, where different equations could be solved, offering an excellent framework to construct hybrid methods.

2.2 Introduction

Flow instabilities are common at displacement fronts between miscible or immiscible fluids. Gravity-driven instabilities in porous media, for instance, can be found during saltwater intrusion on coastal aquifers [33], water infiltration in dry soils [22, 59], contamination of groundwater resources [28, 29], or geological storage of carbon dioxide [18, 19, 43, 66]. Depending on the density contrast, these instabilities, which are triggered by small-scale perturbations, can heavily affect large-scale flow and transport. Convective instabilities can, for instance, increase dissolution rates of CO₂ that favours solution trapping, or reduce contaminant travel times leading to a higher risk of groundwater pollution. It is therefore important to accurately simulate the triggering mechanisms and the dynamic growth, to correctly predict instabilities and their consequences.

This is not a simple task because in most applications (particularly in those dealing with geological porous media) large differences exist between the scale at which the instability is

triggered and the scale at which the problem needs to be described. This disparity of scales makes it computationally impossible to describe the system with the required resolution and coarsening techniques are required. Standard upscaling techniques are not suitable in case of instabilities (or more generally nonlinear processes) because they average out small-scale information. Multiscale methods, in contrast, solve a number of local (small-scale) problems that are coupled through a global (coarse) problem. The local problems are used both to upscale and downscale information, such that the small-scale details are retained.

Among several multiscale methods developed over the last years for flow in porous media, the Multiscale Finite-Volume (MsFV) method [36] has been successfully applied to describe physically complex flow including gravity effects [53, 54, 56]. Although the MsFV method provides very accurate solutions in case of stable interfaces [54, 56], in this paper we show that the quality of the solution deteriorates in presence of instabilities because small errors are amplified with time. Accurate simulation of instabilities requires controlling the MsFV error that originates from the assumption used to define the local problems. This can be done by iteratively improving the boundary conditions of the localized problems [58], paying the price of higher computational costs.

The computational overload, however, can be limited by introducing several adaptive criteria. In particular, an accurate solution is sought only in regions where the front is located and the flow is potentially unstable, whereas coarse solutions are computed in the rest of the domain. This subdivision between regions of different accuracy makes the method suitable to be modified into a downscaling technique: the iterative MsFV (iMsFV) method can be used to locally refine the original problem in critical regions of the domain (hence, achieving a higher accuracy). Although in the rest of the paper we concentrate on flow in porous media, the approach presented here is more general and is not limited to Darcy flow (for an example of the use of the MsFV method to Navier-Stokes see [7]).

2.3 Governing equations

We consider a solute that is dissolved in a solvent at concentration c (in the following we will assume that the concentration is normalized and varies between 0 and 1). Assuming incompressibility of the fluid and employing the Boussinesq approximation [33], the mass-balance equation of the solution in absence of sources and sinks is

$$\nabla \cdot \mathbf{v} = 0, \tag{2.1}$$

where

$$\mathbf{v} = -\frac{\mathbf{k}}{\mu(c)} [\nabla p - \rho(c)\mathbf{g}] \tag{2.2}$$

is the Darcy velocity (specific flux per unit area); \mathbf{k} the absolute permeability tensor; p the pressure; \mathbf{g} the gravity acceleration; μ and ρ the viscosity and density of the fluid, respectively, which depend on the concentration. The solute mass balance is governed by an advection-

dispersion equation of the form

$$\frac{\partial}{\partial t}(\phi c) + \nabla \cdot [c\mathbf{v} - (D_m + \mathbf{D}_d)\nabla c] = 0, \quad (2.3)$$

where ϕ is the porosity; D_m the molecular diffusion in the porous medium; and

$$\mathbf{D}_d = \alpha_T |\mathbf{v}| \mathbf{I} + (\alpha_L - \alpha_T) \frac{\mathbf{v} \otimes \mathbf{v}}{|\mathbf{v}|}, \quad (2.4)$$

the hydrodynamical (or mechanical) dispersion tensor [5]. In Eq. (2.4), α_L and α_T are the longitudinal and transversal dispersivities; and $|\mathbf{v}| = (\mathbf{v} \cdot \mathbf{v})^{1/2}$ is the absolute value of the Darcy velocity.

Eqs. (2.1) and (2.3) forms a system of nonlinear equations, which are coupled through the dependence of the viscosity and the density on the concentration. Although several relationships have been suggested for $\rho(c)$ and $\mu(c)$ in the literature (see, e.g., [33, 44]), simple linear relationships can be assumed for moderate density and viscosity differences (e.g., [2, 32]), i.e.,

$$\rho(c) = (1 - c)\rho_{\min} + c\rho_{\max} \quad \text{and} \quad \mu(c) = (1 - c)\mu_{\min} + c\mu_{\max}, \quad (2.5)$$

where ρ_{\min} and μ_{\min} (resp. ρ_{\max} and μ_{\max}) are the density and the viscosity at $c = 0$ (resp. $c = 1$).

2.4 Discretization and coupling

The system of Eqs. (2.1) and (2.3) is discretized by a finite-volume scheme with a backward Euler scheme for the time derivative. The discrete form of Eq. (2.1) can be written as

$$\mathbf{A}\mathbf{p} = \mathbf{r} \quad (2.6)$$

where \mathbf{p} is the unknown pressure vector; $\mathbf{A} = \mathbf{A}(\mathbf{c}^{n+1})$ the coefficient or stiffness matrix, which depends on the concentration vector at the new time step, \mathbf{c}^{n+1} , via the viscosity, Eq. (2.5); and $\mathbf{r} = \mathbf{r}(\mathbf{c}^{n+1})$ the right hand side vector, which contains boundary and gravity effects, and also depends on the concentration.

The discrete form of the transport equation, Eq. (2.3), is

$$\mathbf{T}\mathbf{c}^{n+1} = (\mathbf{V} + \mathbf{U} + \mathbf{D})\mathbf{c}^{n+1} = \mathbf{q}, \quad (2.7)$$

where \mathbf{V} is the diagonal accumulation operator arising from the time derivative; \mathbf{U} the discrete advection operator, which depends on the Darcy velocity; \mathbf{D} the discrete dispersion operator, which depends on the velocity; and \mathbf{q} the right hand side containing boundary effects, sources and sinks, and the term $-\mathbf{V}\mathbf{c}^n$. A MINMOD Flux Limiter method, which combines a first order upwind scheme with a higher order QUICK (Quadratic Upwind Interpolation for Convection Kinetics) scheme [50, 51], is used for the advection operator \mathbf{U} .

Eqs. (2.6) and (2.7) are solved with a sequential fully implicit scheme (see, e.g., [37]). First, a pressure solution is calculated using the concentration at the old time step and the resulting velocity field is used in the transport equation. Then, the new concentration is used to update the coefficient matrix and the right hand side in the pressure equation. The procedure is repeated until convergence.

2.5 The MsFV method

Instead of solving Eq. (2.6) exactly, the MsFV method seeks for an approximate solution that can be efficiently computed. At this end, an auxiliary coarse grid is employed together with its dual, which is constructed by connecting the coarse-cell centers. The construction of the dual grid defines a partition of the fine-grid cells into inner (i), edge (e) or node (n) cells (Fig. 2.1). The (primal) coarse grid defines the control volumes of a coarse-scale (global) problem, whose solution provides the approximate pressure at the center of the coarse cells (nodes); the dual (coarse) grid is used to define the basis functions, which are node-pressure interpolators [36], and the corrections functions, which are required for consistent treatment of the right hand side [38, 54, 56].

Due to the localization approximation, the velocity field obtained from the approximate pressure solution is non-conservative across dual-cell boundaries. Severe mass-balance errors are introduced if this field is used as advection velocity in a transport equation [36]. Therefore, the MsFV method constructs an approximate, fully conservative velocity field by using the approximate pressure gradient to assign Neumann boundary conditions of local problems solved in the coarse cells [36, 52]. Mass conservation is guaranteed by the consistency between the coarse-scale and the fine-scale fluxes across the boundaries of the coarse cells.

In the following we briefly recall how the approximate pressure solution is obtained and how it can be iteratively improved. We refer to [57, 58] for further details and for an extensive description of the construction of the conservative velocity field.

2.5.1 The MsFV pressure solution

To describe the MsFV method, we use an operator formulation [57] and order the N components of the pressure vector in Eq. (2.6) such that first inner, then edge, and last node cells appear (Fig. 2.1), i.e.,

$$\mathbf{A}\mathbf{p} = \begin{bmatrix} \mathbf{A}_{ii} & \mathbf{A}_{ie} & \mathbf{A}_{in} \\ \mathbf{A}_{ei} & \mathbf{A}_{ee} & \mathbf{A}_{en} \\ \mathbf{A}_{ni} & \mathbf{A}_{ne} & \mathbf{A}_{nn} \end{bmatrix} \begin{bmatrix} \mathbf{p}_i \\ \mathbf{p}_e \\ \mathbf{p}_n \end{bmatrix} = \begin{bmatrix} \mathbf{r}_i \\ \mathbf{r}_e \\ \mathbf{r}_n \end{bmatrix} = \mathbf{r}, \quad (2.8)$$

where the number of inner, edge, and node cells is N_i , N_e , and N_n , respectively.

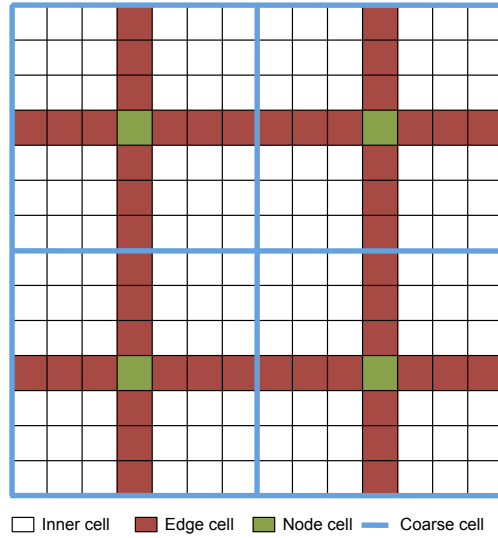


Figure 2.1: Primary and dual coarse grids for a two-dimensional cartesian fine-scale grid. The dual grid introduces a partition of the fine-grid cells into inner cells (belonging to a single dual cell), edge cells (shared by two dual cells) and node cells (shared by four dual cells).

General idea of the MsFV method is that the fine-scale pressure solution can be approximated by

$$\mathbf{p} = \mathbf{B}\mathbf{p}_n + \mathbf{C}\mathbf{r}, \quad (2.9)$$

where

$$\mathbf{B} = \begin{bmatrix} \mathbf{A}_{ii}^{-1}(\mathbf{A}_{ie}\mathbf{M}_{ee}^{-1}\mathbf{A}_{en} - \mathbf{A}_{in}) \\ -\mathbf{M}_{ee}^{-1}\mathbf{A}_{en} \\ \mathbf{I}_{nn} \end{bmatrix} \quad \text{and} \quad \mathbf{C} = \begin{bmatrix} \mathbf{A}_{ii}^{-1} & -\mathbf{A}_{ii}^{-1}\mathbf{A}_{ie}\mathbf{M}_{ee}^{-1} & \mathbf{0} \\ \mathbf{0} & \mathbf{M}_{ee}^{-1} & \mathbf{0} \\ \mathbf{0} & \mathbf{0} & \mathbf{0} \end{bmatrix} \quad (2.10)$$

are the basis-function operator (a $N \times N_n$ matrix), and the correction-function operator (a $N \times N$ matrix), respectively (note that for a five-point stencil discretization of the fine-scale problem we have $\mathbf{A}_{in} = \mathbf{A}_{ni} = \mathbf{0}$), and \mathbf{p}_n is the solution of the coarse problem (coarse node pressure). The N_n columns of \mathbf{B} contain the basis functions (interpolators) of the corresponding nodes; whereas the vector $\mathbf{C}\mathbf{r}$ describes the processes that do not scale with the node pressure. Intuitively speaking, $\mathbf{B}\mathbf{p}_n$ and $\mathbf{C}\mathbf{r}$ are analogous to a juxtaposition of (local) general and particular solutions of the problem, respectively.

Localization is realized by neglecting transversal fluxes across dual-cell boundaries. This is equivalent to eliminating the influence of inner cells on edge cells, thus defining the reduced-problem operator (a $N_e \times N_e$ matrix)

$$\mathbf{M}_{ee} = \mathbf{A}_{ee} + \text{diag} \left[\sum_i (\mathbf{A}_{ie}^T) \right], \quad (2.11)$$

where the operator $\text{diag}[\cdot]$ transforms a vector into a diagonal matrix. The coarse pressures,

\mathbf{p}_n , are obtained by solving

$$\mathbf{M}_{nn}\mathbf{p}_n = (\boldsymbol{\chi}\mathbf{A}\mathbf{B})\mathbf{p}_n = (\boldsymbol{\chi} - \boldsymbol{\chi}\mathbf{A}\mathbf{C})\mathbf{r}, \quad (2.12)$$

where $\mathbf{M}_{nn} = \boldsymbol{\chi}\mathbf{A}\mathbf{B}$ is the coarse operator (a $N_n \times N_n$ matrix) and $\boldsymbol{\chi}$ is the summation operator (a $N_n \times N$ matrix), which is the discrete analogous of a control volume integration and sums up all fine-cell values belonging to the same coarse cell.

With the definition of the restriction operator $\mathbf{R} = [\mathbf{0} \ \mathbf{0} \ \mathbf{I}_{nn}]$ (which extracts the node pressure from the pressure vector, i.e., $\mathbf{p}_n = \mathbf{R}\mathbf{p}$), the approximate pressure problem can be written in the form

$$\mathbf{M}\mathbf{p} = \mathbf{Q}\mathbf{r} \quad (2.13)$$

where $\mathbf{Q} = \mathbf{I} - \mathbf{R}^T\mathbf{R} + \mathbf{R}^T(\boldsymbol{\chi} - \boldsymbol{\chi}\mathbf{A}\mathbf{C})$ and

$$\mathbf{M} = \begin{bmatrix} \mathbf{A}_{ii} & \mathbf{A}_{ie} & \mathbf{A}_{in} \\ \mathbf{0} & \mathbf{M}_{ee} & \mathbf{A}_{en} \\ \mathbf{0} & \mathbf{0} & \mathbf{M}_{nn} \end{bmatrix} \quad (2.14)$$

is the MsFV operator, which has the inverse $\mathbf{M}^{-1} = \mathbf{B}\mathbf{M}_{nn}^{-1}\mathbf{R} + \mathbf{C}$. The approximate pressure solution $\mathbf{p} = \mathbf{M}^{-1}\mathbf{Q}\mathbf{r}$ is then used to assign Neumann boundary conditions for the calculation of the conservative velocity field. For a more detailed description of the operator formulation of the MsFV method we refer to [57].

2.6 Adaptive iterative MsFV method and transport

2.6.1 Iterative improvement of the local boundary conditions

The MsFV solution is an approximate solution and differs from the solution of the fine-scale problem due to the localization assumption, which neglects fluxes across dual-cell boundaries. In case of unstable flow, this differences are amplified with time and lead to different finger growth. Whereas in stable regions the MsFV pressure might be a good approximation, it is important to improve the accuracy of the solution in critical regions. This can be done by iteratively reducing the discrepancy with the reference solution.

Different strategies have been proposed to estimate the neglected transversal fluxes and improve the accuracy of the MsFV method [23, 58]. Following [58], we construct an iterative scheme that uses the pressure residual, $\mathbf{r} - \mathbf{A}\mathbf{p}$, to estimate the transversal fluxes and combines the MsFV operator with a Krylov subspace accelerator. The resulting algorithm is equivalent to the preconditioned Richardson equation

$$\mathbf{p}^{\nu+1} = \mathbf{p}^{\nu} + \omega^{\nu}\mathbf{M}^{-1}\mathbf{Q}(\mathbf{r} - \mathbf{A}\mathbf{p}^{\nu}), \quad (2.15)$$

where ν denotes the pressure iteration level [58], and the Generalized Minimal Residual method

(GMRES [67]) is used to compute the relaxation parameter ω^ν .

Since the coefficient matrix, \mathbf{A} , and the right hand side, \mathbf{r} , depend on the concentration, the pressure solution has to be recomputed every time that a new concentration solution is obtained, i.e., at the new time step or at the new iteration step to couple pressure and saturation. In order to reduce the number of iterations and keep the algorithm efficient, the initial pressure in Eq. (2.15), $\mathbf{p}^{\nu=0}$, is calculated using an estimate of the transversal fluxes that is based on the solution at the old time or pressure-saturation iteration step [24].

2.6.2 Adaptivity and transport

The iterative improvement of the local boundary conditions allows arbitrarily increasing the accuracy of the MsFV method, eventually converging to the exact solution of Eq. (2.6) [58]. Obviously, this comes at additional computational costs and it is important to introduce adaptive criteria to balance computational efficiency and accuracy. In addition to reusing previous estimates of the transversal fluxes (from previous time or pressure-saturation iteration steps) [24], computational costs can be adaptively reduced through two strategies: taking advantage of the fact that the pressure residual is non-zero only on edge cells (which is made possible by a preconditioner splitting [58]), and more important iteratively improving the boundary conditions only in critical subdomains. This naturally leads to a splitting of the domain into critical regions, where high accuracy is required, and noncritical regions, where an approximate solution is sufficient.

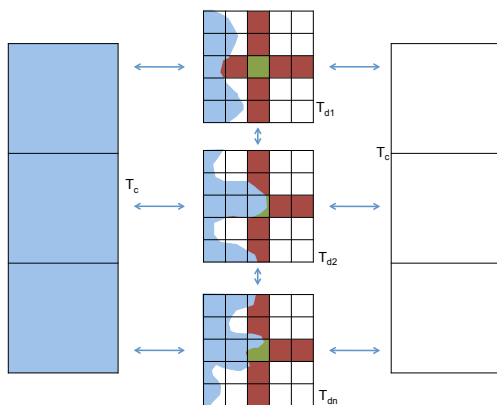


Figure 2.2: The front region is identified as the region characterized by large concentration gradient. In this region, the pressure solution is iteratively improved by reducing the pressure residual on edge cells, and a fine-scale velocity field is constructed to solve a fine-scale transport problem. In the rest of the domain, transport is solved on the coarse grid.

In case of density-driven instabilities, critical regions are those characterized by large concentration gradients (or front regions), where fingers are triggered and the fine-scale details of the flow are important. Regions where the concentration gradient is larger than a threshold value, δ , are identified as front regions. In these regions, the pressure errors are controlled by

iteratively reducing the residual on the edge cells. Then, an approximate, fully conservative fine-scale velocity field is constructed, and the transport equation is solved on the fine-scale grid (Fig. 2.2).

In regions of small concentration gradients, instead, small-scale details can be neglected [49], and the transport is solved on the coarse grid avoiding the construction of a fine-scale velocity field. The solution of the transport equation (coarsened outside the front region) can be written as

$$\mathbf{c} = \boldsymbol{\chi}_T^T (\boldsymbol{\chi}_T \mathbf{T} \boldsymbol{\chi}_T^T)^{-1} \boldsymbol{\chi}_T \mathbf{q}, \quad (2.16)$$

where the operator $\boldsymbol{\chi}_T$ sums up all fine-cell values belonging to the same coarse cell outside the front region, and leaves unchanged all values corresponding to the front region. Note that the same concentration value is assigned to fine cells outside the front region, which belong to the same coarse cell. Instead of solving Eq. (2.16) directly, we use a one level Schwarz decomposition technique [70],

$$\mathbf{c}^{\nu+1} = \mathbf{c}^\nu + \boldsymbol{\chi}_T^T \mathbf{T}_D^{-1} \boldsymbol{\chi}_T (\mathbf{q} - \mathbf{T} \mathbf{c}^\nu), \quad (2.17)$$

where

$$\mathbf{T}_D = \left[\begin{array}{ccc|c} \mathbf{T}_{d1} & \dots & \mathbf{0} & \mathbf{0} \\ \vdots & \ddots & \vdots & \vdots \\ \mathbf{0} & \dots & \mathbf{T}_{dn} & \mathbf{0} \\ \hline \mathbf{0} & \dots & \mathbf{0} & \mathbf{T}_{cc} \end{array} \right], \quad (2.18)$$

is a block diagonal matrix, whose blocks represent the transport problem outside the front region, \mathbf{T}_{cc} , and the local transport problems in each of the coarse cells of the front regions, $\mathbf{T}_{d1} \dots \mathbf{T}_{dn}$. To account for a moving front within a single time step, that may occur especially in case of large time steps, front and non-front coarse cells are defined at each pressure-saturation loop.

2.7 The iMsFV as downscaling method (DMsFV)

The adaptive iMsFV method presented in the previous sections is an upscaling-downscaling method devised to efficiently solve a problem that has been originally defined at the finest scale. The auxiliary coarse grids are used to decrease the computational costs associated with the solution of the original problem and the resulting solution is at most as accurate as the solution of the original problem. However, in many circumstances an accurate description of flow instabilities requires a refinement of the original problem rather than coarsening. These situation arises, for instance, because the original discretization is dictated by the medium heterogeneity rather than by the specific flow conditions, which might vary with time and lead to an unstable regime. In this context, we propose to modify the adaptive iMsFV method to be used as a downscaling method, thus as a method to obtain a more accurate solution than solving the original problem.

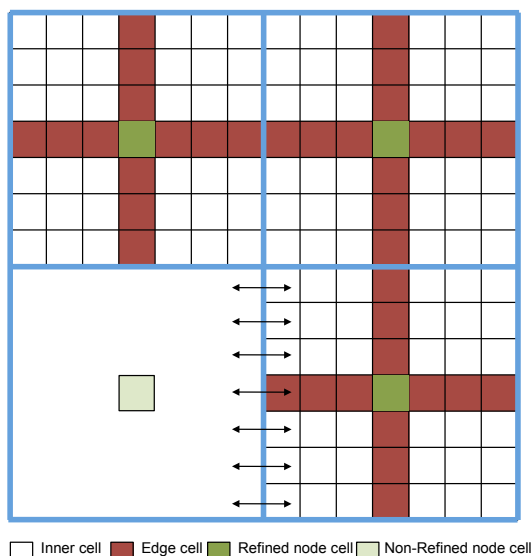


Figure 2.3: Extract of primary and dual coarse grids used for the downscaling algorithm. In the refined region the dual grid introduces a partition into inner, edge and refined node cells.

Let us consider again a pressure problem of the form of Eq. (2.6), which now represents the original, coarsest discretization level. Indicating by the subscript r the cells in the front region (i.e., the cells for which a mesh refinement is required) and by the subscript c the cells for which a coarse resolution is sufficient and the original discretization can be employed, we write the original problem as

$$\begin{bmatrix} \mathbf{A}_{rr} & \mathbf{A}_{rc} \\ \mathbf{A}_{cr} & \mathbf{A}_{cc} \end{bmatrix} \begin{bmatrix} \mathbf{p}_r \\ \mathbf{p}_c \end{bmatrix} = \begin{bmatrix} \mathbf{r}_r \\ \mathbf{r}_c \end{bmatrix}, \quad (2.19)$$

where the appropriate ordering has been employed, and the blocks $\mathbf{A}_{rc} = \mathbf{A}_{rc}^T$ represent the interaction between the refined and non-refined (coarse) regions.

The downscaled problem is defined using the original grid as coarse grid and constructing the corresponding dual grid in the refined region (see Fig. 2.3). In the non-refined region, coarse cells are node cells, whereas in the refined region they are partitioned into inner, edge and node fine-scale cells, and coarse fluxes are defined according to the downscaled mesh following the standard MsFV procedure. Fluxes between the refined and the non-refined regions are calculated from the original connectivities, and uniformly distributed among inner and edge cells at the common boundary; this avoids the problem of hanging nodes.

The resulting downscaling operator,

$$\mathbf{M}_D = \left[\begin{array}{cc|cc} \mathbf{A}_{ii} & \mathbf{A}_{ie} & \mathbf{A}_{ir} & \mathbf{A}_{ic} \\ \mathbf{0} & \mathbf{M}_{ee} & \mathbf{A}_{er} & \mathbf{A}_{ec} \\ \hline \mathbf{0} & \mathbf{0} & \mathbf{M}_{rr} & \mathbf{A}_{rc} \\ \mathbf{0} & \mathbf{0} & \mathbf{A}_{cr} & \mathbf{A}_{cc} \end{array} \right] \quad (2.20)$$

has the form of the MsFV operator, Eq. (2.14), with $\mathbf{A}_{in} = [\mathbf{A}_{ir} \ \mathbf{A}_{ic}]$, $\mathbf{A}_{en} = [\mathbf{A}_{er} \ \mathbf{A}_{ec}]$, and

$$\mathbf{M}_{nn} = \begin{bmatrix} \mathbf{M}_{rr} & \mathbf{A}_{rc} \\ \mathbf{A}_{cr} & \mathbf{A}_{cc} \end{bmatrix} = \chi \mathbf{A}_D \mathbf{B}. \quad (2.21)$$

The usual definitions apply to χ and \mathbf{B} , whereas

$$\mathbf{A}_D = \left[\begin{array}{cc|cc} \mathbf{A}_{ii} & \mathbf{A}_{ie} & \mathbf{A}_{ir} & \mathbf{A}_{ic} \\ \mathbf{A}_{ei} & \mathbf{A}_{ee} & \mathbf{A}_{er} & \mathbf{A}_{ec} \\ \hline \mathbf{0} & \mathbf{A}_{re} & \mathbf{A}_{rr}^* & \mathbf{0} \\ \mathbf{0} & \mathbf{0} & \mathbf{A}_{cr} & \mathbf{A}_{cc} \end{array} \right] \quad (2.22)$$

with $\mathbf{A}_{rr}^* = -\text{diag} \sum_e \mathbf{A}_{re}$ differs from \mathbf{A}_{rr} .

In accordance with the pressure equation, the transport problem in the non-refined region is solved on the original grid, whereas in the refined region it is solved on the downscaled grid. The two regions are matched by standard one-level Schwarz decomposition as described in Chapter 2.6.

2.8 Numerical simulations

As a test case, we first consider a two-dimensional version of the saltwater-freshwater fingering experiment [62, 39], and compare the MsFV solutions with a reference solution obtained by solving the problem on the fine-grid. We employ both the MsFV method without the iterative improvement of the local boundary conditions, and the adaptive iMsFV method with different front-detection thresholds. Subsequently, we use the downscaling iMsFV (DMsFV) method to investigate grid convergence of the convective Elder problem [73], which is a standard benchmark for density-driven saltwater intrusion with diffusive boundary conditions.

2.8.1 MsFV simulation of saltwater-freshwater instabilities

We consider a square computational domain of size $L = 2.025 \cdot 10^{-1}$ m, which is discretized into 162×162 cells of size $\Delta x = 1.25 \cdot 10^{-3}$ m. No-flow conditions are assigned at all four boundaries. The medium is characterized by a rectangular inclusion (width $W = 4.35 \cdot 10^{-2}$ m and height $H = L$) placed at the center of the domain and embedded in a less permeable material. The inclusion has permeability $k_1 = 10^{-9}$ m² and porosity $n_1 = 0.392$, whereas the embedding material has permeability $k_2 = 3.3 \cdot 10^{-10}$ m² and porosity $n_2 = 0.385$. Both diffusion and mechanical dispersion are modeled; and simulation parameters are summarized in Table 2.1. The resulting Rayleigh and dispersive Péclet numbers are $\text{Ra} = \frac{UL}{D_m} = \frac{k_1(\rho_{\max} - \rho_{\min})gL}{n_1 \mu_1 D_m} \approx 14500$ and $\text{Pe} = \frac{L}{\alpha_L} \approx 200$, respectively; whereas the grid Péclet number is $\text{Pe}_g = \frac{\Delta x}{\alpha_L} = 1.25$.

At initial conditions the denser saltwater ($c = 1$) is situated above a freshwater pool ($c = 0$) and the diffused interface between the two fluids is perturbed by one wave length in the inclusion

Table 2.1: Model parameters for the saltwater-freshwater fingering test-case (from [39]).

Parameter	Size	Unit	Parameter	Size	Unit
L	$2.025 \cdot 10^{-1}$	m	H	$2.025 \cdot 10^{-1}$	m
Δt	25	s	D_m	$1.0 \cdot 10^{-9}$	m^2/s
Δx	$1.25 \cdot 10^{-03}$	m	k_1	$1.0 \cdot 10^{-9}$	m^2
ΔX	$1.125 \cdot 10^{-02}$	m	k_2	$3.3 \cdot 10^{-10}$	m^2
$\rho(c=0)$	1000	kg/m^3	n_1	0.392	—
$\rho(c=1)$	1002.9	kg/m^3	n_2	0.385	—
$\mu(c=0)$	$1.0075 \cdot 10^{-3}$	kg/ms	α_l	$1.0 \cdot 10^{-03}$	m
$\mu(c=1)$	$1.002 \cdot 10^{-3}$	kg/ms	α_t	$1.0 \cdot 10^{-04}$	m
Ra	$1.45 \cdot 10^4$	—	Pe	$2 \cdot 10^2$	—

(Fig. 2.4 (a)). The initial conditions are adapted from [39]. The concentration distribution at four different times is shown in Fig. 2.4. Due to the density difference, the initial perturbation is amplified and two fingers develop in the highly permeable region, where saltwater flows downwards and freshwater upwards. At early time (Fig. 2.4 (b)) instabilities are present only in the inclusion; at later time (Fig. 2.4 (c)) weak secondary instabilities appear in the less permeable zone. After 15,000s saltwater accumulated at the bottom of the box and more accentuated secondary instabilities can be observed (Fig. 2.4 (d)). The simulation is repeated using the MsFV method with a 18×18 coarse grid, which corresponds to an upscaling factor of 9×9 and a coarse cell size $\Delta X = 1.125 \cdot 10^{-2}$ m. The concentration distributions at two different times is shown in Fig. 2.5, together with the difference between the MsFV solution and the fine-scale reference solution. It can be observed that the MsFV solution exhibits an earlier and more accentuated secondary instability.

2.8.2 Error sources in the MsFV method

To explain the more pronounced secondary instability, we analyze the effects of the MsFV method on the divergence and the curl of the velocity field. The condition on the divergence expresses mass conservation, Eq. (2.1), whereas the condition on the vorticity is equivalent to Darcy's law and can be obtained by applying the curl to Eq. (2.2). According to Helmholtz Theorem [3], a vector field is uniquely specified by its divergence and its curl; therefore, any approximate velocity field cannot satisfy both, mass conservation and the vorticity condition. In the MsFV method the velocity field computed from the approximate pressure has the correct vorticity, but does not conserve mass, whereas the conservative velocity field is characterized by an inexact vorticity.

To illustrate this with an example, we consider a quarter five-spot problem in a homogeneous medium without gravity effects, in which the exact velocity field is irrotational and solenoidal except at the injection and the production cells. The velocity field computed from the MsFV approximate pressure is irrotational but non-solenoidal on dual-cell boundaries; whereas the MsFV conservative velocity field is solenoidal, but non-irrotational on coarse-cell boundaries. Note that these errors are closely related: the vorticity error is the direct result of

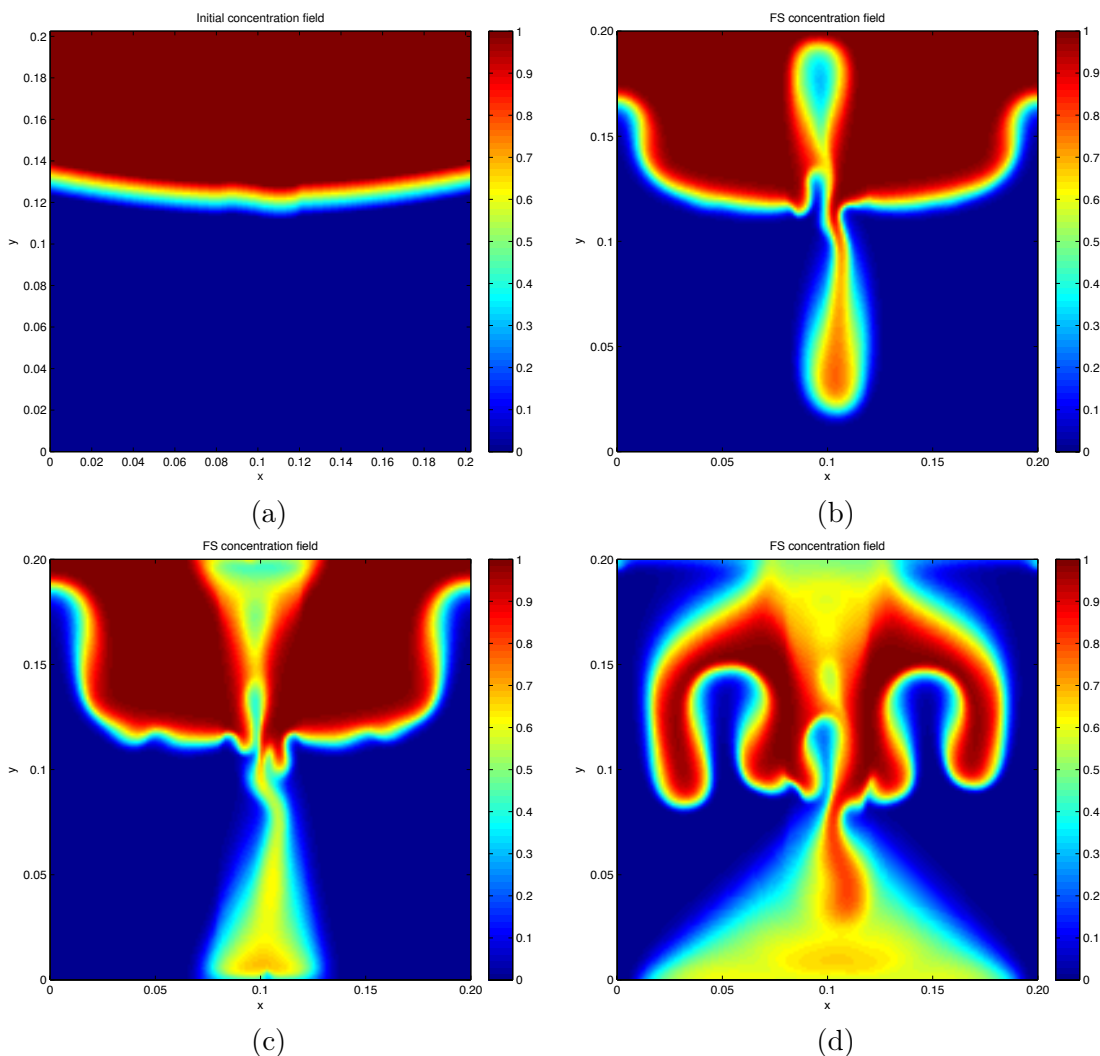


Figure 2.4: Fine-scale reference solution of the saltwater-freshwater instabilities. Shown is the normalized concentration c at four time steps: (a) $t = 0 \text{ s}$ (b) $t = 1.71 \text{ Ra } D/L^2 = 4750 \text{ s}$ (c) $t = 2.52 \text{ Ra } D/L^2 = 7150 \text{ s}$ (d) $t = 5.29 \text{ Ra } D/L^2 = 15000 \text{ s}$. Simulation parameters are summarized in Table 2.1.

the mass imbalance at the dual-cell boundaries and of the fact that the velocity is forced to be conservative.

In presence of gravity effects, the vorticity in a homogenous medium is

$$\nabla \times \mathbf{v} = \frac{\mathbf{k}}{\mu} (\nabla \rho \times \mathbf{g}), \quad (2.23)$$

which is nonzero where the density gradient is not parallel to the gravity acceleration. From Eq.(2.23) we observe that perturbing the vorticity is equivalent to perturbing the density gradient, which triggers instabilities. The inexact vorticity of the conservative velocity field can therefore be seen as a numerical perturbation of the interface that causes a more accentuated secondary instability.

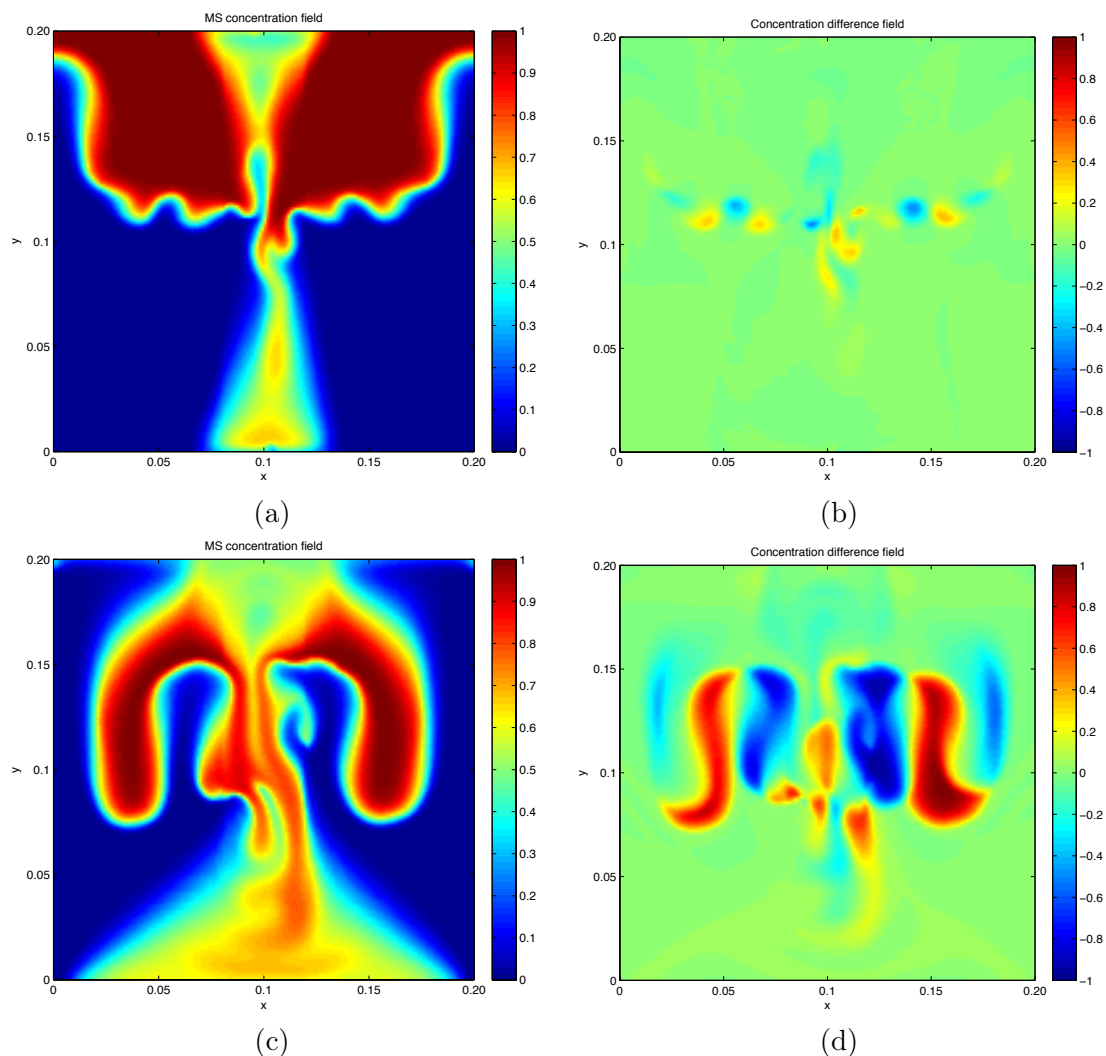


Figure 2.5: MsFV simulation of saltwater-freshwater instabilities: (a) MsFV concentration at time $t = 2.52 \text{ Ra } D/L^2 = 7150 \text{ s}$; (b) Difference between the MsFV solution and the fine-scale reference solution at time $t = 2.52 \text{ Ra } D/L^2 = 7150 \text{ s}$; (c) MsFV concentration at time $t = 5.29 \text{ Ra } D/L^2 = 15000 \text{ s}$; (d) Difference between the MsFV solution and the fine-scale reference solution at time $t = 5.29 \text{ Ra } D/L^2 = 15000 \text{ s}$.

2.8.3 Adaptive iMsFV simulations of saltwater-freshwater instabilities

The simulation of the saltwater-freshwater problem is repeated using the adaptive iMsFV method with three different front-detection thresholds, $\delta = 1 \text{ m}^{-1}$, 10 m^{-1} and 15 m^{-1} , which correspond to a concentration difference between coarse cells $\delta\Delta X = 0.01125$, 0.1125 and 0.1687 , respectively. In Fig. 2.6 the adaptive simulation results at time $t = 5.29 \text{ Ra } D/L^2 = 15000 \text{ s}$ are shown. It can be seen that $\delta = 10 \text{ m}^{-1}$, and more evidently $\delta = 15 \text{ m}^{-1}$ lead to a partly upscaled description of the transport problem, with a homogenized solution in some coarse cells.

By comparing the vertical profiles of the horizontally averaged concentration (Fig. 2.7 (a)),

we observe that for $\delta = 1 \text{ m}^{-1}$ the fine-scale solution and the adaptive iMsFV solution are mostly identical. In Fig.2.7 (b) the temporal evolution of the L2-error concentration norm for the three different thresholds is illustrated. It shows that concentration errors can be effectively controlled by small front-detection thresholds, and that the adaptive iMsFV is as accurate as the fine-scale solution if the threshold values are opportunely chosen. By comparing Fig.2.7 (a) and Fig.2.7 (b) it can also be seen that the criterion $\delta = 10 \text{ m}^{-1}$ in fact leads to local non-negligible errors, however the main fine-scale flow characteristics (in form of the averaged saturation profiles) can be satisfyingly reproduced.

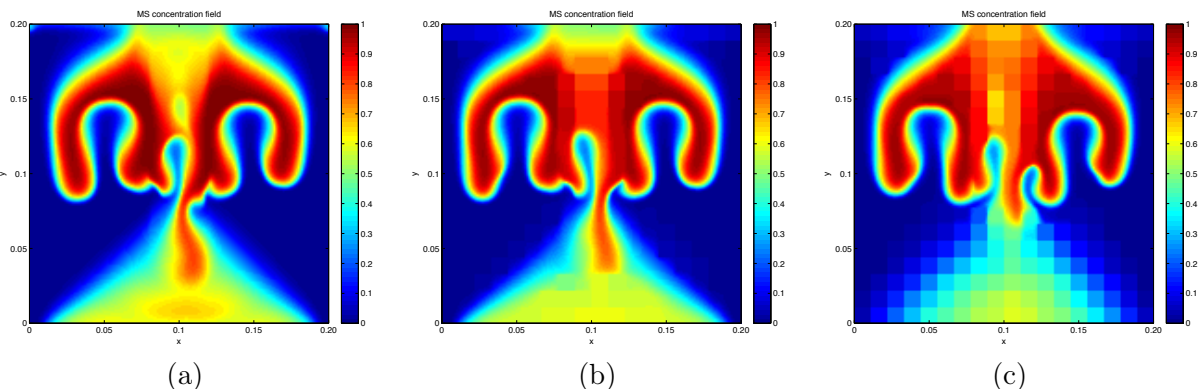


Figure 2.6: Adaptive iMsFV concentration profiles at $t = 5.29 \text{ Ra } D/L^2 = 15000 \text{ s}$ using a GMRES residual criterion of 10^{-6} : (a) $\delta = 1 \text{ m}^{-1}$. (b) $\delta = 10 \text{ m}^{-1}$. (c) $\delta = 15 \text{ m}^{-1}$.

The percentage of refined cells as a function of time is given in Fig.2.7 (c) and Fig.2.7 (d) shows the number of GMRES iterations per pressure solve as a function of time, which can be interpreted as a measure of the additional costs due to the iterative algorithm. Including the reuse of the solution at the old time step for the first calculation of the MsFV pressure, a total of about 2.4 GMRES iterations have been used. On the other hand, the adaptive criterion for front detection allows computing the fine scale-solution only in a portion of the computational domain. For the time simulated here, the average fraction of refined coarse cells is $f_R \approx 35 \%$, 48% and 61% for $\delta = 15 \text{ m}^{-1}$, 10 m^{-1} and 1 m^{-1} , respectively (Fig.2.7 (c)) (note that at later simulation times the number of refined coarse cells will decrease due to the accumulation of saltwater at the bottom). Fig.2.7 (c) and Fig.2.7 (d) show that the additional costs of the iterative improvement of the boundary conditions can be roughly balanced by the adaptive schemes. Indeed, for each time step, the cost of solving the flow problem and construct the conservative velocity can be quantified as $f_R \cdot (n_G + 1) \cdot n_c \cdot (a \cdot n_s^\alpha)$, where n_G is the number of GMRES solutions, n_c is the number of coarse problems, n_s is the size of the local problems and a and α are two solver related constants. For an average refinement $f_R = 40 \%$ and a number of GMRES iteration $n_G = 2.4$, the costs of the iterative algorithm is $1.36 \cdot n_c \cdot (a \cdot n_s^\alpha)$, which is about 1.36 times more expensive than the MsFV method (note that the restriction of the iterative improvement to edge cells additionally reduces the number of mathematical

operations per iteration step). With the good results of the adaptive MsFV code, we use the downscaling algorithm in the next subsection to perform grid convergence study of the Elder problem.

2.8.4 Grid convergence study of the Elder problem with the DMsFV method

The convective Elder problem is a classic benchmark for density-driven saltwater intrusion in porous media with diffusive boundary conditions. Previous works have shown that the solution strongly depends on the discretization level [13, 21] and to this point no unique reference solution exists for the problem. Here, we repeat grid convergence study of the Elder problem with the DMsFV method. In contrast to previous convergence studies, we present simulation results up to a grid of 147,968 cells for a TVD upwind scheme (this is comparable to grid level $l = 8$ in [13, 21], where the number of cells is calculated as $2^{2l+1} = 131,072$ cells).

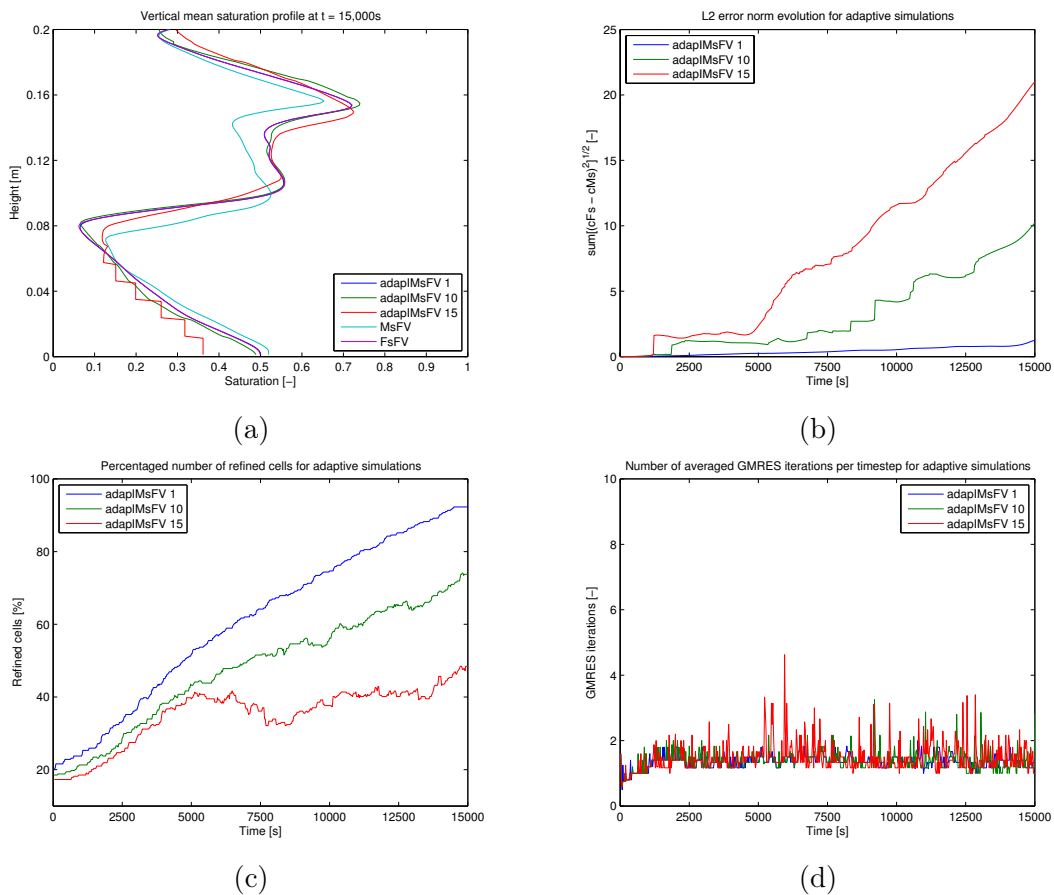


Figure 2.7: Adaptive iMsFV simulation results using a GMRES residual criterion of 10^{-6} . For adaptive simulations the front criteria δ is shown in the legend: (a) Vertical profile of the horizontally averaged concentration profiles; (b) L2-error concentration norm development for different front criteria. (c) Percentaged number of refined cells with respect to the coarse grid. (d) Per timestep averaged number of GMRES iteration.

Due to the symmetry of the problem, we consider only the left half domain of the original set-up (height $H = 150$ m, length $L = 300$ m, permeability $k = 4.845 \cdot 10^{-13} \text{ m}^2$), which is initially saturated with freshwater. At the upper left corner a Dirichlet boundary condition ($p_{Dir} = 0$ Pa) is applied, whereas all other boundaries are impermeable. Diffusive flux is allowed only at the bottom boundary, where a concentration $c = 0$ is assigned, and at the right half of the top boundary, where $c = 1$ is assigned. The parameters used for the simulation are summarized in Table 2.2, and they result in $\text{Ra} = \frac{k(\rho_{\max} - \rho_{\min})gH}{n\mu D_m} \approx 1400$.

We consider an initial discretization of 32×16 cells, which represents the coarsest grid and which is used for a standard 5-point stencil finite-volume discretization (level 1, 512 cells). Starting from this initial discretization, DMsFV simulations are performed with different downscaling factors: 3×3 (level 2, 4,608 cells); 9×9 (level 3, 41,608 cells); 15×15 (level 4, 115,200 cells) and 17×17 (level 5, 147,968 cells). The downscaling is applied adaptively based on the front-detection threshold $\delta = 10^{-3} \text{ m}^{-1}$, which corresponds to a maximum concentration difference between non-refined cells $\delta\Delta X \approx 0.01$; and 10^{-6} is used as convergence criterion for GMRES iterations. This small threshold value is chosen to ensure accurate results for the grid convergence study: the simulations of the saltwater-freshwater problem in the previous section have shown that comparable values lead to a perfect agreement with the reference solution. The simulations are conducted with a constant time step length $\Delta t = 5.376 \cdot 10^{-2} \text{ Ra}D_m/H^2 = 10$ d.

Table 2.2: Simulation parameters for the convective Elder problem (see, e.g., [13]).

Parameter	Size	Unit	Parameter	Size	Unit
L	300	m	D_m	$1.0 \cdot 10^{-6}$	m^2/s
H	150	m	k	$4.845 \cdot 10^{-13}$	m^2
ρ_{\min}	1000	kg/m^3	n	0.1	–
ρ_{\max}	1200	kg/m^3	μ_{\min}	$1.0 \cdot 10^{-3}$	$\text{kg}/\text{m}/\text{s}$
Δt	10	d	μ_{\max}	$1.0 \cdot 10^{-3}$	$\text{kg}/\text{m}/\text{s}$
Ra	1400	–	ΔX	9.375	m

In Fig. 2.8 the simulated 0.2, 0.4, 0.6 and 0.8 isolines at $t = 4.9 \frac{\text{Ra}D_m}{H^2} = 2.5 \text{ y}$, $9.8 \text{Ra}D_m/H^2 = 5 \text{ y}$; $19.6 \text{Ra}D_m/H^2 = 10 \text{ y}$ and $39.2 \text{Ra}D_m/H^2 = 20 \text{ y}$ are illustrated for the levels 1, 2, 3 and 5. Comparing the simulation results at the last time step, we can observe upwelling flow at the right boundary of the half domain for a 3×3 and 9×9 downscaling factor (level 2 and 3, respectively), whereas for a downscaling factor of 17×17 (level 5) and for the coarsest discretization (level 1) downwelling flow occurs in the same region (see also Fig. 2.9).

2.8.5 The effects of the advection schemes on the grid-convergence of the Elder problem

The reappearance of the downwelling flow at high discretization has also been observed in previous studies, in which however, the transition from upwelling to downwelling flow takes place at different discretizations, depending on the advective scheme used for the discretization

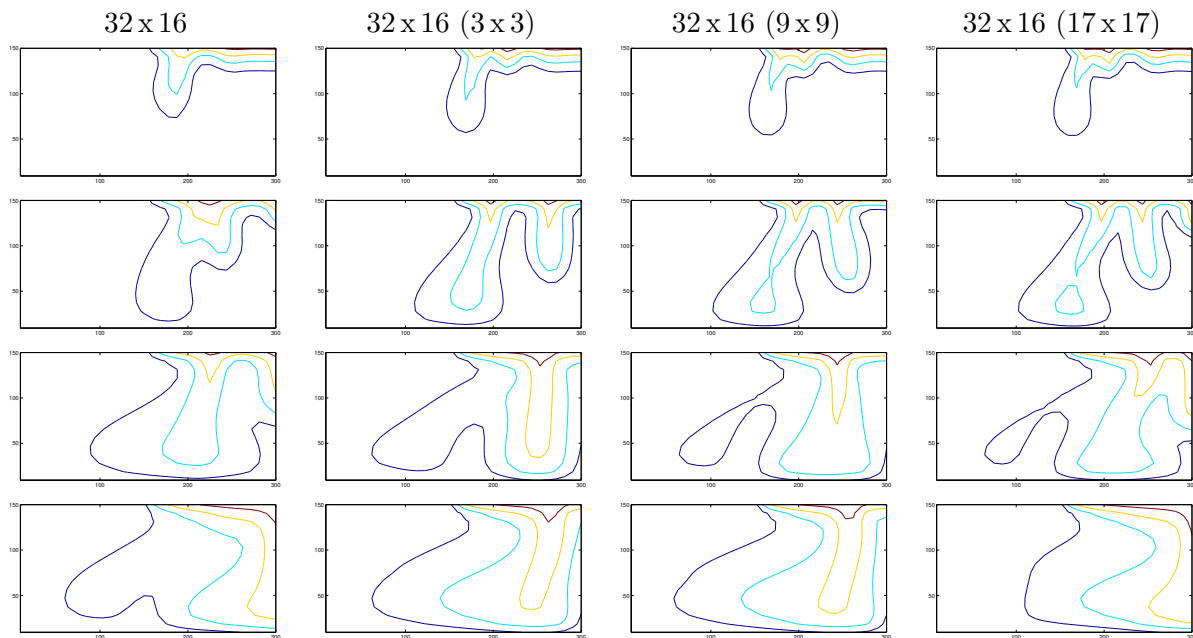


Figure 2.8: Interpolated salinities (isolines 0.2, 0.4, 0.6 and 0.8) at time $t = 4.9\text{Ra}D_m/H^2 = 2.5\text{ y}$, $9.8\text{Ra}D_m/H^2 = 5\text{ y}$; $19.6\text{Ra}D_m/H^2 = 10\text{ y}$ and $39.2\text{Ra}D_m/H^2 = 20\text{ y}$ for grid levels 1, 2, 3 and 5. Grid level 1 (512 cells) was solved by a standard finite-volume method. The other grid levels were computed with the help of the DMsFV method using a downscaling factor of 3×3 (4,608 cells), 9×9 (41,472 cells), 17×17 (147,968 cells), a time step length of $dt = 10\text{ d}$, a front criterion $\delta = 0.001\text{ m}^{-1}$ and a L2-error norm of 10^{-6} .

of the convective part. In [13], for instance, the use of a Galerkin-FEM method leads to a transformation to upwelling flow at a discretization $l = 6$ (8.192 cells); whereas in [21], using a partial upwind scheme, the reappearance of a downwelling flow for a discretization of $l = 7$ (32,768 cells) is shown. In the same work, the effect of a full upwind scheme on the simulation results is discussed. In this case a discretization $l = 7$ still leads to an upwelling flow, which is in agreement with the results of this work. To our knowledge, flow characteristics in case of full upwind schemes for discretizations finer than $l = 7$ have not been investigated to this point. With the DMsFV method we have shown that also with a TVD upwind scheme a back transition to downwelling flow takes place at higher discretizations. However, our results at level 5 (147,968 cells) are mostly identical to the simulation results at $l = 6$ in [13] and at $l = 7$ in [21], showing that downwelling flow reappears at a higher discretization than with the other methods.

To demonstrate that this difference is due to the choice of the advection scheme, we repeat DMsFV simulations with a 9×9 downscaling factor (level 3) using a first-order upwind, a second-order centered and a second-order QUICK scheme. The simulation results at $t = 39.2\text{Ra}D_m/H^2 = 20\text{ y}$ are shown in Fig.2.10. With the Flux Limiter, Upwind and Quick scheme identical results are obtained, verifying (in addition to the calculation of the grid

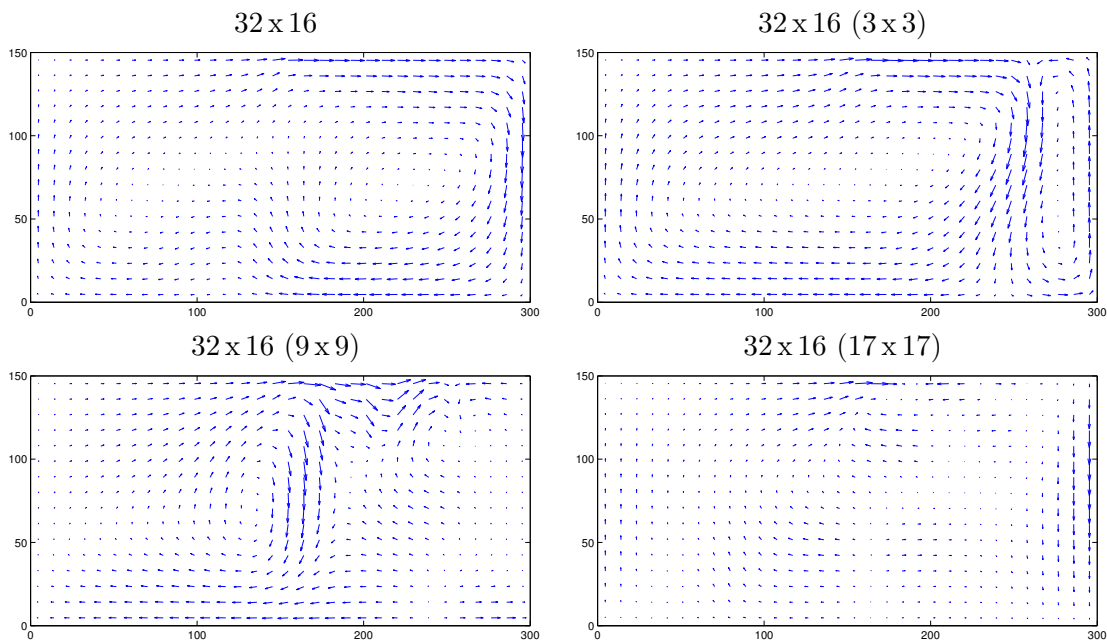


Figure 2.9: Simulated upscaled velocities at time $t = 39.2\text{Ra}D_m/H^2 = 20y$ for grid levels 1, 2, 3 and 5, using a time step length of $dt = 10d$, a front criterion $\delta = 0.001\text{m}^{-1}$ and a L2-error norm of 10^{-6} .

Péclet number) that the later transformation to a downwelling flow is not based on numerical smoothing of the front. With a centered scheme we reproduce the results of previous studies [13, 21], which confirms that the solution of the DMsFV simulations are in agreement with fine-scale simulations employing the same numerical scheme.

2.9 Conclusions

In contrast to the case of stable flow, the MsFV methods does not provide satisfactory results for unstable conditions. Due to instability, small errors grow with time leading to different flow patterns and finger growth. In particular, we have observed that the MsFV solutions are characterized by a more pronounced instability leading to a larger number of fingers. This is due to the perturbation of the vorticity field introduced by the construction of the conservative velocity. As a consequence of the Helmholtz theorem and the uniqueness of a vector field defined by divergence and vorticity, enforcing mass balance (hence the exact divergence) perturbs the vorticity field, which is equivalent to perturbing the interface, and triggers unphysical fingers.

Accurate simulations of density-driven instability require controlling the MsFV errors, which can be done by iteratively improving the boundary conditions used to define the local problems and construct basis and correction functions. Very accurate solutions can be obtained by using the pressure residual to estimate the transversal fluxes at the dual-cell boundaries and combining the MsFV operator with a Krylov subspace method (in particular, we use GMRES).

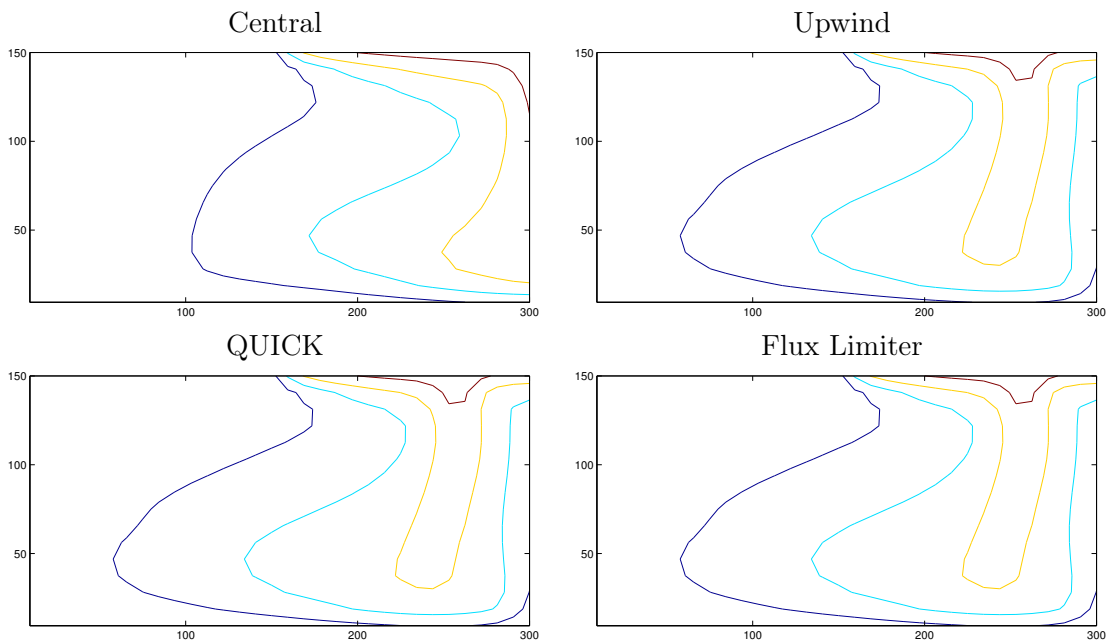


Figure 2.10: Interpolated salinities (isolines 0.2, 0.4, 0.6 and 0.8) at time $t = 39.2\text{Ra}D_m/H^2 = 20\text{y}$ using different convective schemes for the solution of the transport equation for refinement level 3, which corresponds to a 9×9 downscaling factor (41,472 cells).

To avoid large computational overhead due to the iterative scheme, we have suggested several adaptive strategies, which can be used to balance accuracy and computational efficiency. In order to limit the computational overload due to the iterations, we reuse previous estimates of the transversal fluxes (either from previous time steps or previous coupling iterations) [24] and reduce the portion of the domain in which iterations are employed. An adaptive criterion is used to identify the front region, where instabilities are triggered and an iteratively improved solution is required. The transport is also solved adaptively, using the same partitioning of the domain introduced by the adaptive iMsFV algorithm and calculating a fine-scale solution only within the front region; this avoids the construction of a conservative velocity field outside the front region and reduces the size of the transport problem. We have shown that this adaptive strategy can compensate the computational overload introduced by the iterative scheme, leading to much more accurate solution for roughly the same computational cost.

This adaptive iMsFV clearly defines the front-region, in which fine-scale details are resolved, and the rest of the domain where the problem is upscaled and only a coarse description is given both for flow and transport. In many problems dealing with instability, however, an accurate description of finger triggering and growth requires a refinement of the computational grid rather than a coarsening. At this end, we have modified the adaptive iMsFV algorithm to be used as a grid refinement technique to improve accuracy rather than a technique to achieve computational efficiency. In this framework, the DMsFV method avoids too many iterations through the possibility of constructing a conservative velocity from an approximate

pressure solution and keeps the method efficient also for large refined regions. Whereas the computational costs of standard grid refinement techniques (e.g., quad- or octree) tend to the cost of solving the problem on a fine grid if the refined region is large, the cost of the DMsFV remains comparable to the cost of the MsFV method. Moreover, the DMsFV clearly separates the computational domain into refined and non-refined regions, which can be treated separately and matched later. This gives great flexibility to employ different physical descriptions in different regions, where different equations can be solved, offering an excellent framework to construct hybrid methods that couple, for instance, a Darcy and Stokes description of the flow.

Acknowledgments

This project is supported by the Swiss National Science Foundation grant number no. FNS PP00P2_123419/1.

Chapter 3

A Multilevel Multiscale Finite-Volume method

Rouven Künze, Ivan Lunati, and Seong H. Lee

published in *Journal of Computational Physics*¹

¹R. Künze, I. Lunati, and S.H. Lee. A Multilevel Multiscale Finite-Volume method, *Journal of Computational Physics*, 255:502-520, 2013.

3.1 Abstract

The Multiscale Finite-Volume (MsFV) method has been developed over the last decade to efficiently solve large reservoir models. The method projects the original pressure problem onto a second coarser grid, on which it is less expensive to solve, and then prolongates the approximated coarse solution back to the fine-scale grid. One characteristic of the MsFV algorithm is to allow the reconstruction of an approximate but fully conservative velocity field from the prolonged pressure. This makes the method particularly attractive for applications involving the solution of transport problems. Here, we present an extension of the MsFV method (MMsFV) that can employ multiple levels of coarsening instead of the single coarse level used in the standard algorithm. Whereas the coarse problem and the prolongation operators can be easily obtained by recursive application of the MsFV method, formulating an efficient reconstruction of the conservative velocity is not trivial. We devise a nested reconstruction procedure that is novel and has computational cost comparable with the MsFV reconstruction. By analyzing the computational complexity of the algorithm we show that the MMsFV method allows obtaining a conservative approximation of the fine-scale velocity more efficiently than the MsFV method. However, the accuracy of the solution deteriorates and MMsFV errors are larger than MsFV errors. By means of numerical test cases we demonstrate that, when the MMsFV operator is used as preconditioner in GMRES, the number of iterations necessary to achieve the same accuracy is larger than with the MsFV operator. For highly-heterogeneous permeability fields more than several hundreds of iterations might be required. Such a large number of iterations might be practically intractable. Therefore, we propose two ideas that can be used to control the number of iterations. The first is to combine the MMsFV coarse operator with an appropriate smoother in a two-step preconditioner; the second is to modify the localization assumptions used to solve edge problems. Our numerical tests show that both strategies lead to a significant reduction of the iterations and suggest that efficient MMsFV methods can be obtained by identifying optimal smoothers or devising better localizations for the edge problems.

3.2 Introduction

In field-scale simulations, very large models (several millions to billions of cells) are often employed to describe realistic geological structures and complex physical processes in a reservoir. Despite the steady increase of computer power, efficient algorithms are required to numerically solve these large problems. At this end, several multiscale methods (e.g., [1, 8, 34, 42, 60]) have been developed that employ, in addition to the original level of discretization (fine grid), an auxiliary coarser discretization level (coarse grid), which is used to calculate an approximate solution of the fine-scale problem. These methods first upscale the fine-scale problem to the coarse grid (restriction), and then interpolate the coarse solution back to the fine grid (prolongation).

The Multiscale Finite-Volume (MsFV) method (see, e.g., [36, 57, 58]) belongs to this class of techniques, but typically employs an additional dual coarse grid to define the local problems that are used to construct the prolongation operators. A set of coarse-cell balance equations is then obtained by integrating the fine-scale problem over the coarse cells. This characteristic allows constructing an approximate but conservative flux field by solving a set of local problems on coarse cells with boundary conditions obtained from the prolonged solution. Conservation is automatically guaranteed by the consistency between the boundary conditions and the coarse-scale fluxes. For difficult problems (e.g., large grid aspect ratios, highly anisotropic and heterogeneous permeability fields) the localization assumption used to construct the prolongation operator might become less accurate. In this case the quality of MsFV solution deteriorates and the reconstructed conservative velocity field exhibits a disturbed vorticity [45, 55]. To overcome this issue, several iterative strategies have been proposed to improve the quality of the solution while allowing the construction of a fine-scale conservative flux field at every iteration step [23, 58, 76].

The MsFV method has proven accurate and efficient for problems with approximately 1,000,000 unknowns [36]. However, for very large problems (several millions to billions of unknowns) that are often encountered in oil field simulations, solving the MsFV coarse problem can remain a serious computational bottleneck. In this paper we propose an extension of the MsFV method to multiple levels of coarsening, which allows keeping the algorithm efficient also for large problem. Even though it is quite straightforward to obtain prolongation and restriction operators for this novel Multilevel MsFV (MMsFV) method by recursive applications of the standard MsFV procedure, an efficient reconstruction step needs to be devised to obtain a conservative fine-scale velocity field. The main challenge is to avoid the solution of fine-scale problems defined on the cells of the coarsest level of discretization, which would be computationally too expensive in a multilevel method. In this paper we propose a nested reconstruction procedure for the velocity that only involves local problems defined on the less coarse discretization level.

The paper is organized as follows. In Chapter 3.3, we briefly introduce the equations governing two-phase flow in the subsurface. In Chapter 3.4, we extend the MsFV method to employ multiple levels of coarsening and we devise a nested reconstruction procedure that allows an efficient calculation of the fine-scale conservative flux field for the MMsFV algorithm. In Chapter 3.5, we discuss the iterative extension of MsFV and MMsFV. In Chapter 3.6 we perform a novel and detailed complexity analysis that enables: highlighting the computational bottleneck in the traditional MsFV method; demonstrating that the relative cost of the nested reconstruction of the MMsFV method is small; and discussing the speed-up that can be obtained by the iMMsFV algorithm. In Chapter 3.7 the multilevel and multiscale pressure solutions are compared by two- and three-dimensional numerical test cases. Finally, conclusions follow in Chapter 3.8.

3.3 Governing equations

For immiscible, incompressible two-phase flow, the mass conservation equation for each phase is given by

$$\phi \frac{\partial}{\partial t} S_\gamma + \nabla \cdot \mathbf{u}_\gamma = -q_\gamma, \quad \gamma = 1, 2, \quad (3.1)$$

where γ is the phase index, S_γ [-] is the phase saturation; ϕ [-] the porosity; and q_γ [1/s] the source term. It is assumed that the phase velocity is governed by the generalized Darcy's law (see, e.g., [31])

$$\mathbf{u}_\gamma = -\boldsymbol{\lambda}_\gamma \nabla p_\gamma \quad \gamma = 1, 2, \quad (3.2)$$

where p_γ [Pa] is the phase pressure, $\boldsymbol{\lambda}_\gamma = k_{r\gamma} \mathbf{k} / \mu_\gamma$ [m²/Pa·s] the mobility of the phase γ ; μ_γ [Pa·s] the viscosity; \mathbf{k} [m²] and $k_{r\gamma}$ [-] the absolute permeability tensor (which is assumed diagonal) and the relative permeability, respectively.

For simplicity of presentation, we neglect capillary effects and drop the phase indices of the pressures ($p_1 = p_2 = p$). With a constitutive relationship for the relative permeabilities, $k_{r\gamma} = k_{r\gamma}(S_\gamma)$, and the saturation constraint $S_1 + S_2 = 1$, we have a complete system of equations for the unknown variables, p , S_1 and S_2 .

In this work, we employ a pressure-saturation formulation to solve this system of equations. Summing up the two mass-balance equations, Eq. (3.1), we obtain the pressure equation,

$$\nabla \cdot (\boldsymbol{\lambda}_{tot} \nabla p) = q_{tot}, \quad (3.3)$$

where $\boldsymbol{\lambda}_{tot} = \boldsymbol{\lambda}_1 + \boldsymbol{\lambda}_2$ is the total mobility tensor and $q_{tot} = q_1 + q_2$ the total source term. Once the pressure is computed, the saturation is obtained by solving the mass-balance equation for one of the two phases (e.g., phase 1),

$$\phi \frac{\partial}{\partial t} S_1 + \nabla \cdot [f_1(S_1) \mathbf{u}_{tot}] = -q_1, \quad (3.4)$$

where the total velocity is defined as

$$\mathbf{u}_{tot} = \mathbf{u}_1 + \mathbf{u}_2 = -\boldsymbol{\lambda}_{tot} \nabla p, \quad (3.5)$$

and the fractional flow function is given by

$$f_1 = \frac{\frac{k_{r1}}{\mu_1}}{\frac{k_{r1}}{\mu_1} + \frac{k_{r2}}{\mu_2}}. \quad (3.6)$$

Eqs. (3.3) and (3.4) are solved by a sequentially implicit scheme [37].

3.4 The Multilevel MsFV (MMsFV) method

The MsFV method was originally developed to efficiently solve the elliptic pressure equation [36]. Even though multiscale extensions have been proposed for the transport equation (e.g., [45, 49]) and additional levels of coarsening would also be applicable to the solution of the transport problem, in this paper we focus on the application of the multilevel concept to the pressure equation, Eq. (3.3).

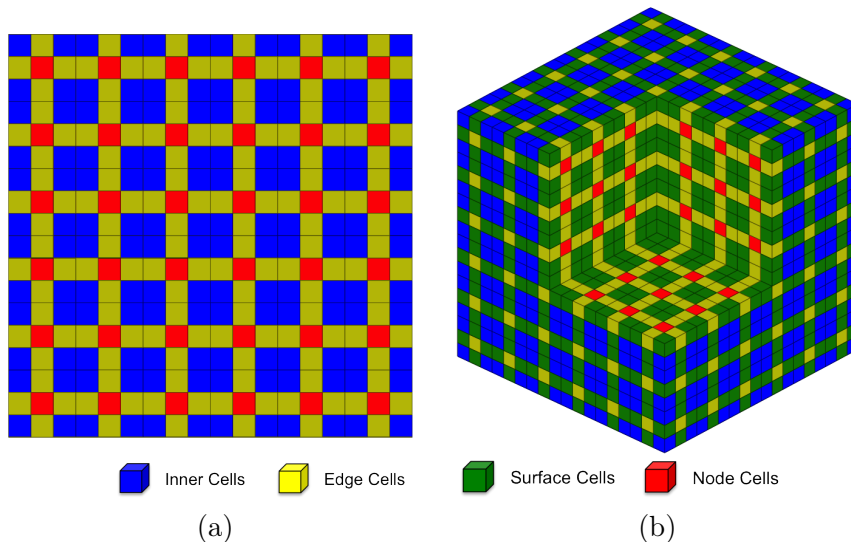


Figure 3.1: (a) Two-dimensional fine-scale grid with dual coarse grid indicating the partition of fine-scale cells into inner (i); edge (e) and node (n) cells. (b) For three-dimensional problems, the fine-cell partition consists of inner (i); surface (s); edge (e) and node (n) cells.

The discrete form of the pressure equation can be written as

$$\mathbf{A}\mathbf{p} = \mathbf{r}, \quad (3.7)$$

where \mathbf{A} is the stiffness matrix, \mathbf{p} the unknown pressure vector, and \mathbf{r} the right hand side vector, which contains terms from sources, sinks, and boundary conditions. In the derivation of MMsFV, we closely follow the operator-based formulation of the MsFV method [57], but we consider more general stencils based on a 9-point and 27-point flux approximation in 2D and 3D, respectively.

3.4.1 MsFV pressure

In addition to the original fine-scale grid (level-0), the MsFV method employs an auxiliary coarse grid (level-1), together with its dual (coarse) grid (see Fig. 3.1). It is assumed that the pressure solution can be approximated as

$$\mathbf{p} \approx \mathbf{p}_{Ms} = \mathbf{B}\mathbf{p}_n + \mathbf{C}\mathbf{r}, \quad (3.8)$$

where \mathbf{B} is the basis-function operator, which contains the solution of the localized dual grid problems; and \mathbf{C} is the correction-function operator, which accounts for the local effects of the right hand side [53, 56, 57] (the explicit form of \mathbf{B} and \mathbf{C} is given in App. 3.9.1).

In Eq. (3.8), \mathbf{p}_n is the coarse (node) pressure vector, which is obtained by solving the coarse problem

$$\mathbf{M}_{nn}\mathbf{p}_n = (\chi\mathbf{A}\mathbf{B})\mathbf{p}_n = \chi(\mathbf{I} - \mathbf{A}\mathbf{C})\mathbf{r}. \quad (3.9)$$

Here, we have introduced the control-volume summation operator χ , that sums up all fine-scale values corresponding to the same coarse cell; the coarse-scale MsFV operator $\mathbf{M}_{nn} = (\chi\mathbf{A}\mathbf{B})$; and the identity matrix \mathbf{I} .

Substituting Eq. (3.9) into Eq. (3.8), we readily write the MsFV pressure solution in the form

$$\mathbf{p}_{Ms} = \mathbf{A}_{Ms}^{-1}\mathbf{r}, \quad (3.10)$$

where the inverse of the fine-scale operator is approximated as

$$\mathbf{A}^{-1} \approx \mathbf{A}_{Ms}^{-1} = \mathbf{B}(\chi\mathbf{A}\mathbf{B})^{-1}\chi(\mathbf{I} - \mathbf{A}\mathbf{C}) + \mathbf{C}. \quad (3.11)$$

3.4.2 Multilevel MsFV pressure

In case of very large problem, the MsFV solution might still require a considerable computational effort: for small coarsening factors, the coarse problem will be the computational bottleneck, whereas for large upscaling factors the computational efficiency will be limited by the construction of the operators \mathbf{B} and \mathbf{C} (the computational cost of MsFV is discussed in detail in Chapter 3.6).

To improve numerical efficiency for problems with a large coarse grid (problems with a very large number of cells or with a small upscaling factor), the MsFV concept can be reapplied to the coarse problem. For the sake of clarity, we first present the method for two-coarse-level MsFV (MMsFV) method: in addition to the fine grid (level-0) and the first coarse grid (level-1), a second, coarser grid is employed together with its coarse dual (level-2).

By introducing a subscript indicating the coarsening level to which operators refer, the MsFV approximation of \mathbf{A}^{-1} can be written as

$$\mathbf{A}^{-1} \approx \mathbf{A}_{Ms}^{-1} = \mathbf{B}_1\mathbf{M}_{nn,1}^{-1}\chi_1(\mathbf{I} - \mathbf{A}\mathbf{C}_1) + \mathbf{C}_1. \quad (3.12)$$

The level-1 inverse coarse operator, $\mathbf{M}_{nn,1}^{-1} = (\chi_1\mathbf{A}\mathbf{B}_1)^{-1}$, is approximated as

$$\mathbf{M}_{nn,1}^{-1} \approx \mathbf{B}_2\mathbf{M}_{nn,2}^{-1}\chi_2(\mathbf{I} - \mathbf{M}_{nn,1}\mathbf{C}_2) + \mathbf{C}_2, \quad (3.13)$$

where $\mathbf{M}_{nn,2} = (\chi_2\mathbf{M}_{nn,1}\mathbf{B}_2)$ is the level-2 coarse operator and \mathbf{B}_2 and \mathbf{C}_2 are the level-2 prolongation- and correction function-operators. The explicit form of \mathbf{B}_2 and \mathbf{C}_2 can again be obtained from Eq. (3.45) and Eq. (3.46) in App. 3.9.1, which give the explicit form of \mathbf{B} and \mathbf{C} for a 3D (resp. 2D) problem with a 27-point (resp. 9-point) discretization at the lower grid

level (there, \mathbf{A} should be replaced by $\mathbf{M}_{nn,1}$, and \mathbf{M}_{ee} , \mathbf{M}_{ss} , and $\mathbf{M}_{nn,2}$ by $\mathbf{M}_{ee,2}$, $\mathbf{M}_{ss,2}$, and \mathbf{M}_{nn} , respectively).

Finally, by substituting Eq. (3.13) into Eq. (3.12), we obtain the two-coarse-level approximation,

$$\mathbf{A}^{-1} \approx \mathbf{A}_{\text{MMs}}^{-1} = \mathbf{B}_1 \mathbf{B}_2 (\chi_2 \chi_1 \mathbf{A} \mathbf{B}_1 \mathbf{B}_2)^{-1} \chi_2 \chi_1 (\mathbf{I} - \mathbf{A} \mathbf{B}_1 \mathbf{C}_2 \chi_1) (\mathbf{I} - \mathbf{A} \mathbf{C}_1) + \mathbf{B}_1 \mathbf{C}_2 \chi_1 (\mathbf{I} - \mathbf{A} \mathbf{C}_1) + \mathbf{C}_1, \quad (3.14)$$

which can be written of the form

$$\mathbf{A}^{-1} \approx \mathbf{A}_{\text{MMs}}^{-1} = \mathbf{G} (\mathbf{I} - \mathbf{A} \mathbf{S}) + \mathbf{S} = \mathbf{G} + \mathbf{S} - \mathbf{G} \mathbf{A} \mathbf{S}, \quad (3.15)$$

where

$$\mathbf{G} = \mathbf{B}_1 \mathbf{B}_2 (\chi_2 \chi_1 \mathbf{A} \mathbf{B}_1 \mathbf{B}_2)^{-1} \chi_2 \chi_1, \quad (3.16)$$

and

$$\mathbf{S} = \mathbf{B}_1 \mathbf{C}_2 \chi_1 (\mathbf{I} - \mathbf{A} \mathbf{C}_1) + \mathbf{C}_1. \quad (3.17)$$

By recursively applying the procedure above, we can derive the general n -level approximation

$$\mathbf{A}^{-1} \approx \mathbf{A}_{\text{MMs}}^{-1} = \mathbf{G}_n (\mathbf{I} - \mathbf{A} \mathbf{S}_n) + \mathbf{S}_n \quad (3.18)$$

where

$$\mathbf{G}_n = \left(\prod_{i=1}^n \mathbf{B}_i \right) \left[\left(\prod_{i=1}^n \chi_{n+1-i} \right) \mathbf{A} \left(\prod_{i=1}^n \mathbf{B}_i \right) \right]^{-1} \left(\prod_{i=1}^n \chi_{n+1-i} \right) \quad (3.19)$$

and

$$\mathbf{S}_n = \sum_{i=1}^n \left[\left(\prod_{j=1}^{i-1} \mathbf{B}_j \right) \mathbf{C}_i \left(\prod_{j=1}^{i-1} \chi_{i-j} \right) \left(\mathbf{I} - \mathbf{A} \left(\prod_{j=1}^{i-2} \mathbf{B}_j \right) \mathbf{C}_{i-1} \left(\prod_{j=1}^{i-2} \chi_{i-j} \right) \right) \right], \quad (3.20)$$

and where we have $\mathbf{C}_0 = \mathbf{0}$, $\mathbf{B}_0 = \chi_0 = \mathbf{I}$. Notice that for $n = 1$ we have $\mathbf{G}_1 = \mathbf{B}_1 (\chi_1 \mathbf{A} \mathbf{B}_1)^{-1} \chi_1$ and $\mathbf{S}_1 = \mathbf{C}_1$, and we recover the standard MsFV method in Eq. (3.11).

3.4.3 Conservative fine-scale fluxes

Darcy fluxes computed from the approximate MsFV pressure vector are non-conservative due to the localization assumption and would yield severe mass balance errors at the dual-cell boundaries if they are used to solve a transport problem [36]. However, the coarse grid velocity is conservative, i.e., $\chi(\mathbf{r} - \mathbf{A} \mathbf{p}_{\text{Ms}}) = \mathbf{0}$, because $\chi \mathbf{A} \mathbf{A}_{\text{Ms}}^{-1} = \chi$ and a conservative velocity field inside coarse-cells can be easily constructed from the solution of Eq. (3.10) [52]. This is done by solving a set of local problems on coarse-cells with Neumann boundary conditions computed from the MsFV pressure solution in Eq. (3.10), i.e.,

$$\mathbf{D} \mathbf{p}_c = \mathbf{r} - (\mathbf{A} - \mathbf{D}) \mathbf{p}_{\text{Ms}}, \quad (3.21)$$

where the operator \mathbf{D} is obtained by neglecting the connection between fine-cells belonging to different coarse-cells in the original stiffness matrix \mathbf{A} . \mathbf{D} is block diagonal if the pressure vector is reordered with respect to the coarse grid, and $(\mathbf{A} - \mathbf{D})\mathbf{p}_{\text{Ms}}$ are the Neumann fluxes between the coarse interfaces [57, 58].

This reconstructed velocity honours mass conservation to the degree permitted by the solver employed to solve the local and the coarse problems. Therefore, mass is conserved to machine precision only if a direct solver is used or if full convergence is achieved by an iterative solver. However, assuming that a direct solver is used for the small local problems, the size of the problem for which the desired tolerance must be achieved is reduced.

The two-coarse-level approximation of the stiffness matrix, in contrast, yields level-1 coarse velocities that are not conservative, $\chi_1 \mathbf{A} \mathbf{A}_{\text{MMs}}^{-1} \neq \chi_1$, but honours the level-2 mass constraint

$$\chi_2 \chi_1 \mathbf{A} \mathbf{A}_{\text{MMs}}^{-1} = \chi_2 \chi_1 \mathbf{A} \mathbf{B}_1 \mathbf{B}_2 (\chi_2 \chi_1 \mathbf{A} \mathbf{B}_1 \mathbf{B}_2)^{-1} \chi_2 \chi_1 (\mathbf{I} - \mathbf{A} \mathbf{S}) + \chi_2 \chi_1 \mathbf{A} \mathbf{S} = \chi_2 \chi_1. \quad (3.22)$$

Therefore constructing a conservative velocity field would require solving a set of local problems that are defined on the cells of the level-2 coarse grid, i.e.,

$$\mathbf{D}_2 \mathbf{p}_{c,0} = \mathbf{r} - (\mathbf{A} - \mathbf{D}_2) \mathbf{p}_{\text{MMs}}, \quad (3.23)$$

where \mathbf{D}_2 is analogous to \mathbf{D} in Eq. (3.21) and $(\mathbf{A} - \mathbf{D}_2) \mathbf{p}_{\text{MMs}}$ are the fine-scale Neumann fluxes over level-2 coarse grid boundaries. Henceforth, the subscript i to the vector $\mathbf{p}_{c,i}$ denotes the level on which the resulting velocity is conservative (i.e., 0 on the fine-grid, 1 on level-1 coarse grid, and 2 on level-2 coarse grid).

Even for small upscaling factors, the total cost of the local problems in Eq. (3.23) can be computationally more expensive than the coarse problem and will become prohibitive in case of several coarse levels. Therefore, a nested reconstruction has to be devised to guarantee that only problems on small supports are solved. We approximate the inverse of \mathbf{D}_2 by applying the MsFV method in each cell of the level-2 coarse grid. An approximate solution of Eq. (3.23) can be obtained by approximating \mathbf{D}_2^{-1} as

$$\mathbf{D}_2^{-1} \approx \mathbf{D}_{2,\text{Ms}}^{-1} = \mathbf{B}_d (\chi_1 \mathbf{D}_2 \mathbf{B}_d)^{-1} \chi_1 (\mathbf{I} - \mathbf{D}_2 \mathbf{C}_d) + \mathbf{C}_d, \quad (3.24)$$

which yields the pressure

$$\mathbf{p}_{c,1} = \mathbf{D}_{2,\text{Ms}}^{-1} [\mathbf{r} - (\mathbf{A} - \mathbf{D}_2) \mathbf{p}_{\text{MMs}}] = \mathbf{D}_{2,\text{Ms}}^{-1} [\mathbf{I} - (\mathbf{A} - \mathbf{D}_2) \mathbf{A}_{\text{MMs}}^{-1}] \mathbf{r}. \quad (3.25)$$

Here \mathbf{B}_d and \mathbf{C}_d are the basis- and correction-function operators for the reconstruction. For dual cells that are not intersecting level-2 coarse boundaries, the corresponding entries of \mathbf{B}_1 and \mathbf{C}_1 can be reused (a more detailed discussion about reusing basis functions is given in Chapter 3.6). From $\mathbf{p}_{c,1}$, which allows computing fine-scale fluxes that are conservative on the

level-1 coarse grid, we reconstruct the final fine-scale pressure as the solution of

$$\mathbf{D}_1 \mathbf{p}_{c,0} = [\mathbf{I} - (\mathbf{D}_2 - \mathbf{D}_1) \mathbf{D}_{2,Ms}^{-1}] [\mathbf{I} - (\mathbf{A} - \mathbf{D}_2) \mathbf{A}_{MMs}^{-1}] \mathbf{r}, \quad (3.26)$$

which involves solving problems of the same computational cost as in the MsFV reconstruction step.

In case of n -levels of coarsening the nested reconstruction can be obtained by solving

$$\mathbf{D}_1 \mathbf{p}_{c,0} = \prod_{i=1}^n [\mathbf{I} - (\mathbf{D}_{i+1} - \mathbf{D}_i) \mathbf{D}_{i+1,Ms}^{-1}] \mathbf{r}, \quad (3.27)$$

where $\mathbf{D}_{n+1,Ms} = \mathbf{A}_{MMs}$.

3.5 Iterative improvement of the solution

Due to the localization assumption, the MsFV method might yield inaccurate solutions for particularly difficult problems, e.g., highly anisotropic permeability fields or large grid aspect ratios [55]. Several adaptive, iterative strategies have been recently proposed [23, 25, 58, 76] to improve the quality of the MsFV solution. They showed that the solution from the iterative MsFV (iMsFV) converges to the reference fine-scale solution if a sufficient number of iterations is employed. Following [58], we use the MsFV or the MMsFV operators as preconditioners, \mathbf{P} , in the iterative scheme

$$\mathbf{p}^{\nu+1} = \mathbf{p}^{\nu} + \omega^{\nu} \mathbf{P}^{-1} (\mathbf{r} - \mathbf{A} \mathbf{p}^{\nu}), \quad (3.28)$$

where $\mathbf{P}^{-1} = \mathbf{A}_{Ms}^{-1}$ for iMsFV and $\mathbf{P}^{-1} = \mathbf{A}_{MMs}^{-1}$ for iMMsFV, respectively. The index ν denotes the iteration level and ω^{ν} is a relaxation parameter. In this paper, we will apply the Generalized Minimal Residual (GMRES) method [67], which is equivalent to finding the relaxation parameters $(\{\omega^i\}_{i=1,2,\dots,\nu})$ that minimize the l_2 -norm of the preconditioned normalized residual, $\epsilon = \|\mathbf{P}^{-1} (\mathbf{r} - \mathbf{A} \mathbf{p}^{\nu})\|_2 / \|\mathbf{r}\|_2$ [58].

Defining $\chi_P = \prod_{i=1}^n \chi_{n+1-i}$, $\mathbf{B}_P = \prod_{i=1}^n \mathbf{B}_i$, and recalling Eqs. (3.18), (3.19), and (3.20), we observe that

$$\chi_P \mathbf{A} \mathbf{P}^{-1} = \chi_P \mathbf{A} \mathbf{B}_P (\chi_P \mathbf{A} \mathbf{B}_P)^{-1} \chi_P (\mathbf{I} - \mathbf{A} \mathbf{S}_n) + \chi_P \mathbf{A} \mathbf{S}_n = \chi_P, \quad (3.29)$$

and we write

$$\chi_P (\mathbf{r} - \mathbf{A} \mathbf{p}^{\nu+1}) = (1 - \omega^{\nu}) \chi_P (\mathbf{r} - \mathbf{A} \mathbf{p}^{\nu}), \quad (3.30)$$

which indicates that, if the initial solution, \mathbf{p}^0 , has zero residual on the coarsest grid, the residual remains zero at any successive iteration (this is valid for the MMsFV and for the MsFV operators, since the latter is recovered from the multilevel operator for $n = 1$). Therefore, GMRES can be stopped at any arbitrary iteration step and a conservative velocity field can be constructed following the procedure outlined in the previous section. Notice that Eq. (3.30) holds in combination with any smoother \mathbf{S}_n^{-1} because the condition $\chi_p \mathbf{A} \mathbf{P}^{-1} = \chi_p$ is sufficient.

Finally we observe that Eq. (3.28) can be used to project any solution with non-zero residual to a solution with zero residual if $\omega^\nu = 1$ is chosen.

The iterative scheme described in Eq. (3.28) can also be applied to the multiscale approximation of $\mathbf{D}_{2,Ms}$, Eq. (3.24), in the nested reconstruction to avoid that the localization assumptions introduced in the decoupled multiscale problems lead to a deterioration of the quality of the conservative velocity.

3.6 Complexity analysis

In this section we first analyze the computational complexity of the MsFV method to show that a multilevel extension of the algorithm is necessary to keep the method efficient. Then, we discuss the costs of the additional local operators and of the nested reconstruction that are required in a multilevel formulation. Finally, we derive the theoretical speed-up that can be achieved with an iterative multilevel algorithm. Here, a complexity analysis is preferred because it allows highlighting the intrinsic characteristics of the algorithms, whereas a comparison of CPU time is largely influenced by the specific implementation and by the hardware architecture employed.

3.6.1 Complexity of MsFV

The cost of solving a problem of N unknowns with a specific solver can be estimated as (see, e.g., [11])

$$\zeta = a_\alpha N^\alpha, \quad (3.31)$$

where α and a_α are the solver dependent exponent and prefactor, respectively. Whereas for a direct solver they can be approximated to $\alpha = 2$ and $a_\alpha = 1$ [11], in case of an optimally implemented Multigrid iterative solver, α can vary between 1.2 and 1.4 [42] and a_α can be rather large (we assume $a_\alpha > 50$ in this case). Notice that exact values strongly depend on the number of bands and the sparsity of the matrix \mathbf{A} .

For the complexity of MsFV, we further assume that the number of coarse cells and dual cells is approximately the same and that the costs of solving localized problems on coarse and dual cells are identical. Consequently the cost of MsFV can be written as

$$\zeta_{Ms} = \mathcal{F}(2N_1)\Upsilon^2 + a_\alpha N_1^\alpha = 2\mathcal{F}N\Upsilon + a_\alpha N^\alpha \Upsilon^{-\alpha}, \quad (3.32)$$

where Υ is the D -dimensional upscaling factor ($\Upsilon = \Upsilon_x \cdot \Upsilon_y$ in 2D and $\Upsilon = \Upsilon_x \cdot \Upsilon_y \cdot \Upsilon_z$ in 3D, where e.g., Υ_x is the upscaling factor in the direction x), $2N_1 = 2N/\Upsilon$ is the number of coarse and dual cells and \mathcal{F} is an adaptivity factor that accounts for the fact that, for time dependent problems, only in a portion of the domain basis and correction functions have to be updated and a conservative velocity field needs to be reconstructed [25, 26, 45, 49]. In Eq. (3.32) it has also been supposed that the local problems, which are $2^D + 1$, are solved with a direct solver

and that the factorization is stored, such that the cost of solving these problems is negligible with respect to the cost of computing the factorization, which has to be computed only once.

In Fig. 3.2 the costs of calculating the MsFV basis and correction functions are compared to the cost of solving the MsFV coarse problem for two different exponents of the linear solver. Costs are illustrated for different upscaling factors $\Upsilon^{\frac{1}{D}}$ and number of unknowns N . According to the results obtained for time dependent problems in previous work, e.g., [49], \mathcal{F} has been fixed to 0.2. It can be observed that for small upscaling factors the solution of the coarse problem dominates the computational efficiency of MsFV. A larger number of unknowns or the use of direct solvers increases the predominance of the coarse problem already for larger upscaling factors. For all these cases a multilevel extension is required to keep the MsFV solution efficient.

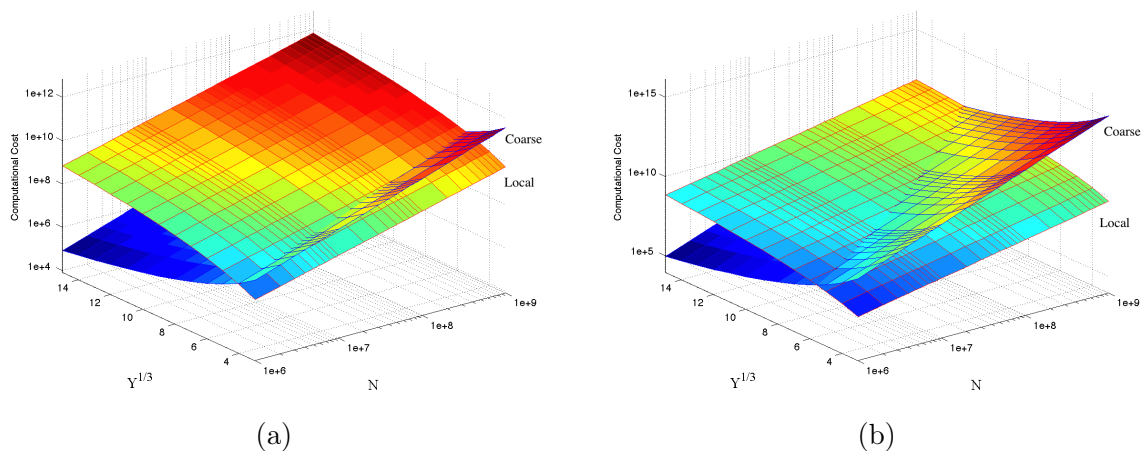


Figure 3.2: Comparison of computational cost of MsFV coarse problem, $\mathbf{M}_{nn}^{-1}\mathbf{q}_n$, and of MsFV local problems, \mathbf{B} and \mathbf{C} , for different upscaling factors $\Upsilon^{1/3}$, and different number of fine cells N using $\mathcal{F} = 0.2$. Two different linear solvers are considered: (a) an iterative solver with $\alpha = 1.3$ and $a_\alpha = 50$; (b) a direct solver with $\alpha = 2$ and $a_\alpha = 1$.

3.6.2 Complexity of MMsFV

For the MMsFV method the cost of building basis and correction functions is increased because a set of basis and correction functions has to be computed for each of the n coarse levels. The estimated cost of this operation is

$$\zeta_{\text{MMs,bfp}} = \sum_{i=1}^n \mathcal{F}N_i\Upsilon^2 = \mathcal{F}N\Upsilon \sum_{i=0}^{n-1} \left(\frac{1}{\Upsilon}\right)^i = \mathcal{F}N\Upsilon \frac{\Upsilon - \Upsilon^{1-n}}{\Upsilon - 1}. \quad (3.33)$$

The increase in computational cost due to the additional sets of basis and correction functions is bounded by the factor

$$\frac{\Upsilon - \Upsilon^{1-n}}{\Upsilon - 1} \leq \frac{\Upsilon}{\Upsilon - 1} = 1 + \frac{1}{\Upsilon - 1}. \quad (3.34)$$

For $\Upsilon = 3^D$, the relative extra costs are about 4% in 3D, resp. 13% in 2D, smaller than the costs of constructing basis and correction functions in the MsFV method. These extra costs decrease with the upscaling factor and can be in general neglected, particularly for realistic 3D problems.

Also the cost of reconstructing a conservative velocity field is increased. In addition to the final reconstruction step that has the same cost as in the MsFV method, the nested reconstruction requires computing new basis and correction functions for the decoupled MsFV to be solved in each coarse cell of level $n \geq 2$, as well as solving the corresponding coarse problems. The cost of computing basis and correction functions can be estimated as

$$\zeta_{\text{MMs,bfr}} = \beta \Upsilon \sum_{i=1}^{n-1} \mathcal{F}N_i \Upsilon^2 = \beta \mathcal{F}N \Upsilon \frac{\Upsilon - \Upsilon^{2-n}}{\Upsilon - 1}, \quad (3.35)$$

where the factor $\beta \lesssim 0.25$ takes into account that some of the factorizations of the pressure basis and correction functions can be reused (see App.3.9.2 for a detailed estimation). The cost of solving the set of coarse problems (one per each coarse cell of each coarse grid from level-2 to level-n) is approximately

$$\zeta_{\text{MMs,cr}} = \sum_{i=2}^n \mathcal{F}N_i \Upsilon^2 = \mathcal{F}N \sum_{i=0}^{n-2} \left(\frac{1}{\Upsilon}\right)^i = \mathcal{F}N \frac{\Upsilon - \Upsilon^{2-n}}{\Upsilon - 1}. \quad (3.36)$$

Then the total cost of the nested reconstruction is

$$\zeta_{\text{MMs,nr}} = \zeta_{\text{MMs,bfr}} + \zeta_{\text{MMs,cr}} = \mathcal{F}N \Upsilon \left[1 + \left(\beta + \frac{1}{\Upsilon} \right) \frac{\Upsilon - \Upsilon^{2-n}}{\Upsilon - 1} \right], \quad (3.37)$$

which is bounded by the value corresponding to an infinite number of levels, $n \gg 1$, and we can write

$$1 + \left(\beta + \frac{1}{\Upsilon} \right) \frac{\Upsilon - \Upsilon^{2-n}}{\Upsilon - 1} \leq 1 + \frac{1 + \Upsilon\beta}{\Upsilon - 1}. \quad (3.38)$$

It is easy to see that the increase in relative computational cost is maximum for the smallest upscaling factor. For $\Upsilon = 3^D$ and β as given in App.3.9.2, in 3D (resp. 2D) the cost of the nested reconstruction is about 30% (resp. 40%) more expensive than the MsFV reconstruction.

The total cost of MMsfv can be finally written as

$$\zeta_{\text{MMs}} = 2\mathcal{F}N\Upsilon \left(1 + \frac{1 + \Upsilon\beta/2}{\Upsilon - 1} \right) + a_\alpha N^\alpha \Upsilon^{-\alpha} \left[\Upsilon^{\alpha(1-n)} \right]. \quad (3.39)$$

A comparison with the cost of the standard MsFV method, Eq. (3.32), reveals that for large problems the additional cost of the basis functions and of the reconstruction is largely compensated by the lower computational cost of the coarsest problem which tend to become negligible for a large number of levels. For $\Upsilon = 3^D$ (resp. $\Upsilon = 5^D$), for instance, the extra costs associated with basis functions, correction function, and velocity reconstruction are 27 % in 2D and 19 % in 3D (resp. 17 % in 2D and 14 % in 3D) the cost of the corresponding steps in the MsFV method. On the other hand, the cost of the coarse problem is reduced by a factor $\Upsilon^{\alpha(1-n)}$; this means that also for a 2-level MMsFV and an optimally performing iterative solver ($\alpha = 1.3$) the cost of the MMsFV coarse problem is 17 times less in 2D and 70 times less in 3D than the cost of the MsFV coarse problem for $\Upsilon = 3^D$. This efficiency gain however is paid in terms of accuracy and a larger number of iMMsFV iterations is required to improve the MMsFV solution.

3.6.3 Complexity of the iterative methods

If we neglect the effects of memory requirement on the computational efficiency, a single GMRES [67] iteration loop is equivalent to solving the coarse problem with an updated right hand side vector and prolongating the new coarse solution to the fine-scale. We therefore estimate the cost of the iterative MsFV method as

$$\zeta_{\text{iMs}} \approx 2\mathcal{F}N\Upsilon + a_\alpha (N_{\text{it},M_s}^2 + 1) N^\alpha \Upsilon^{-\alpha}, \quad (3.40)$$

where we used a quadratic scaling in the number of iterations N_{it,M_s} to account for the increasing cost of GMRES with increasing iteration numbers [67]. Accordingly the cost of iMMsFV can be approximated as

$$\zeta_{\text{iMMs}} \approx 2\mathcal{F}N\Upsilon \left(1 + \frac{1 + \Upsilon\beta/2}{\Upsilon - 1} \right) + a_\alpha (N_{\text{it},\text{iMMs}}^2 + 1) N^\alpha \Upsilon^{-\alpha} \left[\Upsilon^{\alpha(1-n)} \right]. \quad (3.41)$$

Equating Eqs. (3.40) and (3.41) and solving for $N_{\text{it},\text{iMMs}}/N_{\text{it},\text{iMs}}$ we obtain

$$\frac{N_{\text{it},\text{iMMs}}}{N_{\text{it},\text{iMs}}} \approx \Upsilon^{\frac{\alpha}{2}n} \sqrt{\Upsilon^{-\alpha} - 2a_\alpha^{-1}\mathcal{F}\Upsilon \frac{1 + \Upsilon\beta/2}{\Upsilon - 1} \frac{N^{1-\alpha}}{N_{\text{it},\text{iMs}}^2}} \approx \Upsilon^{\frac{\alpha}{2}(n-1)}, \quad (3.42)$$

where the last approximation takes into account that the increase in computational cost for the solution of additional local problems (second term under the square root sign) is negligible with respect to the efficiency gain for the coarse problem. By using the estimate for β in App. 3.9.2

this is easy to verify.

3.7 Numerical Simulations

3.7.1 Two-dimensional pressure solutions

All the 2D simulations in the following are performed in a rectangular domain discretized into 216×54 fine cells. A constant inflow condition ($q_{In} = 1,080 \text{ m}^3/\text{s}$) is applied at the left boundary while the pressure is fixed at the right boundary. The top and bottom boundaries are impermeable. First we consider a constant permeability field to examine the quality of the localization assumption in case of an underlying 9-point stencil discretization. For each level, an upscaling factor $\Upsilon = 3^2$ is used.

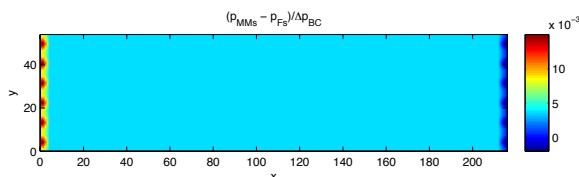


Figure 3.3: Relative MMsFV pressure error with respect to a standard fine-scale finite-volume pressure solution for a homogeneous permeability field. Due to the symmetry of the boundary conditions and the homogeneous permeability field the fine-scale as well as the MsFV pressure solutions are one-dimensional. For each level, an upscaling factor $\Upsilon = 3^2$ is used.

The relative error of the MMsFV pressure with respect to the fine-scale finite-volume solution is shown in Fig. 3.3. We observe that, in contrast to the solution of the standard MsFV method, the pressure field obtained by the MMsFV method differs from the linear pressure field obtained by the reference fine-scale solution: pressure errors can be observed at the left and at the right boundaries. Rather than being a specific feature of the multilevel algorithm, these errors originate from the fact that the underlying discretization is based on a 9-point stencil (instead of 5-point) and that in this case the localization assumption becomes less accurate. Indeed, fine-scale fluxes along edges now depend also on the neighbouring inner cells. For asymmetric reduced edge problems neglecting these connections generates spurious pressure gradients and deteriorates the quality of the solution.

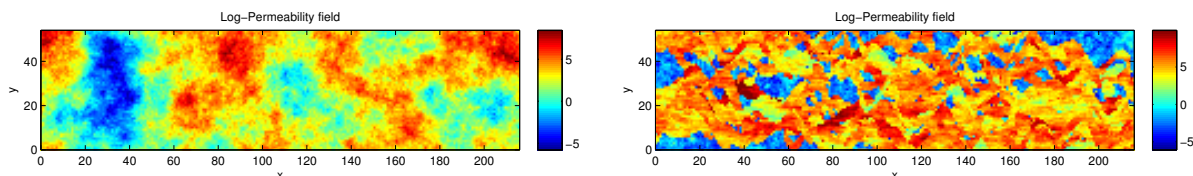


Figure 3.4: Spatially fitted SPE10 top (a) and bottom (b) log-permeability field [9].

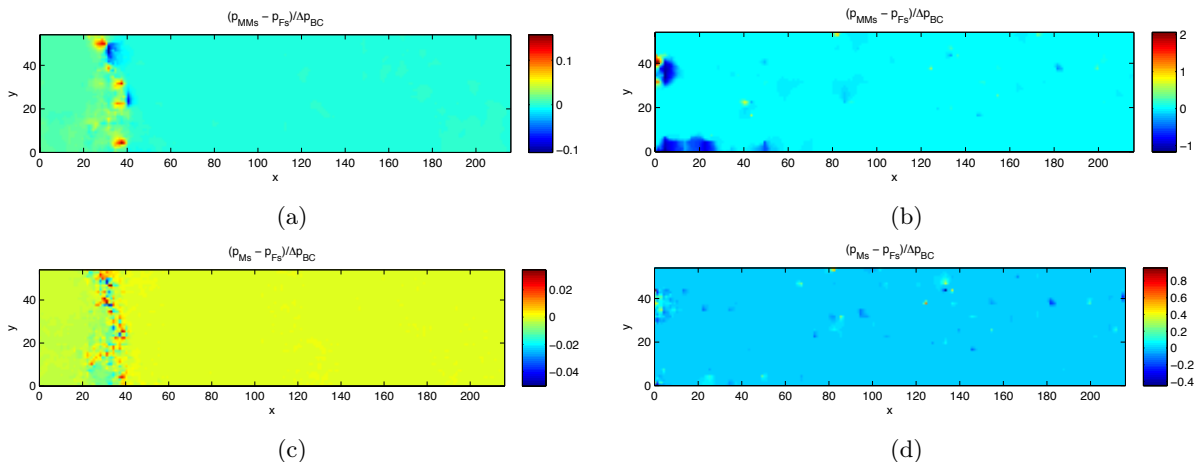


Figure 3.5: Relative pressure error with respect to a standard fine-scale finite-volume pressure solution for: (a) the MMsFV method and the SPE10 top layer; (b) the MMsFV method and the SPE10 bottom layer; (c) the MsFV method and the SPE10 top layer; (d) the MsFV method and the SPE10 bottom layer. For each level, an upscaling factor $\Upsilon = 3^2$ is used.

We now consider two heterogeneous permeability fields obtained from the top and bottom layer of the 10th SPE Comparative Solution Project (SPE10) [9]. The original two-dimensional fields have been truncated to match a discretization of 216×54 fine cells, Fig. 3.4. The relative pressure errors for the SPE10 top and bottom layers are shown in Fig. 3.5 (a) and Fig. 3.5 (b) for the MMsFV, and in Fig. 3.5 (c) and Fig. 3.5 (d) for the MsFV, respectively. Due to the additional approximations introduced by the level-2 coarse problem and by the reduced problems in case of an underlying 9-point stencil, the MMsFV errors are larger than MsFV errors. Notice that errors are larger in low-permeability regions for both methods.

3.7.2 Two-dimensional pressure convergence study

For practical applications it is important to evaluate whether the larger MMsFV errors can be efficiently controlled by the iterative improvement of the solution introduced in Chapter 3.5. Therefore, we consider the SPE10 top and bottom layers, and study the convergence history of GMRES iterations that employ the MsFV and the MMsFV operators as preconditioners.

The performance of the methods for the SPE10 top and bottom layers is shown in Fig. 3.6. To reduce the preconditioned normalized residual to $\epsilon = 10^{-6}$ the iMMsFV method takes about 5 and 18 times more iterations than the iMsFV for the SPE top and bottom layers, respectively. According to the results of the complexity analysis, Eq. (3.42), iMMsFV is more efficient than MsFV for the SPE10 top layer, but less efficient for the SPE10 bottom layer if a direct solver is employed.

In order to reduce the number of MsFV iterations, several strategies have been proposed in the past that can also be applied together with the MMsFV method. *Hajibeygi et al.* [23] used multiple Line-Relaxation (LR) steps to smooth the error residual. *Lunati et al.* [58] tested different type of smoother based on the MsFV data structure, and finally proposed to employ

a two-step GMRES preconditioner that combines the MsFV operator with a Dirichlet Additive Schwarz (DAS) or a Dirichlet Multiplicative Schwarz (DMS) smoother. Recently, *Zhou and Tchelepi* [76] examined the efficiency of the correction-function operator \mathbf{C} as a smoother and proposed to replace \mathbf{C} in the MsFV operator (Eq. (3.11)) by an alternative smoother \mathbf{S} . They observed that convergence is improved with a Block-ILU(0) (BILU) smoother.

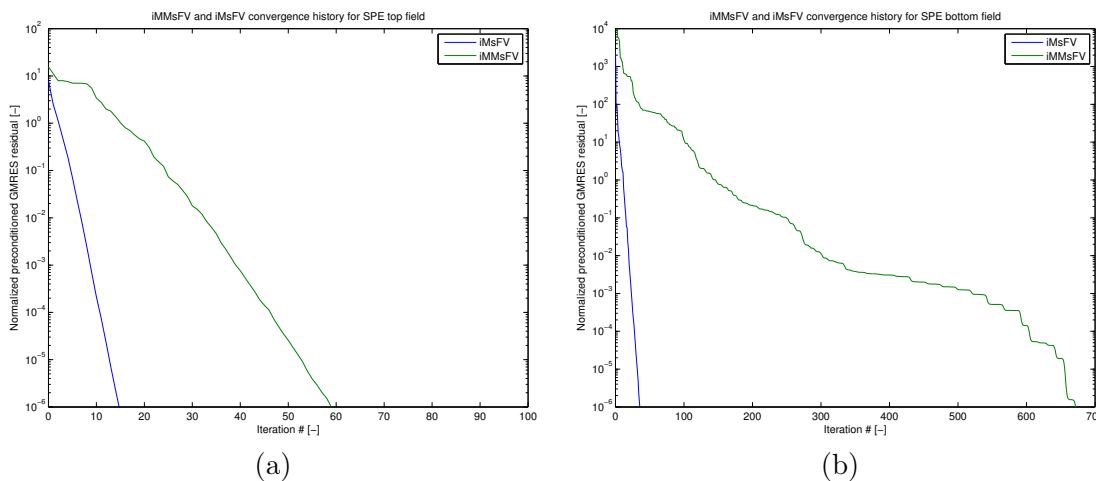


Figure 3.6: Convergence history iMsFV (blue) and iMMsFV (green) method for (a) SPE10 top layer; and (b) SPE10 bottom layer.

In Chapter 3.5 we showed, that the multiscale operator can be used to project any pressure solution onto a new pressure field that has zero residual on the coarsest grid and that allows reconstructing a conservative velocity field. This offers two different strategies: The first strategy is to iteratively apply the smoother a predefined times and then apply \mathbf{G} as defined in Chapter 3.4.2 to obtain a solution from which a conservative velocity can be reconstructed. This strategy, however, has the disadvantage that when the smoothed solution is projected onto a solution that has zero residual on the coarsest grid, the residual on the fine grid increases and additional smoothing steps might be necessary to control the residual [23, 58]. The second possibility is to apply \mathbf{G} in combination with a smoother as two-step preconditioner in GMRES [58]. This strategy has the advantage that, if \mathbf{G} is used as second preconditioner, the preconditioned error can be directly controlled in GMRES.

Fig. 3.7 (a) and (b) show the (non-preconditioned) normalized residuals for the SPE10 top and bottom layers. Notice that here an anisotropic permeability, $k_y = 10 k_x$ has been used for the SPE10 top layer. For both permeability fields the number of iMMsFV iterations can be significantly reduced by employing a two-step preconditioner that combines \mathbf{G} with a BILU smoother constructed on the blocks of the level-1 grid ($G^{-1} + BILU$). These results are consistent with the results obtained for the iMsFV method in [76], where the BILU smoother was constructed using different supports. Applying several BILU-smoothing steps (here we have employed 20 smoothing steps) and using \mathbf{G}^{-1} to allow reconstructing a conservative velocity

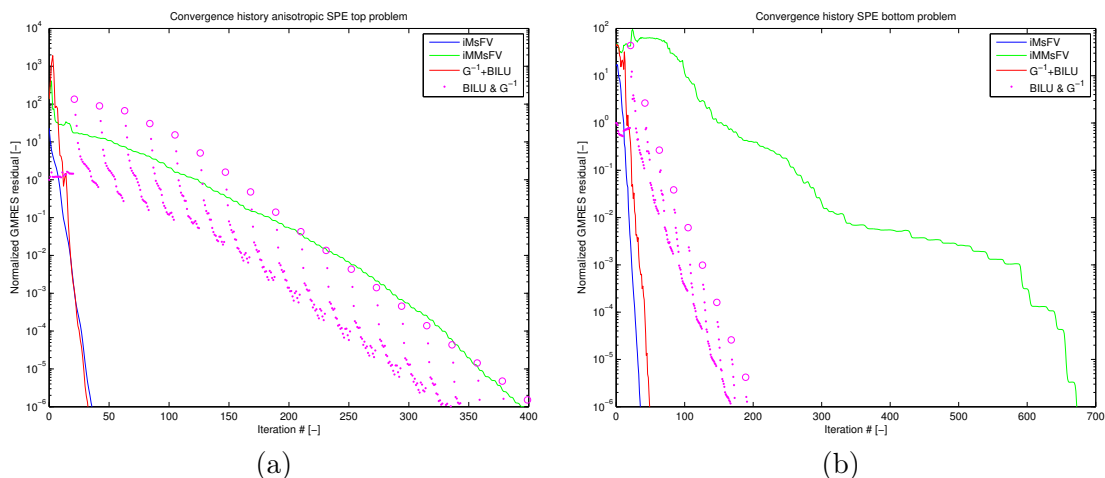


Figure 3.7: Convergence history of the normalized non-preconditioned norm: for the iMsFV method (blue); for the iMMsFV method (green); for the modified iMMsFV method in which the correction function is replaced by a BILU smoother (red); and for an iterative method that employs 20 BILU smoothing iterations and one application of \mathbf{G}^{-1} used to project the solution onto conservative space (magenta). Results are shown (a) for the SPE10 top layer with anisotropy ratio $k_y/k_x = 10$; and (b) for the SPE10 bottom layer.

field ($BILU \& G^{-1}$) leads to a method that is less efficient than the two-step preconditioner. It can be clearly seen, that applying \mathbf{G}^{-1} increases the non-preconditioned residual. This effect is more pronounced in case of the anisotropic test case, leading to the same total number of iterations as the traditional iMMsFV method.

3.7.3 Three-dimensional pressure convergence study

We consider a three-dimensional model of $81 \times 81 \times 81$ fine cells with a synthetic Gaussian permeability field. The log-permeability distribution is depicted in Fig. 3.8 (a). The variance of the permeability field is $\sigma = 0.75$ and the correlation length is $\lambda = 5$ cells. The pressure at the upper-back-right corner is fixed and a constant inflow rate of $50,000 \text{ m}^3/\text{s}$ is assigned at the lower-front-left corner. No-flow boundary conditions are applied elsewhere.

The convergence histories of iMMsFV and iMsFV are shown in Fig. 3.8 (b). More than 700 iMMsFV iterations are required to reduce the preconditioned normalized residual below $\epsilon = 10^{-6}$. It is obvious that, even for this moderately heterogenous field, the multilevel operator cannot be efficiently applied to three-dimensional problems and some modifications are necessary to control the number of iterations. As shown in the previous section, one possibility is to substitute the correction-function operator by a more effective smoother. Here, we propose a different strategy that aims at improving the localization assumption of the level-2 dual problems.

As shown in [55], the reduced boundary conditions for the local problems might lead to unphysical circulations in case of complex permeability fields or large grid aspect ratios. This

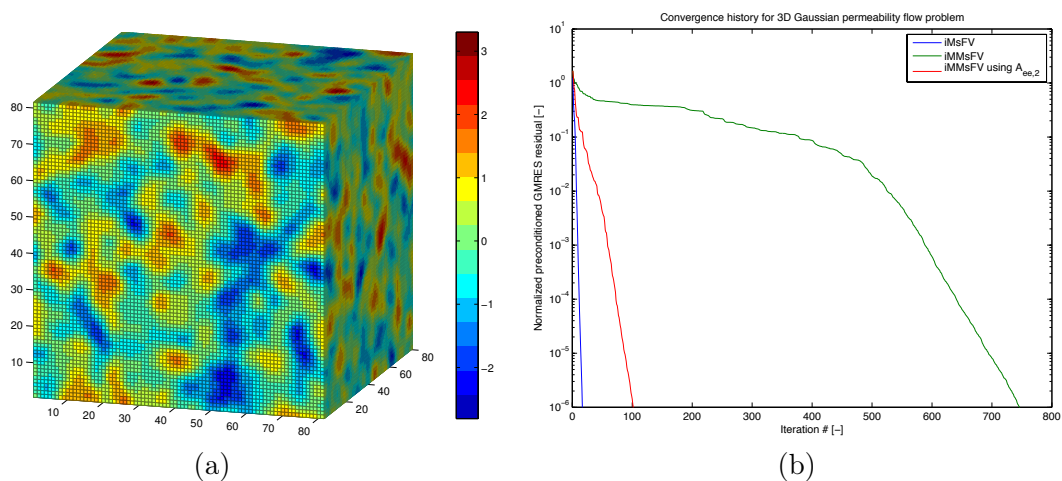


Figure 3.8: (a) Three-dimensional Gaussian log-permeability field consisting of $81 \times 81 \times 81$ fine cells with $\sigma = 0.75$ and $\lambda = 5$ cells. (b) Convergence history of iMMsFV and iMsFV for the three-dimensional Gaussian permeability field.

effect is more pronounced in MMsFV due to the localization assumption on the second level where reduced boundary conditions are employed with an underlying discretization based on a 9-point in 2D and a 27-point stencil in 3D. The boundary conditions of the local problems can be easily improved by adding back some of the connections that have been neglected.

To illustrate this idea, we keep the connections between level-2 edge cells belonging to different edges, which is equivalent to use $\mathbf{A}_{ee,2}$ instead of $\mathbf{M}_{ee,2}$ in the basis- and correction-function operators. The convergence history corresponding to this modified operator (i.e., with $\mathbf{A}_{ee,2}$ included) is shown in Fig. 3.8 (b). The number of iterations is reduced to about 100, and the convergence curve is located between the MsFV and MMsFV solutions. This demonstrates that keeping some of the connections effectively improves the convergence with a slight increase in computational costs.

3.7.4 Effect of the nested reconstruction on saturation results

Finally, we investigate the influence of the nested reconstruction on the accuracy of the solution and on the efficiency of the method for time dependent problems. We again use the SPE10 top layer permeability field, Fig. 3.4 (a), with an anisotropy ratio $k_y/k_x = 10$. For the transient simulations a viscosity ratio $M = \mu_1/\mu_2 = 0.1$ (unfavourable displacement) and a quadratic relative permeability relationship, $k_{r\gamma} = S_\gamma^2$, are employed. As in the previous 2D tests, the upper and the bottom boundaries are impermeable, the pressure is fixed on the right boundary and a constant inflow of the less viscous fluid is assigned at the left boundary. The upscaling factor used for each coarse level is $\Upsilon = 3^2$.

In Fig. 3.9 MMsFV velocity errors with respect to a fine-scale reference solution are compared with the corresponding MsFV velocity errors at 0.1 PVI. It can be observed that the

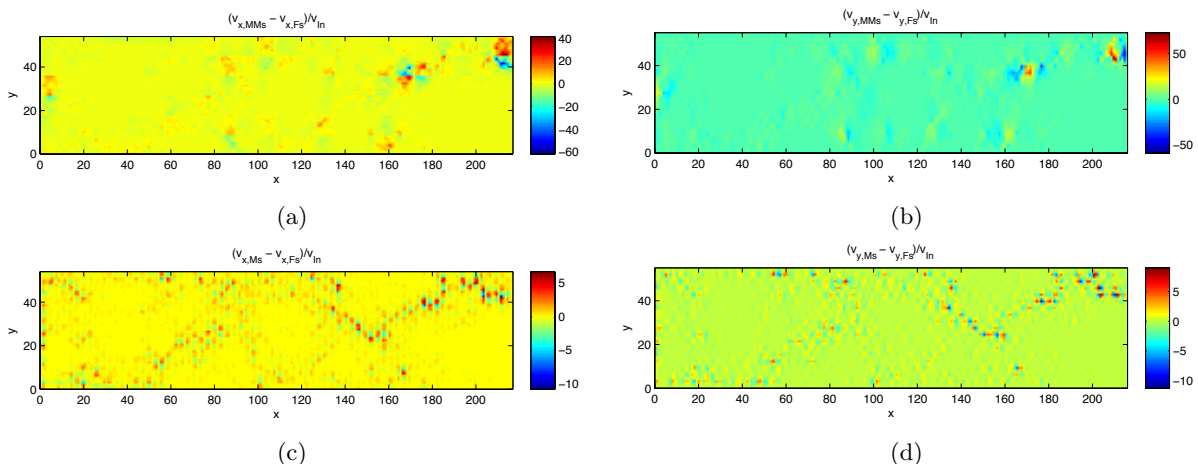


Figure 3.9: Relative vertical and horizontal velocity errors for the anisotropic SPE10 top layer with anisotropy ratio $k_y/k_x = 10$ at 0.1 PVI: (a) $(\mathbf{v}_{x,MMs} - \mathbf{v}_{x,Fs})/\mathbf{v}_{In}$; (b) $(\mathbf{v}_{y,MMs} - \mathbf{v}_{y,Fs})/\mathbf{v}_{In}$; (c) $(\mathbf{v}_{x,Ms} - \mathbf{v}_{x,Fs})/\mathbf{v}_{In}$; (d) $(\mathbf{v}_{y,Ms} - \mathbf{v}_{y,Fs})/\mathbf{v}_{In}$, where \mathbf{v}_{In} is the inflow velocity.

MMsFV errors are about six times larger than MsFV errors. These larger differences with respect to the reference originate from the inaccuracy of the multilevel pressure approximation, $\mathbf{p}_{MMs} = \mathbf{A}_{MMs}^{-1} \mathbf{r}$, as well as from the multiscale approximation employed in the nested reconstruction, Eq. (3.24). They can be both reduced iteratively: the iMMsFV algorithm can be employed in the pressure calculation, as well as in the nested reconstruction, i.e., to solve the decoupled multiscale problems defined on the cells of the coarsest discretization level.

Previous work [26] showed that for the anisotropic top SPE10 permeability field a satisfactory iMsFV saturation solution can be obtained with a threshold on the pressure residual of the order of $\epsilon = 10^{-3}$. Based on these results we use a residual threshold value $\epsilon = 10^{-4}$ for the iterated multilevel pressure \mathbf{p}_{MMs} . To investigate the errors introduced by the multiscale approximations used in the nested reconstruction, Eq. (3.24), we compare the saturation fields obtained with and without iterative improvement of the multiscale solution used in the reconstruction with the saturation field obtained by solving Eq. (3.23) exactly. The latter solution is very close to the fine-scale solution and will be used as a reference to guarantee that errors are only due to the approximations done in the nested reconstruction.

Fig. 3.10 (a) shows the iMMsFV saturation differences with respect to the reference solution at 0.2 PVI when no iteration is applied in the nested reconstruction. This leads to saturation errors around 0.15. The saturation differences obtained by iteratively improving the nested reconstruction are shown in Fig. 3.10 (b). The use of the iterative scheme greatly improves the quality of the saturation solution and differences are reduced to a maximum absolute value of $8 \cdot 10^{-6}$. The corresponding iMMsFV saturation fields obtained with and without iteration in the nested reconstruction are shown in Fig. 3.10 (c) and (d). It can be seen that the two solutions are similar and that also the solution obtained without iterative correction in the nested reconstruction satisfactorily captures the fine-scale flow characteristics.

For time dependent problems the number of iterations required can be reduced by using the pressure solution from the old time as initial guess for the new pressure solution. *Hajibeygi et al.* [26] have demonstrated that this can effectively limit the computational cost, but some care has to be taken to ensure that the solution at the new time is conservative on the coarse grid. Here, we have derived a formulation that allows the same strategy for the two-coarse-level iMMsFV (App. 3.9.3). The number of iMMsFV, iMsFV and nested reconstruction iterations that are necessary to guarantee a pressure residual below the threshold $\epsilon = 10^{-4}$ are plotted in Fig. 3.11 per pressure call. It can be observed that in comparison with the average number of iterations required in iMMsFV (i.e., 107.9) and iMsFV (i.e., 9.4) only very few reconstruction iterations are necessary (i.e., 5.1). This demonstrates that also for time dependent problems the total cost of the nested reconstruction is negligible even if iterations have to be employed to control the inaccuracies that originate from the nested reconstruction procedure.

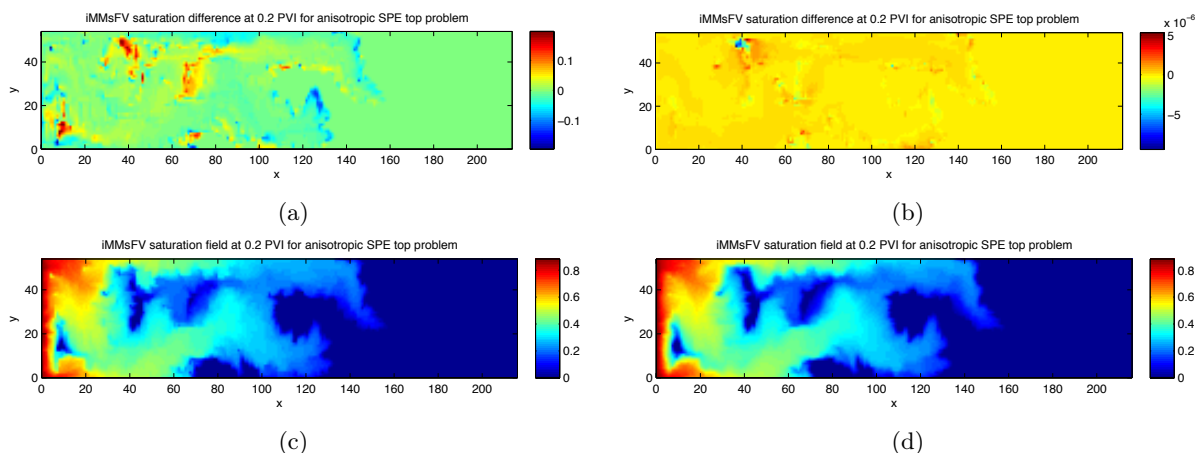


Figure 3.10: Comparison between the saturation distribution obtained by iMMsFV simulations without iterations inside the nested reconstruction (a) and in case iterations are employed inside the nested reconstruction to reduce the residual below the tolerance value $\epsilon = 10^{-4}$ (b) for SPE10 top layer with anisotropy ratio $k_y/k_x = 10$ at 0.2 PVI. Shown are differences with respect to an iMMsFV solution that is obtained by reconstructing the conservative velocity exactly on decoupled level-2 problems for the iMMsFV method. The corresponding iMMsFV saturation distributions are shown in (c) and (d). In both cases iterations with a tolerance value $\epsilon = 10^{-4}$ are used to improve the iMMsFV pressure, which is used to obtain the Neumann boundary fluxes on the level-2 coarse boundaries.

3.8 Conclusions

We have introduced a framework that extends the Multiscale Finite-Volume (MsFV) method to employ multiple levels of coarsening (MMsFV) and that includes a novel and efficient reconstruction procedure. Instead of directly solving problems on coarsest cells, the nested reconstruction uses again an MsFV approximation on decoupled coarsest problems. By means of a

complexity analysis we have demonstrated that the extra cost of constructing the additional basis and correction functions, as well as the cost of the nested reconstruction, are negligible and can be largely compensated by the dramatic reduction of the computational cost necessary to solve the coarsest problem. This efficiency gain is paid in terms of accuracy and MMsFV errors are much larger than MsFV errors. As for the MsFV method [58], these errors can be controlled by using the MMsFV operator as preconditioner in GMRES. Our numerical results showed, however, that for highly heterogeneous 2D permeability fields or for 3D permeability fields with moderate heterogeneity, several hundreds of iterations might be required to obtain a satisfactory solution.

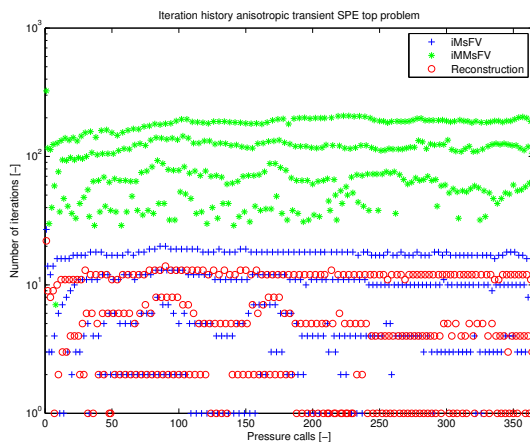


Figure 3.11: Number of iMsFV, iMMsFV and nested reconstruction iterations per pressure call for SPE10 top layer with anisotropy ratio $k_y/k_x = 10$ and a preconditioned error of $\epsilon = 10^{-4}$.

Since such a large number of iterations might be intractable for large problems due to memory requirements and computational cost, we have proposed two ideas to control the number of iterations and to keep the method efficient. The first strategy is to employ different smoother operators [23, 58, 76]. We have shown that the use of a two-step preconditioner can significantly reduce the number of iterations. Here, following the good results obtained in [76], we have substituted the correction-function operator with a BILU smoother, but many other choices are possible. The question of identifying the optimal smoother to be used in conjunction with the MMsFV operator has not been investigated and could be addressed in future work.

The second strategy consists in modifying the localization assumption for the coarser discretization levels, which is particularly important because the underlying discretization is based on a 27-point, resp. 9-point, stencil in 3D, resp. 2D. To illustrate this idea, we have considered an MMsFV operator in which connections between adjacent edges are maintained (this is equivalent to use $\mathbf{A}_{ee,2}$ instead of $\mathbf{M}_{ee,2}$ in the basis- and correction-function operators) and we have shown that a substantial reduction of the number of iterations can be obtained.

The MMsFV framework is especially suited for problems involving the solution of a trans-

port equation: the multilevel method can also be employed as an adaptive solution method. In presence of gravity effects, for instance, a very coarse description (e.g., on coarse level 2 or higher) of flow and transport might be sufficient in most regions, but close to an unstable front a fine-scale description (level 0) is necessary to correctly capture the instability. In this case, the MMsFV solution can be improved locally and adaptively, reducing the overall computational cost. For these problems, a multilevel framework can also be used as downscaling technique in a way similar as presented in [45], allowing multiple levels of refinement close to the unstable front.

Acknowledgments

This project is supported by Chevron ETC, Chevron/ Schlumberger Technology Alliance and the Swiss National Science Foundation grant No. FNS PP00P2_123419/1.

3.9 Appendix

3.9.1 MsFV operators

In case of 3D, 27-point stencil fine-scale discretizations, the dual grid introduces a partition of fine cells into inner (i), surface (s), edge (e) and node (n) cells (see Fig. 3.1 (b)). With an appropriate permutation operator, Eq. (3.7) can be reordered such that the discrete system reads

$$\begin{bmatrix} \mathbf{A}_{ii} & \mathbf{A}_{is} & \mathbf{A}_{ie} & \mathbf{A}_{in} \\ \mathbf{A}_{si} & \mathbf{A}_{ss} & \mathbf{A}_{se} & \mathbf{A}_{sn} \\ \mathbf{A}_{ei} & \mathbf{A}_{es} & \mathbf{A}_{ee} & \mathbf{A}_{en} \\ \mathbf{A}_{ni} & \mathbf{A}_{ns} & \mathbf{A}_{ne} & \mathbf{A}_{nn} \end{bmatrix} \begin{bmatrix} \mathbf{p}_i \\ \mathbf{p}_s \\ \mathbf{p}_e \\ \mathbf{p}_n \end{bmatrix} = \begin{bmatrix} \mathbf{r}_i \\ \mathbf{r}_s \\ \mathbf{r}_e \\ \mathbf{r}_n \end{bmatrix}. \quad (3.43)$$

For a 9-point stencil discretization we have $\mathbf{A}_{in} = \mathbf{A}_{ni} = \mathbf{A}_{ie} = \mathbf{A}_{ei} = \mathbf{A}_{sn} = \mathbf{A}_{ns} = \mathbf{0}$ and for 2D flow all blocks that contain the index s become $\mathbf{0}$. To simplify notation, we drop the permutation operator and refer to $\mathbf{A}\mathbf{p} = \mathbf{r}$ as the reordered system. The dual grid is used to define a set of local problems, which are obtained by neglecting: the influence of inner cells on surface, edge and node cells ($\mathbf{A}_{si} = \mathbf{A}_{ei} = \mathbf{A}_{ni} = \mathbf{0}$); the influence of surface cells on edge and node cells ($\mathbf{A}_{es} = \mathbf{A}_{ns} = \mathbf{0}$); and the influence of edge cells on node cells ($\mathbf{A}_{ne} = \mathbf{0}$). Neglecting off-diagonal blocks requires modifying the diagonal blocks. We therefore replace \mathbf{A}_{ss} and \mathbf{A}_{ee} by \mathbf{M}_{ss} and \mathbf{M}_{ee} , and we write

$$\begin{bmatrix} \mathbf{A}_{ii} & \mathbf{A}_{is} & \mathbf{A}_{ie} & \mathbf{A}_{in} \\ \mathbf{0} & \mathbf{M}_{ss} & \mathbf{A}_{se} & \mathbf{A}_{sn} \\ \mathbf{0} & \mathbf{0} & \mathbf{M}_{ee} & \mathbf{A}_{en} \\ \mathbf{0} & \mathbf{0} & \mathbf{0} & \mathbf{M}_{nn} \end{bmatrix} \begin{bmatrix} \mathbf{p}_i \\ \mathbf{p}_s \\ \mathbf{p}_e \\ \mathbf{p}_n \end{bmatrix} = \begin{bmatrix} \mathbf{r}_i \\ \mathbf{r}_s \\ \mathbf{r}_e \\ \mathbf{q}_n \end{bmatrix}, \quad (3.44)$$

where $\mathbf{M}_{nn}\mathbf{p}_n = \mathbf{q}_n$ is the coarse-scale problem [57]. From Eq. (3.44) the basis-function operator

and the correction-function operator can be readily obtained by backward substitution, which yields

$$\mathbf{B} = \begin{bmatrix} \mathbf{A}_{ii}^{-1}(\mathbf{A}_{ie}\mathbf{M}_{ee}^{-1}\mathbf{A}_{en} - \mathbf{A}_{in} + \mathbf{A}_{is}\mathbf{M}_{ss}^{-1}(\mathbf{A}_{sn} - \mathbf{A}_{se}\mathbf{M}_{ee}^{-1}\mathbf{A}_{en})) \\ \mathbf{M}_{ss}^{-1}(\mathbf{A}_{se}\mathbf{M}_{ee}^{-1}\mathbf{A}_{en} - \mathbf{A}_{sn}) \\ -\mathbf{M}_{ee}^{-1}\mathbf{A}_{en} \\ \mathbf{I}_{nn} \end{bmatrix} \quad (3.45)$$

and

$$\mathbf{C} = \begin{bmatrix} \mathbf{A}_{ii}^{-1} & -\mathbf{A}_{ii}^{-1}\mathbf{A}_{is}\mathbf{M}_{ss}^{-1} & \mathbf{A}_{ii}^{-1}(\mathbf{A}_{is}\mathbf{M}_{ss}^{-1}\mathbf{A}_{se}\mathbf{M}_{ee}^{-1} - \mathbf{A}_{ie}\mathbf{M}_{ee}^{-1}) & \mathbf{0} \\ \mathbf{0} & \mathbf{M}_{ss}^{-1} & -\mathbf{M}_{ss}^{-1}\mathbf{A}_{se}\mathbf{M}_{ee}^{-1} & \mathbf{0} \\ \mathbf{0} & \mathbf{0} & \mathbf{M}_{ee}^{-1} & \mathbf{0} \\ \mathbf{0} & \mathbf{0} & \mathbf{0} & \mathbf{0} \end{bmatrix} \quad (3.46)$$

respectively. Notice that \mathbf{B} and \mathbf{C} can also be derived by a Schur complement formulation with tangential approximation [57, 60].

3.9.2 Calculation of β

In order to estimate the coefficient β , we need to calculate the number of duals cells of the level i that are intersected by the boundary of a coarse cell of the level $(i + 1)$. For these cells, new matrix factorizations have to be performed to compute basis and correction functions. For each coarse cell, we have the following new problems to solve: 2^D dual problems of size $(\Upsilon^{1/D} - 1)^D/2^D \approx \Upsilon/2^D$ adjacent to the coarse cell corners; $2^{D-1}D(\Upsilon^{1/D} - 1)$ problems of size $(\Upsilon^{1/D} - 1)^D/2^{D-1} \approx \Upsilon/2^{D-1}$ adjacent to the coarse cell edges; and, for 3D problems, also $2^{D-2}D(\Upsilon^{1/D} - 1)^2$ problems of size $(\Upsilon^{1/D} - 1)^D/2^{D-2} \approx \Upsilon/2^{D-2}$ adjacent to the coarse cell faces.

Then, for each level- i , the total costs of recomputing local operators can be estimated as

$$\zeta \approx \frac{N_i}{\Upsilon^2} \left[\frac{\Upsilon^2}{2^D} + D(\Upsilon^{1/D} - 1)\frac{\Upsilon^2}{2^{D-1}} + D(\Upsilon^{1/D} - 1)^2\frac{\Upsilon^2}{2^{D-2}}\delta_{3D} \right], \quad (3.47)$$

where the Kronecker delta, δ_{3D} (equal to one if $D = 3$ and to zero otherwise), accounts for the fact that the last term appears only if $D = 3$. Rearranging and dividing by the cost of computing the standard basis and correction functions for the level i , $N_i\Upsilon$, we obtain

$$\beta \approx \frac{1}{2^D\Upsilon} \left[1 + 2D(\Upsilon^{1/D} - 1) + 4D(\Upsilon^{1/D} - 1)^2\delta_{3D} \right]. \quad (3.48)$$

3.9.3 2-Level reuse formulation

To keep the iMsFV method efficient for time dependent problems, the MsFV pressure at the old time step, \mathbf{p}^t , can be used as the initial pressure solution at the new time step [26],

$$\mathbf{p}^{t+1,0} = (\mathbf{A}_{\text{Ms}}^{t+1})^{-1}\mathbf{r}^{t+1} + [(\mathbf{A}_{\text{Ms}}^{t+1})^{-1} - \mathbf{B}^{t+1}(\chi\mathbf{A}^{t+1}\mathbf{B}^{t+1})^{-1}\chi](\mathbf{M}^t\mathbf{p}^t - \mathbf{r}^t). \quad (3.49)$$

In a 2-coarse-level iMMsFV the solution reused from the previous time step can be written as

$$\begin{aligned} \mathbf{p}^{t+1,0} = & (\mathbf{A}_{\text{MMs}}^{t+1})^{-1} \mathbf{r}^{t+1} + \\ & [(\mathbf{A}_{\text{MMs}}^{t+1})^{-1} - \mathbf{B}_1^{t+1} \mathbf{B}_2^{t+1} (\chi_2 \chi_1 \mathbf{A}^{t+1} \mathbf{B}_1^{t+1} \mathbf{B}_2^{t+1})^{-1} (\chi_2 - \chi_2 \chi_1 \mathbf{A}^{t+1} \mathbf{B}_1^{t+1}) \chi_1 - \mathbf{B}_1^{t+1} \mathbf{C}_2^{t+1} \chi_1] \mathcal{R}_1 - \\ & [(\mathbf{B}_1 \mathbf{B}_2 (\chi_2 \chi_1 \mathbf{A}^{t+1} \mathbf{B}_1^{t+1} \mathbf{B}_2^{t+1})^{-1} \chi_2 \chi_1 \mathbf{A}^{t+1} \mathbf{B}_1^{t+1} - \mathbf{B}_1^{t+1} \mathbf{C}_2^{t+1})] (\chi_1 \mathbf{A}_1^t \mathbf{C}_1^t \mathcal{R}_1 + \mathcal{R}_2), \end{aligned} \quad (3.50)$$

with the level-1 residual

$$\mathcal{R}_1 = \mathbf{M}_1^t \mathbf{p}^t - \mathbf{r}, \quad (3.51)$$

and the level-2 residual

$$\mathcal{R}_2 = \mathbf{M}_{\text{nn},1}^t \mathbf{p}_n^t - (\chi_1 - \chi_1 \mathbf{A}_1^t \mathbf{C}_1^t) \mathbf{r}, \quad (3.52)$$

respectively. In Eq. (3.52), $\mathbf{M}_{\text{nn},1}^t \mathbf{p}_n^t$ denotes the multilevel approximation of the level-1 coarse problem.

Chapter 4

Local modeling of instability onset for global finger evolution

Rouven Künze, Pavel Tomin, and Ivan Lunati

submitted to *Advances in Water Resources*

4.1 Abstract

Simulation of density-driven instabilities requires flexible methods to deal with the different spatial and temporal scales involved. Downscaling approaches based on standard adaptive grid refinement aim at resolving the fine-scale details only in the region of interest, but they may become computationally expensive in presence of very corrugated unstable fronts because the problem to be solved approaches the size of the fully refined system. The Downscaling Multiscale Finite-Volume (DMsFV) method overcomes this issue by splitting the problems into a set of localized subproblems that interact only through a global problem. However, in presence of convective instabilities (e.g., density-driven fingers) the diffusion scale has to be resolved only at early times to capture the evolution of infinitesimal random perturbations, whereas at later times fingers have developed and merged, allowing the use of a coarser numerical description. Based on this observation, we present an adaptive algorithm which splits the simulation into three stages: an onset stage in which a set of localized problems is solved independently to capture the initial growth of the instability; a transition stage in which the DMsFV method is used to couple local and global scale; and a global stage in which only a fully coarsened description of the problem is employed. The dissolution-diffusion-convection problem (which is typically studied in the context of CO₂ sequestration) is chosen as an example to evaluate the accuracy of the adaptive algorithm. For this problem, the use of a coarse grid that does not resolve the fine-scale details at earlier times leads to a dramatic underestimation of mass influx and penetration depth. On the contrary, the solutions obtained with the adaptive algorithm are in good agreement with the reference solution (obtained with a fully refined discretization) and are able to capture total mass influx and penetration depth with excellent accuracy. This demonstrates the need and the effectiveness of modeling local details during the instability onset to capture large-scale features of the concentration patterns at later times.

4.2 Introduction

Density-driven instabilities can be observed in a variety of subsurface-flow processes, e.g., seawater intrusion in coastal aquifers [33], geological storage of CO₂ [28, 29, 43], or in the presence of geothermal gradients [16, 17]. As a consequence of the convective instability, rapidly moving fingers form, which can drastically reduce the travel time. Although, they have been extensively studied in the last decades, e.g., [13, 18, 19, 65, 66, 75], accurate simulation in field-scale aquifer or reservoir modeling remains a challenge due to the disparity of scales involved.

To correctly capture the onset of instability and the finger-growth rate, it is important to resolve the fastest growing wavelength, which is the smallest mode that is not damped by diffusion and emerges from any initial infinitesimal random perturbation. This requires a very fine numerical discretization (with grid size below a centimeter, e.g., [63]) at least at early simulation times. In contrast, field-scale models consider subsurface flow processes that take place over several kilometers and normally employ cell-sizes in the order of several meters,

which is dictated by geological heterogeneities and by the constraints set by the computational costs.

This discrepancy between a computationally realistic and a physically sound discretization has fostered the development of several adaptive grid-refinement algorithms that refine the computational grid around the unstable front to capture the small scale behaviour, e.g., [63]. In these methods, however, the size of the larger problem that has to be solved, may approach the size of the fully refined problem if the instability front is large and complex. To avoid this issue, we have proposed a downscaling algorithm [45] that is based on the Multiscale Finite-Volume (MsFV) method [23, 36, 37, 52, 55, 57, 58]. The problem is downscaled by solving local problems, that are coupled through a global problem defined on the original grid; therefore, the larger problem is independent of the level of details. This framework, which employs clearly separated local and global problems, is particularly well suited to model instabilities.

In case of density instability, after an initial period dominated by diffusion, a critical time is reached at which convection starts to dominate. At early time, convection patterns are small compared to the size of the original discretization: their evolution is local and does not require global information. At later time, the convective patterns have grown such that they can be described by the original discretization and local details can be neglected. These observations naturally lead to define three stages that characterize finger evolution with respect to the original discretization: an onset or local stage; a transition stage; and a global stage.

In this paper we propose to solve only local decoupled problems during the onset stage, whereas the Downscaling MsFV (DMsFV) algorithm [45] is used for the transition stage, and the problem is solved on the original grid in the global stage. In this approach global and local problems can be solved adaptively.

The paper is organized as follows. The equations governing single-phase flow and transport are given in Chapter 4.3. In Chapter 4.4 we discuss the different scales, whereas Chapter 4.5 describes the three numerical schemes employed in the three different time stages. In Chapter 4.6 the performance of the adaptive algorithm is investigated with the help of the dissolution-diffusion-convection problem [20, 63, 65] for different durations of the onset stage and the results for ensemble realizations are analyzed. Finally, conclusions are drawn in Chapter 4.7.

4.3 Governing equations

We consider the flow of a single phase which consists of a solvent fluid and a solute. If we assume that the fluid is incompressible and employ the Boussinesq approximation (e.g., [33]), the fluid conservation equation takes the form

$$\nabla \cdot \mathbf{v} = 0, \quad (4.1)$$

where

$$\mathbf{v} = -\frac{k}{\mu} [\nabla p - \rho(c)\mathbf{g}]. \quad (4.2)$$

is the Darcy velocity.

In Eq. (4.2), k [m²] is the absolute permeability (which is assumed isotropic); p [Pa] the pressure; \mathbf{g} [m/s²] the gravity acceleration; ρ [kg/m³] the density of the fluid, which depends on the normalized concentration $0 \leq c \leq 1$ [-]; and μ [kg/m/s] the viscosity (concentration effects on viscosity are neglected for simplicity). The conservation equation for the solute mass can then be written as

$$\frac{\partial}{\partial t}(\phi c) + \nabla \cdot [c\mathbf{v} - \phi D_m \nabla c] = 0, \quad (4.3)$$

where ϕ [-] is the porosity; and D_m [m²/s] the molecular diffusion in the bulk solvent (we neglect mechanical dispersion). The equations above form a system of non-linear differential equations that are coupled by the density dependence on the solute concentration and by the velocity. To be solved, the equations need to be complemented with a constitutive relationship for $\rho(c)$ [33, 44]. As we are mainly concerned with moderate density contrasts, we assume a simple linear relationship of the form

$$\rho(c) = (1 - c)\rho_{\min} + c\rho_{\max}, \quad (4.4)$$

where ρ_{\min} and ρ_{\max} are the density at $c = 0$ and $c = 1$ respectively, e.g., [2, 32].

By defining the dimensionless quantities

$$\mathbf{v}^* = \frac{\mathbf{v}}{k\Delta\rho g/\mu}, \quad t^* = \frac{t}{L^2/\phi D_m}, \quad x^* = \frac{x}{L}, \quad (4.5)$$

where L is the characteristic length and $\Delta\rho = \rho_{\max} - \rho_{\min}$, we can write the system of non-dimensional equations as

$$\nabla \cdot \mathbf{v}^* = 0, \quad (4.6)$$

$$\frac{\partial c}{\partial t^*} + \text{Ra} \mathbf{v}^* \cdot \nabla c - \nabla^2 c = 0, \quad (4.7)$$

where

$$\text{Ra} = \frac{k\Delta\rho g L}{\phi\mu D_m} \quad (4.8)$$

is the dimensionless Rayleigh number, which describes the relative importance of convective to diffusive processes.

4.4 Characteristic length scales and adaptive algorithm

In the following, we will consider the dissolution-diffusion-convection (DDC) problem which has been extensively investigated in the past decade in the context of long-term geological storage of carbon dioxide [20, 63, 65]. This problem, which is a variant of classical density instability problems related to Rayleigh-Bénard convection [33] such as the Elder problem [13, 21, 73], is chosen here as an example, but the method proposed is general.

One application of this class of problem is to model the instability that arises when a layer of supercritical CO₂ stored in a deep saline aquifer is located above a denser brine layer. However,

the same process can take place in presence of mineral dissolution that can sensibly increase the density of the solution. Also, similar instabilities are triggered in presence of temperature gradients as in the case of a porous medium cooled from above (or heated from below); in this case the role played by diffusion is replaced by conduction and the density is modified by the thermal expansion of the fluid.

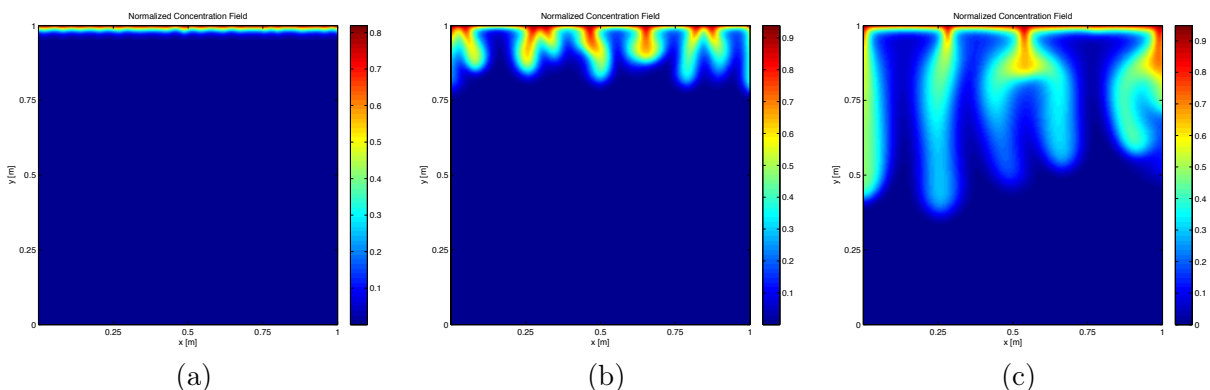


Figure 4.1: Normalized concentration fields for the dissolution-diffusion convection problem [20, 63, 65] at early (a), intermediate (b) and advanced (c) simulation time.

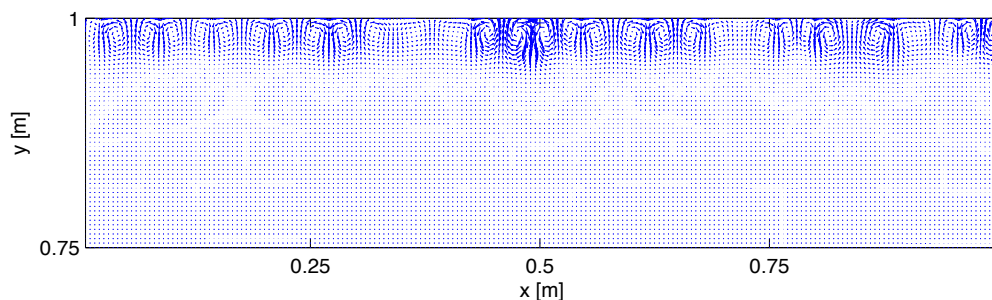


Figure 4.2: Extract of scaled velocity field for the situation shown in Fig. 4.1 (a).

4.4.1 Physical length scales

The DDC problem is illustrated in Fig. 4.1. We consider a porous medium of height H and width W , which is initially saturated by a solvent. At time $t = 0$, a solute starts to dissolve at the top boundary and diffuses into the solution forming a diffusive boundary layer, Fig. 4.1 (a). Since the solution has higher density than the solvent, the system is gravitationally unstable and small perturbations grow by affecting the velocity field, Fig. 4.2. Linear stability analysis applies at early times because concentration fluctuations are small; it can be shown that the

fastest growing perturbation is characterized by the critical wavelength

$$\lambda_c = 96.23 \frac{\mu\phi D_m}{\Delta\rho g K}, \quad (4.9)$$

which is solely a function of the fluid and aquifer properties, e.g., [75]. This is the smallest perturbation that is not damped by diffusion and emerges from any infinitesimal random perturbation.

At early times, linear instability generates small, local convective cells that are characterized by a width λ_c . When perturbations become larger, the nonlinear regimes starts and fingers grow and merge into larger convective cells, Fig. 4.1 (b). At later times, a fully developed nonlinear fingering regime leads to the formation of complex concentration patterns, Fig. 4.1 (c). From this brief description it is clear that the size of the fingers (or of the convective cells, which are intimately related) is a function of time, $\ell_F(t)$, and is equal to the critical wavelength, λ_c , only in the initially linear regime.

4.4.2 Numerical length scales

To accurately model finger evolution, the problem has to be discretized on a grid that is able to resolve the typical length scales involved in the specific flow regime. In practice, however, problems are discretized on computational grids whose cell size, Δx , is dictated by the information on the geological heterogeneity, by the global flow field, or by computational convenience (i.e., in order to avoid solving global problems that are too large).

At early time, the numerical grid must be able to resolve the critical wavelength, which requires a cell size

$$\Delta x_f = \frac{\lambda_c}{N}, \quad (4.10)$$

where N is the number of cells per wavelength that guarantees the desired accuracy in the description of the instability onset. At later time, the system enters the nonlinear regime and fingers merge. When their size has grown such that

$$\Delta x < \frac{\ell_F}{N}, \quad (4.11)$$

the further evolution of the finger can be described on the original grid. Problems arise due to the fact that in practice $\Upsilon = \Delta x / \Delta x_f \gg 1$, and the fine grid cannot be employed in the whole domain.

An adaptive grid refinement (with cells of size Δx_f used only in the vicinity of the dissolution boundary) will help to limit the computational costs, but the problem size will likely become intractable before the problem can be accurately solved on the original grid. Indeed, this requires $\ell_F > N\Delta x = N\Upsilon\Delta x_f \gg \Delta x_f$ and, therefore, the problems to be solved contain a very large number of fine cells. Fortunately, the limited size of the convective cells might allow solving a set of decoupled problems at early time. These local problems have size Δx_L but discretization characterized by a cell-size Δx_f , which is required to resolve the critical

wavelength.

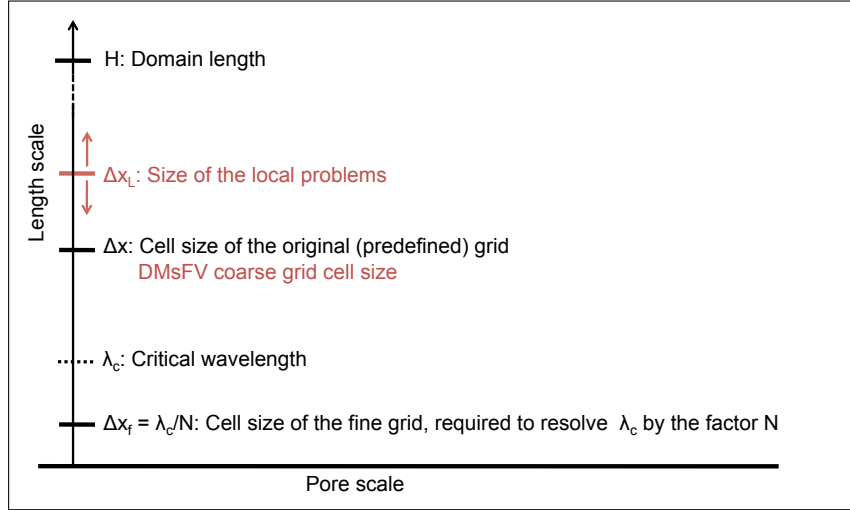


Figure 4.3: Physical and numerical scales in simulating density-driven instabilities.

4.4.3 Onset, transition and global instability stages

The numerical length scales discussed above and illustrated in Fig. 4.3 naturally define three stages: an onset or local stage, in which the evolution of the fingers is local and is not influenced by the original discretization; a global stage, in which the instability is fully developed with respect to the original grid and the problem can be solved with the numerical resolution allowed by the original grid; and a transition stage. The global stage clearly starts at time t_G when the finger can be satisfactorily described by the original grid,

$$\ell_F(t_G) = N\Delta x. \quad (4.12)$$

The onset or local regime ends when the finger have grown such that the localization assumption used to solve problems of size Δx_L becomes inaccurate, i.e., at time t_L such that

$$\ell_F(t_L) > \frac{\Delta x_L}{N_C}, \quad (4.13)$$

where N_C is the number of convective cells that can be accurately simulated in a local problem. This parameter depends on the particular problem, as well as on the localization assumptions used to define the boundary conditions of the local problem, but can also be seen as user-defined parameter that can be tuned to balance accuracy and efficiency.

As Δx_L must contain a reasonable number of fine cells to limit the costs of the local problems, t_L is smaller than t_G and a transition stage exists. One possibility to bridge the gap between the onset and the global stage is to employ a set of nested local problems of increasing size. However, this strategy is not able to take into account the effects of a global flow field,

e.g., a natural gradient present in the porous medium. A better strategy is therefore to employ the DMsFV method, which has proven accurate in dealing with instabilities when multiple interacting scales exist.

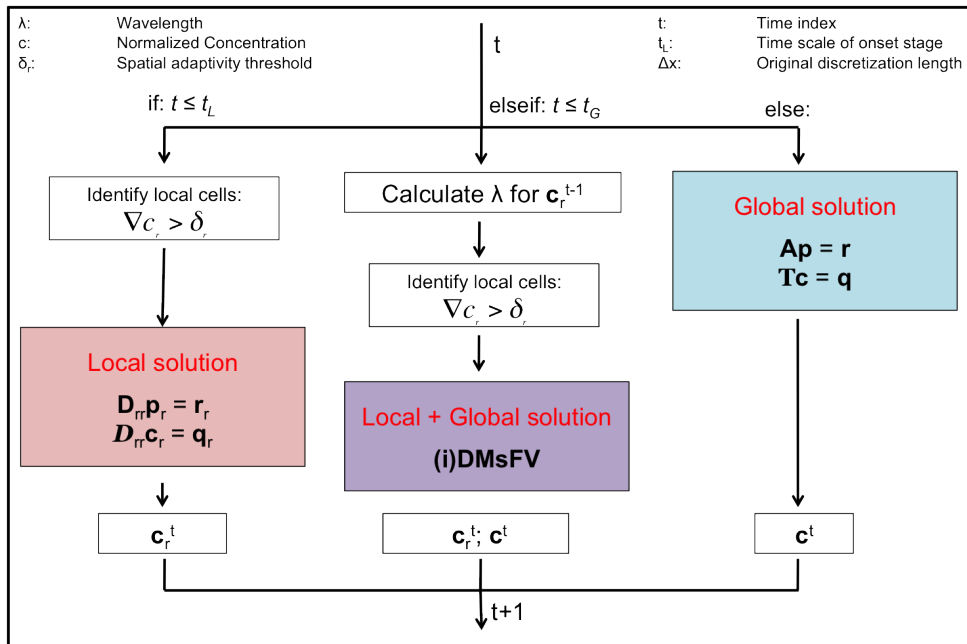


Figure 4.4: Workflow of the new adaptive algorithm (lgDMsFV).

4.4.4 The adaptive algorithm

We employ a new adaptive algorithm (local global DMsFV - lgDMsFV) that makes use of the three characteristic time stages. The flowchart is given in Fig. 4.4. For simulation times $t \leq t_L$ only decoupled refined flow problems of size Δx_L are solved. As larger local problems favour an extended length of t_L , Δx_L might be chosen larger than Δx , providing that local problems can be still solved efficiently. When the simulation time exceeds t_L , the algorithm switches to transition stage and the Downscaling MsFV (DMsFV) method is used to solve the refined flow and transport system. The DMsFV employs the cells of the original problem as coarse cells, which are of size Δx . In the local and in the transition stage local problems are solved adaptively only in cells with relevant refined concentration gradients, i.e.,

$$\nabla c_r > \delta_r, \quad (4.14)$$

where δ_r is an appropriate threshold.

The DMsFV algorithm is applied until Δx resolves the characteristic finger wavelength by the factor N . A 1D Fast Fourier Transformation (FFT) and the resulting power spectrum are used to determine the smallest relevant wavelength. As at later times flow fingers evolve

into complex two-dimensional objects the height function method [10] is used to map the 0.2-contour lines into a 1D object, Fig. 4.5. This enables to estimate the characteristic wavelength at every time step and to identify the transition time. During the global stage, the problem is solved on the coarse grid by a standard finite-volume discretization. Consequently only a coarse concentration field (defined in the same resolution as the original discretization) is obtained after switching to the final stage. The numerical schemes employed in the different stages are described in the next section.

4.5 Numerical formulations of the different stages

4.5.1 Original discretization

We start considering the governing equations, Eqs. (4.1) and (4.3), discretized on the original grid characterized by cell size Δx , which are solved during the global stage. We use a standard finite-volume scheme based on a five-point stencil and on a backward Euler scheme for the time derivative, and we write the equations in discrete form as

$$\mathbf{A}\mathbf{p} = \mathbf{r} \quad (4.15)$$

and

$$\mathbf{T}\mathbf{c} = \mathbf{q}. \quad (4.16)$$

In the equations above, \mathbf{p} and \mathbf{c} are the unknown pressure and concentration vectors at the new time, t , respectively; \mathbf{A} the stiffness matrix, which discretizes the elliptic operator $(\nabla \cdot \frac{k}{\mu} \nabla^*)$; $\mathbf{r} = \mathbf{r}(\mathbf{c})$ the right hand side vector that contains the effects of gravity, $\nabla \cdot \rho(c)\mathbf{g}$, and the boundary conditions; $\mathbf{T} = \mathbf{T}(\mathbf{p})$ the transport matrix that contains the discrete form of the advection operator, $\nabla \cdot (\mathbf{v}^*)$, which depends on the pressure gradient, the discrete form of the diffusion operator, $-\nabla \cdot (\phi D_m \nabla^*)$, and the accumulation operator, $\phi/\Delta t$, where Δt is the time step; and $\mathbf{q} = \mathbf{q}(\mathbf{c}^{t-1})$ is the right hand side vector that contains the effects of boundary conditions and the part of the accumulation operator that depends on the concentration at the previous time $\mathbf{c}^{t-1}/\Delta t$.

Eqs. (4.15) and (4.16) are coupled through \mathbf{r} , which depends on the concentration, and \mathbf{T} which depends on the velocity, thus on \mathbf{p} . The system of equations is solved by a sequentially-implicit scheme: first, the pressure equation is solved using the old concentration; second the resulting pressure, \mathbf{p} , is used to construct the transport matrix, \mathbf{T} ; then, the concentration equation is solved; finally, the new concentration value is used to update \mathbf{r} , and the pressure equation is solved again. This procedure is repeated until convergence, e.g., [36, 45].

4.5.2 Local solution

Resolving the critical wavelength requires a refined grid. To avoid a large number of refined cells we limit the refinement to the regions with large concentration gradients. We indicate the

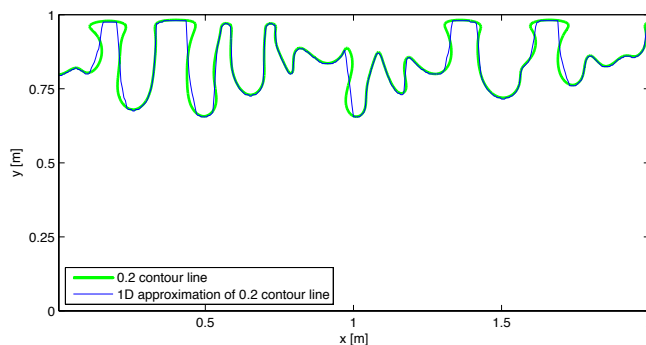


Figure 4.5: 0.2-contour line and its 1D approximation applying a height function method [10] for the dissolution-diffusion-convection problem illustrated in Fig. 4.1 using an extended domain width.

adaptively refined pressure and transport equations by $\mathbf{A}_{\text{rr}}\mathbf{p}_r = \mathbf{r}_r$ and $\mathbf{T}_{\text{rr}}\mathbf{c}_r = \mathbf{q}_r$, respectively. For large domains with corrugated concentration fronts, the refined system cannot be solved directly and we, therefore, consider decoupled local problems of size Δx_L . The decoupled refined flow and transport systems take the form

$$\mathbf{D}_{\text{rr}}\mathbf{p}_r = \mathbf{r}_r, \quad (4.17)$$

and

$$\mathcal{D}_{\text{rr}}\mathbf{c}_r = \mathbf{q}_r, \quad (4.18)$$

where \mathbf{D}_{rr} , resp. \mathcal{D}_{rr} , is the block diagonal version of \mathbf{A}_{rr} , resp. \mathbf{T}_{rr} , if the entries are ordered according to their local cells and the entries corresponding to fluxes across local boundaries have been eliminated. Localization is achieved by assigning zero boundary fluxes (alternatively, periodic boundary conditions could be used). The decoupled refined systems, Eqs. (4.17) and (4.18), are solved by a sequentially-implicit scheme.

4.5.3 DMsFV in transition stage

The DMsFV method is based on the Multiscale Finite-Volume (MsFV) method [36, 57] that was developed to efficiently solve the discretized pressure equation by projecting the problem to a coarser grid and prolongating the coarse solution back to the original discretization. Several extensions of the MsFV method exist that allow, e.g., the accurate simulation of complex flow problems [23, 55, 56, 58, 76] or an adaptive reduction of the computational costs [45, 49]. In contrast to the original upscaling perspective we devised the DMsFV method to be able to adaptively refine dynamic complex flow processes as density-driven instabilities. The DMsFV method will be shortly reviewed in the following. For a more detailed description we refer the readers to [45].

Equally to the previous section, we assume that a fraction of the original grid has been refined, Fig. 4.6, and we write the discrete two-level pressure system as

$$\begin{bmatrix} \mathbf{A}_{rr} & \mathbf{A}_{rc} \\ \mathbf{A}_{cr} & \mathbf{A}_{cc} \end{bmatrix} \begin{bmatrix} \mathbf{p}_r \\ \mathbf{p}_c \end{bmatrix} = \mathbf{A}_D \mathbf{p}_D = \begin{bmatrix} \mathbf{r}_r \\ \mathbf{r}_c \end{bmatrix} = \mathbf{r}_D, \quad (4.19)$$

where $\mathbf{A}_{rc} = \mathbf{A}_{cr}^T$ contains the interactions between refined and non-refined regions and \mathbf{A}_{cc} interactions between non-refined coarse cells. In the DMsFV system, fluxes over non-refined and refined interfaces are calculated by employing the coarse pressure gradient and equally distributed to the fine interfaces, what prevents the problem of hanging nodes.

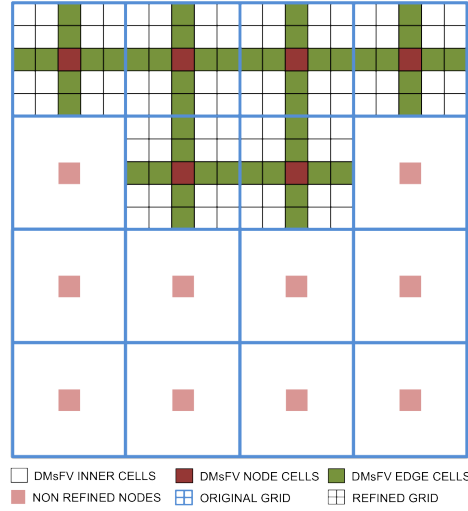


Figure 4.6: DMsFV original grid with adaptively refined cells. In the refined regions the dual grid introduces a partition of downscaled cells into inner, edge and refined node cells according to the MsFV concept.

According to the traditional MsFV concept, the basic idea is to approximate the refined solution on the coarse discretization. We therefore construct a so-called dual coarse grid in the refined regions by connecting the centres of the coarse cells, Fig. 4.6, which allows the classification of refined cells into inner (i), edge (e), and refined node (n) cells, $\mathbf{p}_r = [\mathbf{p}_{r,i} \ \mathbf{p}_{r,e} \ \mathbf{p}_{r,n}]^T$. The pressure vector $\mathbf{p}_n = [\mathbf{p}_{r,n} \ \mathbf{p}_c]^T$ therefore represents the approximate pressure values on the coarse grid.

The dual grid is used to construct local interpolators that allow projecting the refined flow problem to the coarse grid and interpolating the coarse solution, \mathbf{p}_n , back to the refined mesh. Localization is realized by assuming equal transversal fluxes over dual interfaces what is equivalent in eliminating the influence of inner cells on edge cells and of edge on node cells (see Fig. 4.6). This allows rewriting Eq. (4.19) in upper block diagonal form as

$$\begin{bmatrix} \mathbf{A}_{ii} & \mathbf{A}_{ie} & \mathbf{A}_{in} \\ \mathbf{0} & \mathbf{M}_{ee} & \mathbf{A}_{en} \\ \mathbf{0} & \mathbf{0} & \mathbf{M}_{nn} \end{bmatrix} \begin{bmatrix} \mathbf{p}_{r,i} \\ \mathbf{p}_{r,e} \\ \mathbf{p}_n \end{bmatrix} = \begin{bmatrix} \mathbf{r}_{r,i} \\ \mathbf{r}_{r,e} \\ \mathbf{b}_n \end{bmatrix}, \quad (4.20)$$

where neglecting the influence of inner on edge cells ($\mathbf{A}_{ei} = \mathbf{0}$) requires to eliminate the corresponding effects on the main diagonal (we therefore use \mathbf{M}_{ee} instead of \mathbf{A}_{ee}) and where $\mathbf{M}_{nn}\mathbf{p}_n = \mathbf{b}_n$ is the DMSFV coarse problem. Applying a standard backward substitution to Eq. (4.20), the unknown pressure solution in refined and non-refined domains can be written in the form

$$\mathbf{p} \approx \mathbf{B}\mathbf{p}_n + \mathbf{C}\mathbf{r}_D. \quad (4.21)$$

where

$$\mathbf{B} = \begin{bmatrix} \mathbf{A}_{ii}^{-1}(\mathbf{A}_{ie}\mathbf{M}_{ee}^{-1}\mathbf{A}_{en} - \mathbf{A}_{in}) \\ -\mathbf{M}_{ee}^{-1}\mathbf{A}_{en} \\ \mathbf{I}_{nn} \end{bmatrix} \quad \text{and} \quad \mathbf{C} = \begin{bmatrix} \mathbf{A}_{ii}^{-1} & -\mathbf{A}_{ii}^{-1}\mathbf{A}_{ie}\mathbf{M}_{ee}^{-1} & \mathbf{0} \\ \mathbf{0} & \mathbf{M}_{ee}^{-1} & \mathbf{0} \\ \mathbf{0} & \mathbf{0} & \mathbf{0} \end{bmatrix} \quad (4.22)$$

are the basis- and correction-function operators. Using the local interpolators also to project the fine-solution to the original grid, the DMSFV coarse problem is readily given as

$$\chi\mathbf{A}_D\mathbf{B}\mathbf{p}_n = (\chi - \chi\mathbf{A}_D\mathbf{C})\mathbf{r}_D, \quad (4.23)$$

where χ is the summation operator that is equivalent to integrating over coarse cell volumes.

Due to the localization assumption on dual cell boundaries, the (D)MSFV solution is only conservative with respect to the coarse grid. A fully conservative fine-scale velocity field can be constructed by solving once more local flow problems that are defined with respect to the coarse grid and using the approximated DMSFV pressure solution to construct Neumann boundary fluxes,

$$\mathbf{D}_{rr}\mathbf{p}_{r,\text{rec}} = \mathbf{r}_r - (\mathbf{A}_{rr} - \mathbf{D}_{rr})\mathbf{p}_r - \mathbf{A}_{rc}\mathbf{p}_c. \quad (4.24)$$

From the reconstruction procedure a conservative refined velocity field is only available in the downscaled regions. Hence, a two-level formulation has to be applied to the solution of the transport equation,

$$\begin{bmatrix} \mathbf{T}_{rr} & \mathbf{T}_{rc} \\ \mathbf{T}_{cr} & \mathbf{T}_{cc} \end{bmatrix} \begin{bmatrix} \mathbf{c}_r \\ \mathbf{c}_c \end{bmatrix} = \begin{bmatrix} \mathbf{q}_r \\ \mathbf{q}_c \end{bmatrix}. \quad (4.25)$$

Depending on the number of refined cells the direct solution of the downscaled transport system, Eq. (4.25), can become computational expensive and we therefore apply a one-level Schwarz decomposition technique [70], that beside decoupling refined regions from non-refined regions additionally separates the refined coarse cells. Boundary fluxes over decoupled regions are iteratively updated till a predefined threshold, ϵ_{SD} , is matched. The multiscale transport system can be formulated as

$$\begin{bmatrix} \mathbf{D}_{rr} & \mathbf{0} \\ \mathbf{0} & \mathbf{T}_{cc} \end{bmatrix} \begin{bmatrix} \mathbf{c}_r^{\nu+1} \\ \mathbf{c}_c^{\nu+1} \end{bmatrix} = \begin{bmatrix} \mathbf{q}_r - \mathbf{T}_{rc}\mathbf{c}_c^\nu - (\mathbf{T}_{rr} - \mathbf{D}_{rr})\mathbf{c}_r^\nu \\ \mathbf{q}_c - \mathbf{T}_{cr}\mathbf{c}_r^\nu \end{bmatrix}, \quad (4.26)$$

where ν is the index of iteration.

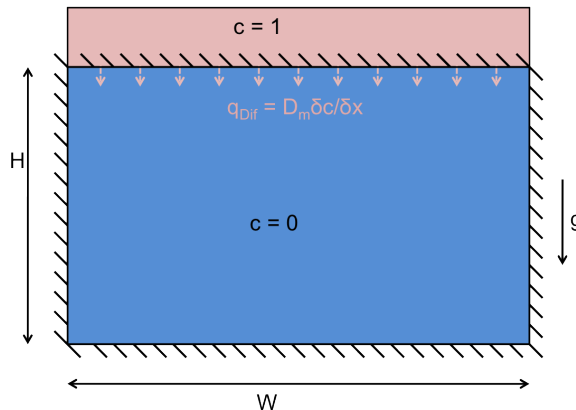


Figure 4.7: Initial set-up dissolution-diffusion-convection problem [20, 63, 65] during CO₂ storage in saline aquifers. c refers to the normalized CO₂ concentration and q_{Dif} to the diffusive inflow. Convection is initiated by assigning a randomly perturbed concentration layer to the top of the domain.

Due to the localization assumption on dual cell boundaries, the DMsFV pressure solution is an approximation to the fine-scale solution. Especially in case of complex flow problems the solution can differ significantly. To improve the quality of the pressure solution several adaptive strategies have been proposed that iteratively add the neglected fluxes on dual boundaries [23, 58]. According to [58], we use the DMsFV operators as two-stage preconditioner \mathbf{P}^{-1} in the following iterative scheme,

$$\mathbf{p}^{\nu+1} = \mathbf{p}^{\nu} + \omega^{\nu} \mathbf{P}^{-1}(\mathbf{r} - \mathbf{A}\mathbf{p}^{\nu}). \quad (4.27)$$

The index ν again denotes the iteration level and ω^{ν} is a relaxation parameter, calculated with the Generalized Minimal Residual method (GMRES [67]).

4.6 Numerical simulations

4.6.1 Problem definition and reference solutions

We test the performance of the adaptive algorithm with the dissolution-diffusion-convection (DDC) problem. We consider a domain of width $W = 6$ m, which is chosen to minimize the influence of boundary conditions and to obtain a sufficiently large number of fingers. All boundaries are impermeable to fluid flow. While a solute can diffuse into the domain at the top boundary, where a normalized concentration $c = 1$ is assigned, no mass exchange occurs through the other three boundaries (Fig. 4.7). In order to trigger the instability, random initial concentration values are assigned in the first cells next to the diffusive-inflow boundary (the same random perturbation is used for different algorithms). To guarantee a satisfactory

resolution of the density fingers at late times (see, e.g., Fig. 4.1 (c)), we employ an original grid that consists of 240 x 80 cells, which corresponds to a discretization length of $\Delta x = 2.5 \cdot 10^{-2}$ m. Fluid and aquifer properties used in the simulations are defined according to [63] and are given in Table 4.1.

Table 4.1: Fluid and model parameters for the dissolution-diffusion-convection problem during CO₂ storage in saline aquifers.

Parameter	Size	Unit	Parameter	Size	Unit
$\rho(c = 0)$	995	kg/m^3	$\Delta\rho$	10	kg/m^3
\mathbf{k}	$1.0 \cdot 10^{-11}$	m^2	μ	$1.0 \cdot 10^{-3}$	$kg/m/s$
D_m	$2 \cdot 10^{-9}$	m^2/s	ϕ	$3.0 \cdot 10^{-1}$	[–]
H	2	m	W	6	m
Δt^*	$2.7 \cdot 10^{-7}$	[–]	t_{end}^*	$7.425 \cdot 10^{-4}$	m/s^2
ϵ_{pC}	$1.0 \cdot 10^{-4}$	[–]	δ_r	0.1	[m]
ϵ_{SD}	$1.0 \cdot 10^{-4}$	[–]	ϵ_{GMRES}	$0.5 \cdot 10^{-6}$	[–]
Δx	$2.5 \cdot 10^{-2}$	[m]	Δx_f	$5 \cdot 10^{-3}$	[m]
Δx_L	$5 \cdot 10^{-1}$	[m]	g	9.81	[m/s^2]

For the given flow parameters, the critical wavelength that has to be resolved is $\lambda_c = 0.059$ m. A grid convergence study for the DDC problem [63], has shown that the onset-time error determined by the CO₂ mass influx at the diffusive boundary is about 1 % for $N = 100$, and increases to around 10 % and 12 % for $N = 25$ and $N = 10$, respectively. For numerical convenience, we take $N = 11.8$, which still guarantees a quite accurate reference solution, and corresponds to a fine grid consisting of 1200 x 400 cells of size $\Delta x_f = \lambda_c/11.8$. The numerical diffusion coefficient arising from truncation errors has been estimated from the numerically computed velocity field and is one order of magnitude smaller than the assigned molecular diffusion coefficient.

The reference solution is computed with the flow and transport software MaFloT (Matlab Flow and Transport - [47]), which is based on a standard 5-point-stencil finite-volume discretization. The reference concentration field at the dimensional time $t_{end}^* = 7.425 \cdot 10^{-4}$ is shown in Fig. 4.8 (a), together with its 0.2-contour line, and corresponds to the final simulation time investigated in this work. Accumulation of solute at the bottom boundary is therefore not considered since we are interested in the unstable flow regime. The reference refined concentration plot shows about 15 fingers of length 0.5 m or longer. The tip of the most penetrating finger (defined from the 0.2-contour line) is located about 0.2 m above the bottom boundary. Fig. 4.8 (b), shows the concentration field computed directly on the original grid. The coarse solution captures neither the fine-scale penetration depth (the tip of the most penetrating finger is located about 0.7 m above the bottom boundary) nor the total mass in the system, which is underestimated by 35 %. This demonstrates the importance of correctly resolving the characteristic length of the perturbation and highlights the needs of resolving the fine-scale details of

the instability at early times in order to capture the coarse-scale flow behaviour at later times.

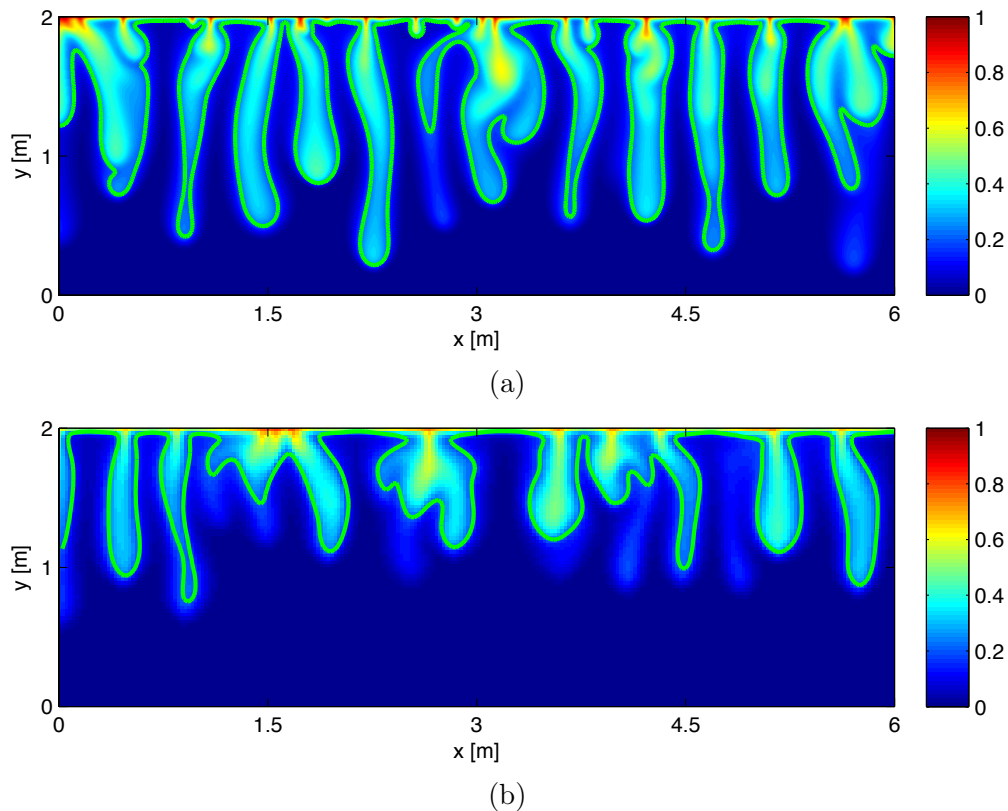


Figure 4.8: (a) Reference normalized concentration field at $t_{end}^* = 7.425 \cdot 10^{-4}$ computed with respect to the fine discretization using the finite-volume function MaFloT [47]. (b) Normalized concentration field computed with respect to the coarse grid at $t_{end}^* = 7.425 \cdot 10^{-4}$. The corresponding 0.2-contour lines are shown in green.

4.6.2 Adaptive simulations

We evaluate the adaptive algorithm in three separate steps: first, we investigate the error caused by the localization of the onset stage; then, we focus on the effects of the global-stage coarsening; finally, we evaluate the performance of the complete algorithm (onset-transition-global stages) and its ability to predict the response of an ensemble of initial random perturbations. The transition stage is not investigated separately and its effects are studied only in relation to the complete algorithm, because we have previously demonstrated that the DMsFV provides an arbitrary accurate solution if a low convergence threshold is used in the GMRES iterations [45].

As small differences grow with time in unstable flow regimes, we evaluate the error of the components of the adaptive algorithm by comparing the concentration field with the reference solution at the final simulation time t_{end}^* . In this manner, small errors can develop with time and we can assess whether the reference concentration is accurately reproduced in a deterministic or statistic sense. When studying the onset stage, localized problems are solved for $t^* < t_L^*$,

whereas the fully refined reference algorithm is employed for $t^* > t_L^*$ in order to isolate the errors arising from the onset stage only. Analogously, to identify the effects of the global-stage coarsening, the reference algorithm is used before switching to the coarse discretization at time $t^* < t_G^*$.

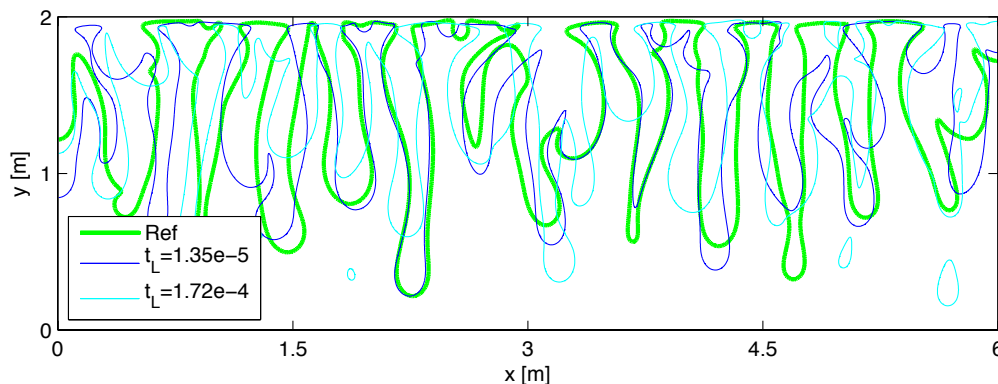


Figure 4.9: 0.2-contour lines at $t_{end}^* = 7.425 \cdot 10^{-4}$ obtained with different lengths of the local stage in comparison to the reference fine-scale solution.

4.6.2.1 Error introduced by the onset stage

In the local stage, problems solved on subdomains of size Δx_L in contact with the diffusive top boundary are decoupled by imposing zero-flux conditions in the other three boundaries. In general, the quality of the approximate solution obtained by this procedure depends on Δx_L as well as on the duration of the local stage t_L^* , which are closely related. In the following simulations, we fix $\Delta x_L = 100\Delta x_f \approx 10\lambda_c$ and evaluate the error for different durations of the onset stage.

In Fig. 4.9, the 0.2-contour lines obtained with two different durations of the onset stage ($t_L^* = 1.35 \cdot 10^{-5}$ and $t_L^* = 1.72 \cdot 10^{-4}$) are compared to the 0.2-contour line of the reference solution at $t_{end}^* = 7.425 \cdot 10^{-4}$. For the longer duration, $t_L^* = 1.72 \cdot 10^{-4}$, the most penetrating finger is close to the no-flow bottom boundary of the local cell when the onset stage ends. The effects of the localization are well visible. Fingers evolve differently (in a deterministic sense) due to small differences at the end of the onset stage which increase with time. In general, the longest the onset time, the most different the concentration distribution looks at the end of the simulation. This is confirmed by the L1-norm of the concentration error illustrated in Fig. 4.10 (a): errors increase with t_L^* and, for short onset times, are about 30 % smaller than the error of the coarse solution. For the shortest t_L^* in Fig. 4.10, the onset stage is 2.3 % of the total simulation time, whereas it takes about 23 % of the total time for the longest t_L^* .

For unstable flow regime, rather than the deterministic reproduction it is important to evaluate overall characteristics of the concentration patterns. Therefore, we consider the total

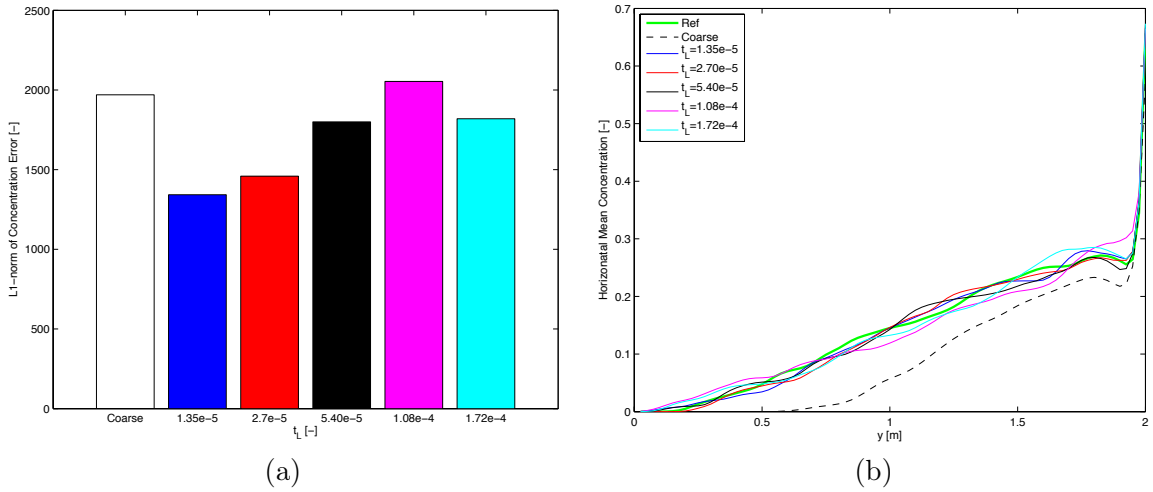


Figure 4.10: (a) L-1 norm of the concentration error for different t_L in comparison to the coarse solution at $t_{end}^* = 7.425 \cdot 10^{-4}$. (b) Vertical profile of the horizontal-average concentration for different t_L in comparison to the reference and coarse solution at $t_{end}^* = 7.425 \cdot 10^{-4}$.

mass influx into the domain and the vertical profile of the mean concentration (averaged horizontally). The total solute mass in the domain is at most 3% larger than the reference value for all t_L^* ; also the vertical concentration profiles are sufficiently well captured for all durations of the onset stage (Fig. 4.10 (b)). A more careful look reveals moderately better reproduction of the reference penetration and the vertically transported mass for depths lower 0.5 m for $t_L^* < 1.08 \cdot 10^{-4}$, but differences are limited. Notice that when the problem is solved directly on the coarse grid without refinement the results are inaccurate: mass influx is underestimated by about 35%, and the vertical profile is not satisfactorily captured.

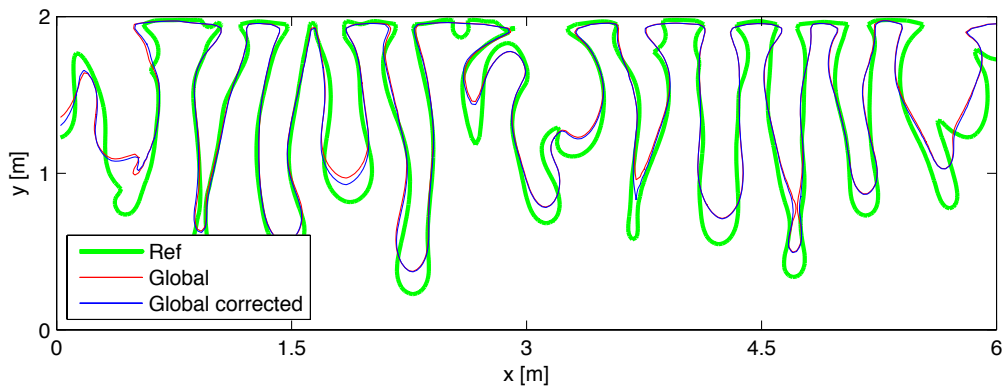


Figure 4.11: 0.2-contour lines at $t_{end}^* = 7.425 \cdot 10^{-4}$ obtained by applying a coarse description when the characteristic finger width counted $10\Delta x$. The reference fine-scale code was applied before the global stage.

Additional simulations with smaller sizes of the local Ref problem (not presented here) confirmed

the results above, but with larger errors: for the same t_L^* , the error was about twice as large if $\Delta x = 50\Delta x_f$ was used. Since longer durations of the onset stage are computationally less expensive, in practical applications the value of t_L^* can be chosen to balance accuracy and efficiency.

4.6.2.2 Effects of global stage

In accordance with the value chosen to define the fine-scale grid ($N \approx 10$) the local stage starts at time t_G^* such that the finger width is $\ell(t_G^*) = 10\Delta x$. To estimate the finger width we make use of height functions and FFT as described in Chapter 4.4.4. Again, to isolate the error introduced by the global stage, the reference finite-volume code is used before switching to the global stage ($t^* < t_G^*$). The resulting 0.2-contour line is compared to the reference fine-scale solution in Fig. 4.11. The time of transition to the global stage is $t_G^* = 3.9312 \cdot 10^{-4}$, which represents 47% of the total simulation time. The red contour line refers to a straightforward coarsening procedure.

Whereas shape and number of fingers are well reproduced, a shallower penetration is observed. This can also be seen from the vertical concentration profile (Fig. 4.12 (b)) and is caused by a lower mass influx that leads to underestimate the total mass by about 7% at the end of the simulation (Fig. 4.12 (a)). The origin of the reduced influx is the poor resolution of the coarse grid that does not allow to resolve the nonlinear concentration profile in the diffusive boundary layer at the top boundary and leads to a systematically smaller concentration gradient.

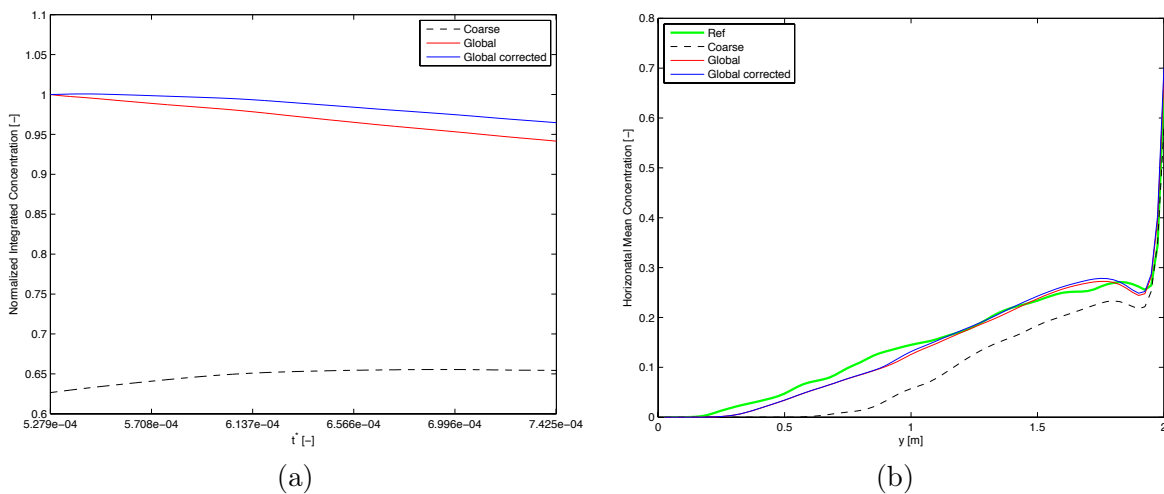


Figure 4.12: (a) By the reference mass normalized total mass evolution for the coarse, the non-corrected and the corrected global simulations. (b) Vertical profile of the horizontal-average concentration at $t_{end}^* = 7.425 \cdot 10^{-4}$.

To avoid large errors in mass without changing the resolution of the grid close to the upper boundary, we introduce a Cauchy-type correction of the diffusive boundary conditions. The

basic idea is to estimate the diffusive-flux error for each coarse cell i during the transition stage when it can be easily calculated as the ratio between the fine-scale boundary fluxes and the boundary flux that would be generated by the coarse gradient, i.e.,

$$\epsilon_{D,i}(t) = \frac{\sum_j \frac{\Delta x_f (1 - c_{f,i}(t))}{\Delta x_f / 2}}{\frac{\Delta x (1 - c_i(t))}{\Delta x / 2}}, \quad (4.28)$$

where $1 - c_i$ is the difference between the concentration at the top boundary and the concentration in the center of the coarse cell; $1 - c_f(j)$ the difference between the concentration in the center of the fine cell j adjacent to the top boundary and located in the coarse cell i ; and the sum is taken over all fine cells j located in the coarse cell i . As the concentration difference can vary in time, the correction is computed as the average influx error over a time interval Δt ,

$$\epsilon_{D,i} = \frac{1}{\Delta t} \int_{t_G - \Delta t}^{t_G} \epsilon_{D,i}(t) dt, \quad (4.29)$$

and the boundary condition is

$$q_{D,i}(t) = \epsilon_{D,i} D_m \Delta x \frac{(1 - c_i(t))}{\Delta x / 2}, \quad (4.30)$$

which is equivalent to a Cauchy type boundary condition with a corrected diffusion coefficient $\epsilon_{D,i} D_m$.

In the numerical simulations, we consider the last 20 time steps before transition to the global stage to estimate $\epsilon_{D,i}$. The results with the corrected diffusive boundary influx are shown in blue in Fig. 4.11 and Fig. 4.12. The contour line and vertical concentration are insignificantly improved. The latter shows a slight increase of the mass contained in the upper cells of the domain. Better results can be observed for the total mass evolution where the error in mass at t_{end}^* could be reduced by about 40 %. Notice that in case of extended simulation times or for more complex flow problems, the DMsFV algorithm could be alternatively applied during global stage in the coarse cells adjacent to the diffusive boundary.

4.6.2.3 Statistical accuracy of the adaptive algorithm

To evaluate the variability of the solution due to the initial random perturbation and to statistically assess the performance of the algorithm, we consider an ensemble of 20 initial random perturbations. The results obtained by the reference code are shown in Fig. 4.13, which plots the vertical concentration profile and the total mass as a function of time for each realization, together with the ensemble average and the standard deviation.

To decrease the influence of transition stage on simulation results, the iterative extension of DMsFV is used with a GMRES convergence threshold of $5 \cdot 10^{-7}$, which guarantees a solution almost as accurate as the reference for the transition stage. Due to the different initial random perturbations that impact finger evolution, change from transition to global stage took place

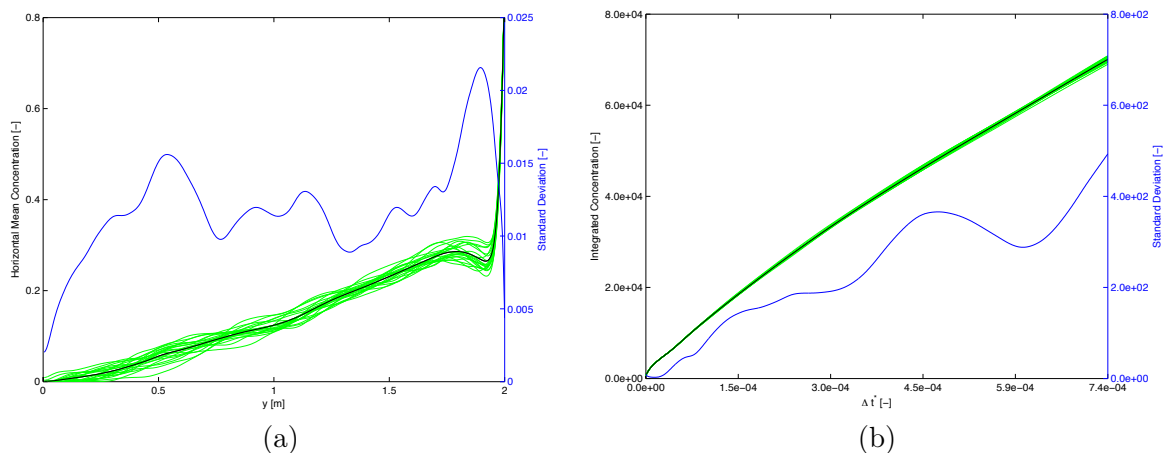


Figure 4.13: (a) Ensemble horizontally integrated normalized concentration profiles. (b) Ensemble total mass evolutions for the reference algorithm. The corresponding mean to the ensemble is shown in black and the standard deviation in percent of the mean value is shown in blue.

at different simulation times, which ranged from $t_G^* \approx 3 \cdot 10^{-4}$ to $t_G^* \approx 6 \cdot 10^{-4}$. The average duration of the global stage was about 40 % of total time. For simulations at which t_L was determined when the fastest finger reaches the bottom of the local cell, the average duration of the onset stage was 24.6 % of the total simulation time, which corresponds to $t_L^* = 1.826 \cdot 10^{-4}$.

The L1-norm of the errors of the ensemble-average concentration are displayed in Fig. 4.14 (a) for all t_L^* values. They are half the size of the error of the coarse solution that was obtained without refinement. Differences among simulations with different t_L^* values are minor and no clear trend can be observed. This shows that, despite the fact that for each perturbation the finger evolution differs from the reference solution, the variability from realization to realization is larger and the error introduced by the adaptive algorithm is mostly random and not systematic. Also, the good results obtained for all t_L^* are a consequence of the relatively large ratio of local-cell size to the original-cell size, $\Delta x_L / \Delta x = 20$, which allows an evolution of local instabilities that is not affected by the localization assumption.

The vertical profiles of the ensemble-average concentration show little dependency on t_L^* . All onset-stage durations yield results in very good agreement with the reference (Fig. 4.14 (b)), and a small mismatch is visible only for concentrations lower than 0.1; in contrast, the coarse solution systematically leads to much shallower penetrations and to an inaccurate vertical profile of the ensemble-average concentrations. As a consequence, the error of the total mass influx is about 35 % for the coarse solution, but less than 2 % for the adaptive algorithm.

In Fig. 4.15 the 10th and 90th percentiles of the references solution are compared with those of the coarse solution as well as of the solutions of the adaptive algorithm. The fluctuations of the total mass influx at the end of the simulation are similar to the one of the reference solution for the adaptive algorithm, which demonstrates the very accurate reproduction of the concentration evolution in a statistic sense (Fig. 4.15 (a)). Also the 10th percentile of the vertical

concentration profile concentration is very well reproduced by the adaptive algorithm (for the sake of clarity, the vertical profile for only two values of t_L is shown in Fig. 4.15 (b)). Larger differences can be observed for the 90th percentile, which refers to a depth where concentrations of less than 0.1 are present.

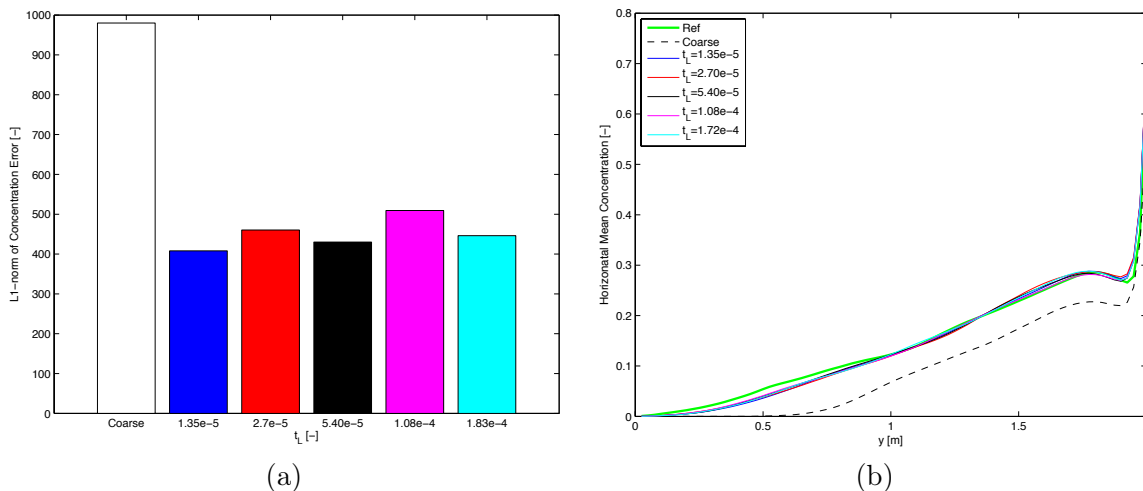


Figure 4.14: (a) L-1 norm of the concentration error for different t_L in comparison to the coarse solution at $t_{end}^* = 7.425 \cdot 10^{-4}$. (b) Vertical profiles of the horizontal-average concentration for different t_L in comparison to the reference and coarse solution at $t_{end}^* = 7.425 \cdot 10^{-4}$. All results are obtained by the ensemble average.

4.7 Conclusions

We have introduced an adaptive algorithm that splits the simulation of density-driven instabilities into three stages: an onset stage, during which the diffusion scale has to be locally resolved to correctly model the instability onset; a transition stage, in which spatiotemporal scales closely interact and the DMsFV algorithm is used to link local and global scales; and a global stage that is characterized by fully developed fingers, which can be described directly by the original coarse discretization and which allow neglecting the fine-scale details of the flow.

Considering the dissolution-diffusion-convection problem, we have tested the adaptive algorithm for different durations of the onset stage. Small random errors are introduced by the onset stage, but mass influx can be systematically underestimated during the global stage if the nonlinear concentration profile close to the diffusive boundary is not captured by the coarse discretization. To reduce this effect we have introduced a correction that accounts for the difference between fine- and coarse-scale gradients at the boundary. The corrected boundary condition improves the influx estimate and reduces the mass error by a half. As an alternative to the correction, a fine-scale resolution in the cells adjacent to the top boundary could be maintained during the global stage by applying the DMsFV algorithm to resolve the diffusive

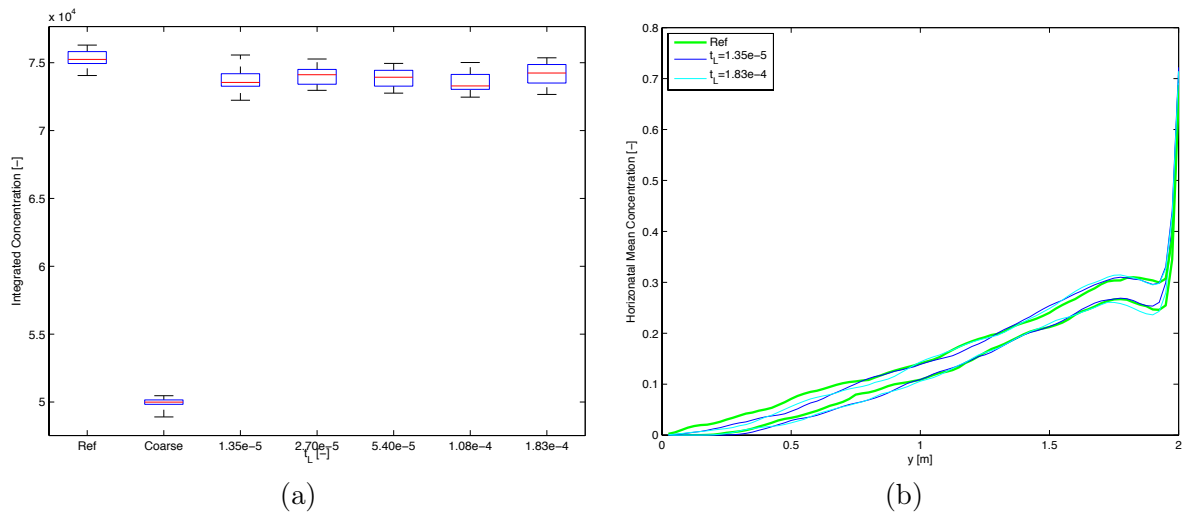


Figure 4.15: (a) The upper and lower limit of the blue boxes refer to the 90th and 10th percentile of the total mass. The black bars illustrate the minimum and maximum values and the median is highlighted in red. (b) 90th and 10th percentile profiles for the horizontal-average concentration. Simulation results refer to $t_{end}^* = 7.425 \cdot 10^{-4}$.

boundary layer; this is expected to provide better results, but might require smaller time steps at least for the refined problems.

In addition to a deterministic analysis of the evolution of a single perturbation, we have performed a statistical analysis by simulating the evolution of density fingers for an ensemble of initial perturbations. Indeed, in practical problems, flow instabilities can be evaluated solely in a statistical sense because initial perturbations are unknown due to their intrinsic random nature and to the impossibility of accurately characterizing finger evolution at very early times. Our numerical simulations demonstrate that for all durations of the local stage, an excellent reproduction of the ensemble-average behaviour of finger evolution is achieved. The small effects of onset-stage duration on the accuracy of the predicted ensemble-average behaviour are due to the relatively large ratio between the size of the local problems, Δx_L , and the coarse-cell size, Δx . For smaller ratios, which will be typically encountered in real applications due to the larger disparities of scales involved, the quality of the adaptive-algorithm solution is expected to deteriorate for larger t_L^* and shorter onset stages should be used to achieve the same accuracy. Notice that solutions obtained directly on the coarse grid are unable to correctly model the problem in a deterministic and even in a statistical sense: a systematic underestimation of total mass influx and penetration depth can be observed. This confirms the paramount importance of resolving the fine-scale details of the flow at early time.

The computational efficiency achieved by the adaptive algorithm with respect to iterative DMsFV relies on the fully local formulation used in the onset stage, as well as on the fully coarsened problem at later times (global stage). Additional strategies can be envisaged to further reduce the computational costs. The iterative DMsFV algorithm used in the transition

stage delivers an almost exact solution by using a low convergence threshold. This level of accuracy is probably unnecessary to capture the statistical behaviour of the fingers and similar results might be obtained without iterations (i.e., using a simple DMsFV algorithm in the transition stage). Also, errors might be dominated by the localization in the onset stage and further inaccuracies introduced in the transition stage might indeed have a minor impact on the overall quality of the solution. To limit the size of the largest problem to be solved, which can become large in practical applications, the recently developed multilevel MsFV concept [46] might be used to offer additional flexibility to balance accuracy and efficiency.

The good results obtained for all onset-stage durations might give the impression that a transition stage is not needed and that it is possible to switch from the onset to the global stage directly. However, this would require local problems that are unrealistically large for practical problems when Δx is typically much larger than Δx_f . Also, in presence of preexisting spatial variability, such as natural flow gradients or heterogeneity, it might be necessary to use global information to define the boundary conditions of the local problems. This suggests that a natural evolution of the solution strategy presented here, is the use of a DMsFV algorithm that solves the global and the local problem with different time steps. This would allow combining the advantages inherent to the onset stage (solution of local time-dependent problems) with the accuracy provided by the solution of a global problem in the transition stage.

Acknowledgments

This project is supported by the Swiss National Science Foundation grants FNS PP00P2_123419 and PP00P2_144922.

Chapter 5

Conclusions and outlook

5.1 Conclusions

The following objectives were to be addressed in this work:

- Investigate the effects of the approximations in MsFV on density-driven instabilities and apply adaptive strategies to balance the additional costs of the iterative extension that is necessary to reproduce fine-scale results.
- Develop an efficient downscaling technique that is based on the MsFV concept and that allows to locally resolve the scales of interest.
- Extend the MsFV concept to more than one level of coarsening, which is necessary to keep the method efficient for very large problems in future applications.
- Investigate the level of local and global information required to reproduce density-driven instabilities in a statistical prospective.

While the first three objectives aim at developing numerical tools to simulate density-driven instabilities, the last one addresses the question of how accurately physical processes have to be described on the refined discretization and if a coarsening is possible at late times.

Concerning more technical objectives, the Multiscale Finite-Volume (MsFV) method has been tested and extended to deal with density-driven instabilities. First we focused on the efficiency of the method. Adaptive schemes were applied to the MsFV pressure and transport system in order to restrict the velocity reconstruction to coarse cells that contain the moving front and to iteratively improve the initial pressure solution only where the flow is unstable. We demonstrated that for moderate spatial adaptivity thresholds, the additional costs of the iterations are balanced by adaptivity and that accurate results can be produced.

In the second part of Chapter 2, a modification of the Multiscale Finite-Volume method from an upscaling-downscaling method into a downscaling method was introduced. Downscaling is important to resolve fine-scale processes in presence of flow instabilities. In comparison with other methods the downscaling MsFV (DMsFV) offers two advantages: first, the problem of

hanging nodes is avoided by calculating the fluxes over refined and non-refined interfaces on the coarsest discretization and equally distributing the fluxes to the fine interfaces; second, the largest flow problem to be solved is limited by the size of the coarse problem. Errors introduced by the localization assumption on refined dual boundaries are controlled by local iterative updates in DMsFV.

While the traditional (adaptive) MsFV method provides an efficient solution for a given fine-scale discretization, the downscaling MsFV was designed to increase accuracy by means of a dynamic and local refinement down to the diffusion scale. A grid convergence study for the saline Elder problem [17] with the DMsFV algorithm provided new insight to the reappearance of downwelling flow at very fine discretizations.

A new n -level extension of the MsFV method that serves the adaptive as well as the downscaling concept and allows keeping the traditional method efficient for future applications with an increasing number of unknowns, has been introduced in Chapter 3. In this case, new insights into the algorithm were obtained by a detailed complexity analysis, which showed that only for small upscaling factors the MsFV coarse problem is the computational bottleneck. This demonstrates the importance of adaptive formulations applied to the local operators and the reconstruction procedure as well as the need of an n -level formulation that helps reducing the computational costs.

Simulation results demonstrated that the nested multilevel reconstruction, which avoids solving large problems in the reconstruction step, performs very well in terms of accuracy and computational cost. However, localization assumptions in case of an underlying 9-point stencil discretization in 2D (or a 27-point stencil in 3D) lead to large errors in the multilevel pressure solution, which require a large number of iterations to be eliminated. To guarantee efficient and accurate simulations, additional strategies such as using a Block-Incomplete LU (BILU) smoother or reintroducing connections that have been neglected due to the localization assumption have been proposed. The latter is computationally inexpensive if it is done on the coarsest level.

With respect to the last objective of this thesis (see above), previous work demonstrated that an accurate description of density-fingers requires the flow and aquifer properties to be known and the numerical scheme to be able to resolve the fastest growing wavelength. Relationships for the critical wavelength have been derived on the basis of a linear stability analysis by different authors, e.g., [66, 75]. From the critical wavelength the characteristic size of the fingers continuously grows, as single perturbations merge with time. Based on this observations, in Chapter 4 we classified finger evolution into three characteristic stages: the onset, the transition and the global stage. In the onset stage fingers are local but the diffusion scale needs to be resolved. In the transition stage, the single perturbations start to interact and a global problem needs to be considered to describe the interactions among the local problems. The DMsFV method enables resolving these interactions. In the global stage the characteristic length is large and a coarse description is sufficient.

These different stages entail the use of different numerical schemes. The onset stage is solved by decoupling the flow problem into a set of local problems with zero boundary fluxes. The DMsFV method is employed in the transition stage. In the final stage the problem can be coarsened since local fluctuations of the concentration become negligible. The adaptive local and global formulation (lgDMSFV) is an extension of the downscaling algorithm. Statistically meaningful coarse results (with respect to horizontally averaged concentration profiles and mass content) for the dissolution-diffusion-convection problem were obtained also for long durations of the local stage. This demonstrates that a coarsening of instabilities at late times is possible, if the diffusive scale is resolved at initial times. Furthermore, localization errors are of the order of the variations obtained by 20 realizations of the randomly perturbed initial concentration layer.

5.2 Outlook

With the new extensions, the MsFV method is an efficient tool to simulate flow and transport problems with dynamically changing scales. In Chapter 2 and Chapter 3 simulation results were mostly evaluated in a deterministic sense or at most in terms of horizontally averaged concentration profiles. In practice, the uncertainty on the input data, i.e., in permeability and porosity models, and on the initial conditions prevents a deterministic reproduction of the flow fingers. Future simulation of density-driven instabilities should therefore use DMsFV or lgDMsFV formulations in a statistical framework. A large number of approximated but relatively inexpensive realizations can be simulated as in [40] and compared to ensemble average quantities as in Chapter 4. Statistical evaluations may allow relaxing the adaptivity threshold as a highly accurate solution may not be necessary. Notice that adaptive algorithms offer multiple degrees of freedom in form of thresholds that have to be defined by end users. The question of the level of accuracy or efficiency has always to be answered with respect to the objectives of the application.

Even if this work focused on the Multiscale Finite-Volume method as adaptive downscaling technique to simulate density-driven flow in porous media, a novel n -level formulation was developed and tested as preconditioner in an iterative scheme. The efficiency of the n -level algorithm has been compared to the two-level algorithm by a detailed complexity analysis. Future works could validate the results obtained from the complexity analysis by comparing CPU times of the specific implementations. This would require recoding the MATLAB prototype code used in this work in a higher-level programming language that allows for full compilation. In the framework of reliable efficiency tests the question of the best performing smoother in conjunction with multiscale and multilevel operators as well as a comparison between multiscale or multilevel formulations and an optimal performing Multigrid solver could be addressed.

Advantages of a downscaling MsFV algorithm have been pointed out in Chapter 2. Additional numerical comparisons to existing downscaling algorithms could include the n -level concept into DMsFV. Here the performance of MMsFV in case of an inhomogeneous pressure

equation, which is the result of gravity effects can be investigated. Also improved boundary conditions for local problems might be devised in future works to reduce the number of iterations with and without manipulation of the traditional correction function smoother. Finally, with respect to the lgDMsFV method, the idea of moving local problems in case of external pressure gradients could be realized.

Bibliography

- [1] J. E. Aarnes. On the use of a mixed multiscale finite element method for greater flexibility and increased speed or improved accuracy in reservoir simulation. *Multiscale Modeling and Simulation*, 2(3):421-439, 2004.
- [2] E. Abarca, J. Carrera, X. Sánchez-Vila, and M. Dentz. Anisotropic dispersive Henry problem. *Advances in Water Resources*, 30(4):913–926, 2007.
- [3] G. Arfken, and H. J. Weber. *Mathematical Methods for Physicists*. Fourth Edition, Academic Press San Diego, USA, 1995.
- [4] P. Bastian. *Numerical Computation of Multiphase Flows in Porous Media*. Habilitation Thesis, Christian-Albrechts-Universität Kiel, Germany, 1999.
- [5] J. Bear. *Dynamics of Fluids in Porous Media*. American Elsevier Publishing Company, New York, USA, 1972.
- [6] S. H. Begg, R.R. Carter, and P. Dranfield. Assigning effective values to simulator gridblock parameters for heterogeneous reservoirs. *SPE Reservoir Engineering*, 4(4):455–463, 1989.
- [7] G. Bonfigli, and P. Jenny. An efficient multi-scale Poisson solver for the incompressible Navier–Stokes equations with immersed boundaries. *Journal of Computational Physics*, 228(12):4568–4587, 2009.
- [8] Z. Chen, and T. Y. Hou. A mixed multiscale finite element method for elliptic problems with oscillating coefficients. *Mathematics of Computation*, 72:541–576, 2003.
- [9] M. A. Christie, and M. J. Blunt. Tenth SPE comparative solution project: a comparison of upscaling techniques. *SPE 66599, presented at the SPE Symposium of Reservoir simulations*, Houston, USA, February 2001.
- [10] S. J. Cummins, M. M. Francois, D. B. Kothe. Estimating curvature from volume fractions. *Computers and Structures*, 83:425–434, 2005.
- [11] M. O. Deville, P. F. Fischer, and E. H. Mund. *High-Order Methods for Incompressible Fluid Flow*. Cambridge University Press, Cambridge, UK, 2002.

- [12] H.-J.G. Diersch, and O. Kolditz. Coupled groundwater flow and transport: 2. Thermohaline and 3D convection systems. *Advances in Water Resources*, 21(5):401–425, 1998.
- [13] H.-J.G. Dirsch, and O. Kolditz. Variable-density flow and transport in porous media: approaches and challenges. *Advances in Water Resources*, 25(8–12):899–944, 2002.
- [14] C. Doughty, and K. Pruess. Modeling supercritical carbon dioxide injection in heterogeneous porous media. *Vadose Zone Journal*, 3(3):837–847, 2004.
- [15] Y. R. Efendiev. The Multiscale Finite Element Method (MsFEM) and its Applications. Dissertation (Ph.D.), California Institute of Technology, USA, 1999.
- [16] J. W. Elder. Steady free convection in a porous medium heated from below. *Journal of Fluid Mechanics*, 27:29–48, 1967.
- [17] J. W. Elder. Transient convection in a porous medium. *Journal of Fluid Mechanics*, 32(1):69–96, 1967.
- [18] J. Ennis-King, and L. Paterson. Rate of dissolution due to convective mixing in the underground storage of carbon dioxide. In J. Gale and Y. Kaya (Eds.) *Greenhouse Gas Control Technologies*, 1:507–510, 2003.
- [19] J. Ennis-King, and L. Paterson. Role of convective mixing in the long-term storage of carbon dioxide in deep saline formations. *SPE 84344, presented at the SPE Annual Technical Conference and Exhibition*, Denver, 2003.
- [20] R. Farajzadeh, H. Salimi, P. L.J. Zitha, and H. Bruining. Numerical simulation of density-driven natural convection in porous media with application for CO₂ injection projects. *International Journal of Heat and Mass Transfer*, 50(25-26):5054–5064, 2007.
- [21] P. Frolkovic, and H. De Schepper. Numerical modelling of convection dominated transport coupled with density driven flow in porous media. *Advances in Water Resources*, 24(1):63–72, 2001.
- [22] R. J. Glass, T. S. Steenhuis, and J-Y. Parlange. Mechanism for finger persistence in homogeneous unsaturated porous media: theory and verification. *Soil Science*, 148(1):60–70, 1989.
- [23] H. Hajibeygi, G. Bonfigli, M. A. Hesse, and P. Jenny. Iterative Multiscale Finite-Volume method. *Journal of Computational Physics*, 227(19):8604–8621, 2008.
- [24] H. Hajibeygi, S. H. Lee, and I. Lunati. Accurate and efficient simulation of multiphase flow in a heterogeneous reservoir with error estimate and control in the Multiscale Finite-Volume framework. *SPE 141954-PP, presented at SPE Reservoir Simulation Symposium*, Texas, USA, February 2011.

-
- [25] H. Hajibeygi, and P. Jenny. Adaptive iterative Multiscale Finite-Volume method. *Journal of Computational Physics*, 230(3):628-643, 2011.
- [26] H. Hajibeygi, S. H. Lee, and I. Lunati. Accurate and efficient simulation of multiphase flow in a heterogeneous reservoir by using error estimate and control in the Multiscale Finite-Volume framework. *SPE Journal*, 17(4):1071-1083. SPE-141954-PA, 2012.
- [27] A. W. Harbaugh. MODFLOW-2005, The U.S. Geological Survey modular groundwater model—the Ground-Water Flow Process: *U.S. Geological Survey Techniques and Methods 6- A16*, variously p., 2005.
- [28] R. J. Held, and T. H. Illangasekare. Fingering of dense non-aqueous phase liquids in porous media 1. Experimental investigation. *Water Resources Research*, 31(5):1223–1231, 1995.
- [29] R. J. Held, and T. H. Illangasekare. Fingering of dense non-aqueous phase liquids in porous media 2. Analysis and classification. *Water Resources Research*, 31(5):1213–1222, 1995.
- [30] R. Helmig. Modellierung von Hydrosystemen. Institut für Wasserbau, Universität Stuttgart, 5. korrigierte Auflage.
- [31] R. Helmig. Multiphase Flow and Transport Processes in the Subsurface: A Contribution to the Modeling of Hydrosystems. Springer Verlag, Berlin, 1997.
- [32] H. R. Henry. Effects of dispersion on salt encroachment in coastal aquifers. *Sea Water in Coastal Aquifers*, U.S. Geological Survey Supply Pap., p. 239–250, 1613-C, 1964.
- [33] E. O. Holzbecher. Modeling Density-Driven Flow in Porous Media: Principles, Numerics, Software. Springer Verlag, Berlin, Germany, 1998.
- [34] T.Y. Hou, and X.-H. Wu. A Multiscale Finite Element method for elliptic problems in composite materials and porous media. *Journal of Computational Physics*, 134(1):169–189, 1997.
- [35] H. Jacks, O. J.E. Smith, and C.C. Mattax. The modeling of a three-dimensional reservoir with a two-dimensional reservoir simulator - the use of dynamic pseudo functions. *SPE Journal*, 13(3):175–185, 1973.
- [36] P. Jenny, S. H. Lee, and H. Tchelepi. Multi-scale Finite-Volume method for elliptic problems in subsurface flow simulation. *Journal of Computational Physics*, 187(1):47–67, 2003.
- [37] P. Jenny, S. H. Lee, and H. Tchelepi. Adaptive fully implicit Multi-scale Finite-Volume method for multi-phase flow and transport in heterogeneous porous media. *Journal of Computational Physics*, 217(2):627–641, 2006.
- [38] P. Jenny, and I. Lunati. Modeling complex wells with the Multi-scale Finite-Volume method. *Journal of Computational Physics*, 228(3):687–702, 2009.

- [39] K. Johannsen, S. Oswald, R. Held, and W. Kinzelbach. Numerical simulation of three-dimensional saltwater-freshwater fingering instabilities observed in a porous media. *Advances in Water Resources*, 29(11):1960–1704, 2006.
- [40] L. Josset, and I. Lunati. Local and global error models to improve uncertainty quantification. *Mathematical Geosciences*, 45(5):1874–8961, 2013.
- [41] A. G. Journal, C. V. Deutsch, and A. J. Desbarats. Power averaging for block effective permeability. *SPE 15128, presented at SPE California Regional Meeting*, Oakland, April 1986.
- [42] V. Kippe, J. E. Aarnes, and K.-A. Lie. A comparison of multiscale methods for elliptic problems in porous media flow. *Computers & Geosciences*, 12(3):377–398, 2008.
- [43] T. J. Kneafsey, and K. Pruess. Laboratory flow experiments for visualizing carbon dioxide - induced, density-driven brine convection. *Transport in Porous Media*, 82(1):123–139, 2010.
- [44] O. Kolditz, R. Ratke, H. J.G. Diersch, and W. Zielke. Coupled groundwater flow and transport: 1. Verification of variable density flow and transport models. *Advances in Water Resources*, 21(1):27–46, 1998.
- [45] R. Künze, and I. Lunati. An adaptive multiscale method for density-driven instabilities. *Journal of Computational Physics*, 231(17):5557–5570, 2012.
- [46] R. Künze, I. Lunati, and S.H. Lee. A Multilevel Multiscale Finite-Volume method. *Journal of Computational Physics*, 255:502–520, 2013.
- [47] R. Künze, and I. Lunati. MaFloT - Matlab Flow and Transport. Published under the GNU licence agreement on www.maflo.com, 2012.
- [48] J. R. Kyte, and D. W. Berry. New pseudo functions to control numerical dispersion. *SPE Journal*, 15(4):269–276, 1975.
- [49] S. H. Lee, H. Zhou, and H. A. Tchelepi. Adaptive Multiscale Finite-Volume method for nonlinear multiphase transport in heterogenous formations. *Journal of Computational Physics*, 228(24):9036–9058, 2009.
- [50] B. P. Leonard. A stable and accurate convective modelling procedure based on quadratic upstream interpolation. *Computer Methods in Applied Mechanics and Engineering*, 19(1):59–98, 1979.
- [51] R. J. LeVeque. Finite Volume Method for Hyperbolic Problems. Cambridge University Press, Cambridge, UK, 2002.
- [52] I. Lunati, and P. Jenny. Multi-scale Finite-Volume method for compressible flow in porous media. *Journal of Computational Physics*, 216(2):616–636, 2006.

-
- [53] I. Lunati, and P. Jenny. The Multiscale Finite-Volume method: a flexible tool to model physically complex flow in porous media. *Proceedings of European Conference of Mathematics of Oil Recovery X*, Amsterdam, Netherlands, September 2006.
- [54] I. Lunati, and P. Jenny. A Multiscale Finite-Volume method for three-phase flow influenced by gravity. *Proceedings of XVI International Conference on Computational Methods for Water Resources*, Copenhagen, Denmark, June 2006.
- [55] I. Lunati, and P. Jenny. Treating highly anisotropic subsurface flow with the Multiscale Finite-Volume technique. *Multiscale Modeling and Simulation*, 6(1):308–318, 2007.
- [56] I. Lunati, and P. Jenny. Multiscale Finite-Volume method for density-driven flow in porous media. *Computers & Geosciences*, 12(3):337–350, 2008.
- [57] I. Lunati, and S. H. Lee. An operator formulation of the Multiscale Finite-Volume method with correction function. *Multiscale Modeling and Simulation*, 8(1):96–109, 2009.
- [58] I. Lunati, M. Tyagi, and S. H. Lee. An iterative Multiscale Finite-Volume algorithm converging to the exact solution. *Journal of Computational Physics*, 230(5):1849–1864, 2011.
- [59] M. J. Nicholl, and R. J. Glass. Infiltration into an analog fracture: experimental observations of gravity-driven fingering. *Vadose Zone Journal*, 4(4):1123–1151, 2005.
- [60] J. M. Nordbottem, and P.E. Bjørstad . On the relationship between the Multiscale Finite-Volume method and domain decomposition preconditioners. *Computers & Geosciences*, 12(3), 367–376, 2008.
- [61] J. M. Ortega, and W. C. Rheinboldt. Iterative Solution of Nonlinear Equations in Several Variables. Society for Industrial and Applied Mathematics, Philadelphia, USA, 2000.
- [62] S. Oswald. Dichteströmungen in Porösen Medien: Dreidimensionale Experimente und Modellierung. Diss. Naturwiss. ETH Zürich, Nr. 12812, 1998, Zürich, Switzerland, 1998.
- [63] G. S.H. Pau, J. B. Bell, K. Pruess, A. S. Almgren, M. J. Lijewski, and K. Zhang. High-resolution simulation and characterization of density-driven flow in CO₂ storage in saline aquifers. *Advances in Water Resources*, 33(4):443–455, 2010.
- [64] K. Pruess, C. M. Oldenburg, and G.J. Moridis. TOUGH2 User’s Guide Version 2. Lawrence Berkeley National Laboratory: *Lawrence Berkeley National Laboratory*, Report LBNL-43134, 1999.
- [65] K. Pruess. Numerical modeling studies of the dissolution-diffusion-convection process during CO₂ storage in saline aquifers. Lawrence Berkeley National Laboratory: *Lawrence Berkeley National Laboratory*, Paper LBNL-1243E, 2008.

- [66] A. Riaz, M. Hesse, H. A. Tchelepi, and F. M. Orr. Onset of convection in a gravitationally unstable diffusive boundary layer in porous media. *Journal of Fluid Mechanics*, 548:87–111, 2006.
- [67] Y. Saad, and M. H. Schultz. GMRES: a generalized minimal residual algorithm for solving non-symmetric linear systems. *SIAM Journal on Scientific and Statistical Computing*, 7(3):856–869, 1986.
- [68] Y. Saad. *Iterative Methods for Sparse Linear Systems*. Society for Industrial and Applied Mathematics, Philadelphia, USA, 2003.
- [69] C.-T. Simmons, and K. A. Narayan. Mixed convection processes below a saline disposal basin. *Journal of Hydrology*, 194(1–4):263–285, 1997.
- [70] B. F. Smith, P. E. Bjørstad, and W. Gropp. *Domain Decomposition: Parallel Multilevel Methods for Elliptic Partial Differential Equations*. Cambridge University Press, New York, USA, 1996.
- [71] B. Smith. A Quick Guide to GPLv3. Free Software Foundation, Inc., <http://www.gnu.org/licenses/quick-guide-gplv3.html>, 2007.
- [72] K. Stüben. An introduction to Algebraic Multigrid. In *Multigrid*, ed. U. Trottenberg, C. W. Oosterlee, and A. Schüller, Appendix, 413-532, London: Academic Press, 2001.
- [73] C. I. Voss and W. R. Souza. Variable density flow and solute transport simulation of regional aquifers containing a narrow freshwater-saltwater transition zone. *Water Resources Research*, 23(10):1851–1866, 1987.
- [74] C. Wolfsteiner, S. H. Lee, and H. A. Tchelepi. Well modeling in the Multiscale Finite-Volume method for subsurface flow simulation. *Multiscale Modeling and Simulation*, 5(3):900–917, 2006.
- [75] X. Xu, S. Chen, and D. Zhang. Convective stability analysis of the long-term storage of carbon dioxide in deep saline aquifers. *Advances in Water Resources*, 29(3):397-407, 2006.
- [76] H. Zhou, and H.A. Tchelepi. Two-stage Algebraic Multiscale linear solver for highly heterogeneous reservoir models. *SPE Journal*, 17(2):523-539. SPE-141473-PA, 2012.

Curriculum Vitae

Personal

Name	Rouven Künze
Date of Birth	January 25, 1981
Citizenship	German

Education

10/2009 – 03/2014	Ph.D. student, Faculty of Geosciences and Environment University of Lausanne, Switzerland
10/2002 – 03/2008	Dipl.-Ing. (Environmental Engineering) University of Stuttgart, Germany

Work Experience

05/2012 – 06/2012	Reservoir Engineer Chevron Energy Technology Co., San Ramon, California, USA
06/2011 – 08/2011	Reservoir Engineer Chevron Energy Technology Co., San Ramon, California, USA
11/2008 – 09/2009	Junior Hydrologist Hydrotec Engineering, Aachen, Germany
05/2007 – 03/2008	Diplomate/ Intern GIT HydroS Consult, Freiburg, Germany
04/2006 – 04/2007	Research Assistant IWS, University of Stuttgart, Germany
10/2005 – 03/2006	Research Assistant Environmental Engineering Lab., University of Tokyo, Japan

Scholarships

10/2005 – 03/2006	Landesstipendium Baden-Württemberg
-------------------	------------------------------------

Publications

Peer-Reviewed Publications:

- R. Künze, P. Tomin, and I. Lunati. Local modeling of instability onset for global finger evolution, *submitted to Advances in Water Resources*.
- R. Künze, I. Lunati, and S.H. Lee. A Multilevel Multiscale Finite-Volume method, *Journal of Computational Physics*, 255:502-520, 2013.
- R. Künze, and I. Lunati. An adaptive multiscale method for density-driven instabilities, *Journal of Computational Physics*, 231(17):5557-5570, 2012.

Conference Proceedings:

- R. Künze, I. Lunati, and S.H. Lee. A Multilevel Multiscale Finite-Volume method. Proceeding for the ECMOR XIII - 13th European Conference on the Mathematics of Oil Recovery, EAGE, Biarritz, France, 2012.
- R. Künze, and I. Lunati. Modeling density-driven flow instabilities with the Multiscale Finite-Volume technique. Proceeding for the IAHR Groundwater Symposium, Universidad Politecnica de Valencia, Spain, 2010.

Other Publications:

- R. Künze. Characterization and Quantification of Interactions between Drainage Ditch, Groundwater Body and Quarry Pond within the Scope of a Numerical Simulation of a Transient 3D Flow and Transport Process using FEFLOW. M.Sc. Thesis, University of Stuttgart/ GIT HydroS Consult, Freiburg, Germany, 2008.